Immune cell topography predicts response to PD-1 blockade in cutaneous T cell lymphoma

Garry Nolan (✉ gnolan@stanford.edu)
Stanford School of Medicine   https://orcid.org/0000-0002-8862-9043

Darci Phillips
Stanford School of Medicine   https://orcid.org/0000-0002-0804-3342

Magdalena Matusiak
Stanford School of Medicine

Belén Gutierrez
Stanford School of Medicine

Salil Bhate
Stanford University

Graham Barlow
Stanford University   https://orcid.org/0000-0001-9335-5414

Sizun Jiang
Stanford University   https://orcid.org/0000-0001-6149-3142

Janos Demeter
Stanford University   https://orcid.org/0000-0002-7301-8055

Kimberly Smythe
Fred Hutchinson Cancer Research Center   https://orcid.org/0000-0002-2329-8298

Robert Pierce
Fred Hutchinson Cancer Research Center

Steven Fling
Fred Hutchinson Cancer Research Center   https://orcid.org/0000-0001-6263-0153

Nirasha Ramchurren
Fred Hutch Cancer Research Center

Martin Cheever
Fred Hutch Cancer Research Center

Yury Goltsev
Stanford University School of Medicine

Robert West
Stanford University Medical Center

Michael Khodadoust
Stanford School of Medicine

Youn Kim

Stanford University Medical Center

Christian Schürch

Stanford University School of Medicine   https://orcid.org/0000-0002-1792-1768

Article

1 **Immune cell topography predicts response to PD-1 blockade in cutaneous T cell lymphoma**
2
3
4 Darci Phillips[1,2,3,7], Magdalena Matusiak[3,7], Belén Rivero Gutierrez[3], Salil S. Bhate[1,3,4], Graham L. Barlow[1,3],

5 Sizun Jiang[1,3], Janos Demeter[1], Kimberly S. Smythe[5], Robert H. Pierce[5], Steven P. Fling[5], Nirasha

6 Ramchurren[5], Martin A. Cheever[5], Yury Goltsev[1,3], Robert B. West[3], Michael S. Khodadoust[6,8], Youn H.

7 Kim[2,6,8], Christian M. Schürch[1,3,8]*, and Garry P. Nolan[1,3,8]*

8
9
10
11 [1] Department of Microbiology & Immunology, Stanford University School of Medicine, Stanford, CA

12 94305, USA

13 [2] Department of Dermatology, Stanford University School of Medicine, Stanford, CA 94305, USA

14 [3] Department of Pathology, Stanford University School of Medicine, Stanford, CA 94305, USA

15 [4] Department of Bioengineering, Stanford University Schools of Engineering and Medicine, Stanford, CA

16 94305, USA

17 [5] Cancer Immunotherapy Trials Network, Fred Hutchinson Cancer Research Center, Seattle, WA, USA

18 [6] Division of Oncology, Stanford University School of Medicine, Stanford, CA 94305, USA

19 [7] Co-first authors

20 [8] Co-senior authors

21

22 *Corresponding authors: christian.m.schuerch@gmail.com, gnolan@stanford.edu
23
24
25
26 **Keywords**

27 Cutaneous T cell lymphoma (CTCL), anti-PD-1 immunotherapy, tumor microenvironment (TME), CODEX

28 multiplex tissue imaging, RNA sequencing, spatial biomarkers, chemokines

29
30

31 **ABSTRACT**

32 Anti-PD-1 immunotherapies have transformed cancer treatment, yet the determinants of clinical

33 response are largely unknown. We performed CODEX multiplexed tissue imaging and RNA sequencing

34 on 70 tumor regions from 14 advanced cutaneous T cell lymphoma (CTCL) patients enrolled in a clinical

35 trial of pembrolizumab therapy. Clinical response was not associated with the frequency of tumor-

36 infiltrating T cell subsets, but rather with striking differences in the spatial organization and functional

37 immune state of the tumor microenvironment (TME). After treatment, pembrolizumab responders had

38 a localized enrichment of tumor and $CD4^+$ T cells, which coincided with immune activation and cytotoxic

39 PD-1^+ $CD4^+$ T cells. In contrast, non-responders had a localized enrichment of Tregs pre- and post-

40 treatment, consistent with a persistently immunosuppressed TME and exhausted PD-1^+ $CD4^+$ T cells.

41 Integrating these findings by computing the physical distances between PD-1^+ $CD4^+$ T cells, tumor cells,

42 and Tregs revealed a spatial biomarker predictive of pembrolizumab response. Finally, the chemokine

43 CXCL13 was upregulated in tumor cells in responders post-treatment, suggesting that chemoattraction

44 of PD-1^+ $CD4^+$ T cells towards tumor cells facilitates a positive outcome. Together, these data show that T

45 cell topography reflects the balance of effector and suppressive activity within the TME and predicts

46 clinical response to PD-1 blockade in CTCL.

47

INTRODUCTION

48

49   Cutaneous T cell lymphomas (CTCL) are a rare, heterogeneous group of T cell malignancies that

50   primarily occur in the skin. The majority of CTCLs are comprised of mycosis fungoides and Sézary

51   syndrome, which originate from mature, skin-tropic CD4^{+} T cells[1]. A third of patients present with

52   advanced-stage disease and those meeting high risk criteria have a 5-year survival rate of 28%[2]. With the

53   exception of hematopoietic stem cell transplantation, there are no curative therapies for advanced

54   CTCL, and current treatments typically induce short-lived, partial disease control[3]. However, immune

55   checkpoint inhibitors, such as antibodies against PD-1, restore T cell effector function at the tumor site[4,5]

56   and promote robust and durable responses in a number of advanced cancers[6-8]. In CTCL, PD-1 and its

57   ligands can be simultaneously expressed on tumor cells, making this pathway an attractive therapeutic

58   target for PD-1 blockade[9-12].

59   A Cancer Immunotherapy Trials Network (CITN) multicenter phase II clinical trial of the anti-PD-1

60   immunotherapy, pembrolizumab, in heavily pre-treated patients with advanced relapsed/refractory

61   CTCL was recently reported (NCT02243579)[13]. In this study, 38% of patients achieved a sustained clinical

62   response, whereas 25% experienced rapid disease progression, likely because inhibition of PD-1 on

63   tumor cells promoted cancer growth[14,15]. Such outcome discrepancies underscore a need for predictive

64   biomarkers of PD-1 blockade that will allow patients to be stratified into probable responders and non-

65   responders prior to initiating therapy.

66   To date, biomarker studies with immunohistochemistry (IHC), gene expression profiling, and

67   mass cytometry (CyTOF), have not yet provided predictive indices of pembrolizumab responsiveness in

68   CTCL[13]. Similarly, predictive biomarkers remain in-demand for other tumor types and

69   immunotherapies[16,17]. As the immune system acts via coordinated cell-cell association, it is expected

70   that spatial cellular attributes within the tumor microenvironment (TME) would be predictive of clinical

71   outcomes. As such, organized cellular contexts would be productive whereas incorrectly arranged

72   cellular contexts (i.e., absence or misplacement of certain cell-types) would prognosticate a negative

73   outcome. Indeed, recent studies indicate that immune cells are not randomly distributed within the

74   TME, but are purposefully organized into cellular neighborhoods and niches that facilitate anti- or pro-

75   tumor functions[18,19]. This raises the question of how PD-1 blockade alters spatial cellular context, and in

76   turn, how such changes in architecture relate to patient responses in CTCL.

77   We combined CO-Detection by indEXing (CODEX) multiplexed tissue imaging[19,20] with gene

78   expression profiling by RNA-seq to interrogate tumors from 14 patients with advanced CTCL sampled

79   before and after pembrolizumab treatment. Then we computationally correlated spatial protein

80   information at the single cell level with matched global gene expression data to generate insights into

81   the drivers and resistors of PD-1 blockade. Our data revealed a localized enrichment of effector CD4$^+$ T

82   cells in responders versus inhibitory Tregs in non-responders. Such topographical differences coincided

83   with variations in the functional immune state of the TME, T cell function, and tumor cell-specific

84   chemokine expression. We integrated these findings into a single *SpatialScore*—a spatial biomarker

85   predictive of pembrolizumab outcome—that can be accurately recapitulated using clinically accessible

86   multiplexed IHC (mIHC) platforms. The results underscore a key determinant of spatial cellular

87   organization, namely a distancing balance of effector and suppressive T cell activity, for predicting anti-

88   PD-1 immunotherapy response in CTCL.

89

90   **RESULTS**

91   **CTCL clinical cohort and multimodal experimental approach**

92   We analyzed pre- and post-treatment biopsies from 14 patients with advanced-stage CTCL, who

93   received pembrolizumab every 3 weeks for up to 2 years as part of the CITN-10 trial (NCT02243579) (**Fig.**

94   **1a.1, Sup. Fig. 1a-b, Sup. Table 1**)[13]. The post-treatment biopsies were collected at several timepoints,

95   which is detailed per patient in **Sup. Fig. 1c** and **Sup. Table 1**. The spatial organization and

96   immunogenomic heterogeneity of the CTCL TME was dissected using a formalin-fixed paraffin-

4

97   embedded (FFPE) tissue microarray from 70 patient-matched pre- and post-treatment skin tumor

98   samples (**Fig. 1a.2**). The tissue microarray spots were selected from the most infiltrated regions of the

99   skin biopsies. CODEX multiplexed protein imaging identified 117,170 cells in the tissue microarray. These

100   results were integrated with 64 tissue transcriptomes obtained from serial sections using laser capture

101   microdissection and Smart-3Seq[21] (i.e., RNA-seq) (**Fig. 1a.3**). Integrative analyses, including cellular

102   neighborhood assessment[19] and CIBERSORTx (CSx)[22], were then used to profile the molecular dynamics

103   of CTCL and identify predictive biomarkers of anti-PD-1 immunotherapy (**Fig. 1a.4**).

104   Therapeutic response to pembrolizumab was assessed by consensus global response criteria[23].

105   No significant differences were observed at baseline between responders and non-responders for

106   patient demographics, cancer type/stage, and treatment history (**Sup. Fig. 1b**). Clinical outcomes were

107   significantly different between patient groups (**Sup. Fig. 1b**). Responders had a significant improvement

108   in their overall skin response compared to non-responders, as measured by the modified Severity

109   Weighted Assessment Tool (mSWAT)[24] (**Sup. Fig. 1b**). Similarly, overall survival was significantly longer in

110   responders than non-responders: Non-responders had a median survival of 109 weeks after treatment

111   initiation, whereas all but one responder was alive at the median follow-up time of 142 weeks (**Fig. 1b**).

112   The expression of key T cell, macrophage and PD-1 signaling markers was assessed by standard IHC for

113   each patient's pre-treatment tumor biopsy: PD-L2 expression was slightly increased in non-responders

114   compared to responders but did not reach statistical significance (**Fig. 1c**). No differences were observed

115   for the other seven markers, as shown for CD4, FoxP3, PD-1, and PD-L1 (**Fig. 1d**).

116

117   **Discrimination of malignant from reactive CD4+ T cells in the CTCL TME**

118   Distinguishing malignant from reactive CD4+ T cells is a major challenge in CTCL, because no

119   protein marker is 100% specific for tumor cells and both cell-types can be clonal[25]. Using a 55-marker

120   CODEX panel (**Fig. 1e, Sup. Fig. 1d, Sup. Table 2**), unsupervised machine learning and manual curation

121   based on marker expression, tissue localization, and morphology, we identified and validated 21 unique

122   cell-type clusters (**Fig. 1f, Sup. Fig. 2a-b**), including reactive CD4^{+} T cells and malignant CD4^{+} T cells (i.e.,

123   tumor cells). Comparing the fluorescent stainings of reactive CD4^{+} T cells (blue crosses) and malignant

124   CD4^{+} T cells (red crosses) showed that in tumor cells CD7 was decreased and CD25 and Ki-67 were

125   increased (**Fig. 1g**), consistent with an advanced CTCL phenotype[26]. Quantifying these expression

126   differences for tumor cells relative to reactive CD4^{+} T cells showed a fold-change of 0.40 for CD7, 1.87

127   for CD25, and 3.47 for Ki-67 (**Fig. 1h**, $p<0.0001$). Tumor cells were also larger in size than reactive CD4^{+} T

128   cells (**Fig. 1i**), in line with previous reports[27]. One patient had large cell transformation, but the average

129   size of tumor cells in that patient was not significantly different from the other 13 patients. Additionally,

130   we identified genes predictive of the frequency of tumor cells per tissue microarray spot by fitting an L1-

131   regularized linear model to bulk RNA-seq data. This confirmed that higher expression of several known

132   CTCL marker genes, including *CD27*, *IL-32*, *CXCL13*, *BATF*, and *TIGIT*[28-32], was associated with spots with

133   higher frequencies of tumor cells (**Fig. 1j**, see yellow highlighted gene names). Notably, CTCL tumor cells

134   can also express FoxP3[33], as was the case for one patient in this clinical trial cohort. Our clustering

135   approach identified this population of malignant FoxP3^{+} CD4^{+} T cells, which differed significantly from

136   Tregs, with lower CD3, CD4, and FoxP3 marker expression and larger cell size (**Sup. Fig. 1e**). Given the

137   heterogeneity of CTCL, the marker expression profile of tumor cells may differ between cohorts,

138   especially those that were heavily pre-treated. However, these findings demonstrate that multiplexed

139   imaging can discriminate malignant from reactive CD4^{+} T cells at the single-cell level, which is supported

140   by cell size measurements and gene expression profiling.

141

142   **Deep profiling of the CTCL TME in response to anti-PD-1 immunotherapy**

143   Anti-PD-1 immunotherapies are premised on the ability to alter the delicate balance of positive

144   and negative immune signaling to promote the recognition and elimination of tumor cells. Tumor cells,

145   however, shift this balance in favor of their own survival and proliferation. We reasoned that delineating

146   the complexities of tumor and immune cell interactions within the TME may reveal the cell specific

147   organizations that determine pembrolizumab response and resistance in CTCL.

148   We first explored how cellular composition contributes to the efficacy of PD-1 blockade in CTCL

149   by cataloging the frequencies of the 21 cell-types identified by CODEX across patient groups. The 21 cell-

150   types included 13 immune cell-types, 6 auxiliary cell-types, and 2 tumor cell-types (**Sup. Fig. 2b**).

151   Markers for T cell subsets (CD4, CD8, FoxP3), macrophages (CD68), dendritic cells (CD11c), tumor cells

152   (CD4), vasculature (CD31), and epithelium (cytokeratin) were clearly visualized in the CODEX fluorescent

153   images (**Fig. 2a-b, upper panels; Sup. Fig. 3a**). The corresponding hematoxylin and eosin (H&E) images

154   (**Fig. 2a-b**, inserts; **Sup. Fig. 3b**) confirmed accurate staining of structural elements like epithelium and

155   vasculature. Fluorescent staining of immune and tumor cells confirmed the cell-type assignments shown

156   in the corresponding cell-type maps (**Fig. 2a-b, lower panels)**.

157   Interestingly, no differences in the content of the 21 identified cell-types were noted between

158   responders and non-responders pre- or post-treatment (**Fig. 2c-d; Sup. Fig. 2c**). The combined

159   frequencies of tumor, immune and auxiliary cell-types each comprised approximately one-third of all

160   cells (**Fig. 2c, upper panel**); the same trend held across patient groups (**Sup. Fig. 2c**). Tumor cell content

161   (averaged across all TMA spots in a patient group) was unchanged in responders or non-responders

162   following pembrolizumab therapy (**Sup. Fig. 2c**), likely because only heavily infiltrated skin tumor biopsy

163   regions were used for this study. Among all immune cells, the ranked cell-type frequencies were 38% for

164   M_1 macrophages, 21% for Tregs, 15% for CD8$^+$ T cells, 5% for M_2 macrophages, 5% for CD4$^+$ T cells, and

165   <5% for other immune cell-types including B cells, plasma cells, dendritic cells, Langerhans cells, mast

166   cells, and neutrophils (**Fig. 2c, lower panel**). No differences in the mean frequencies of immune cell-

167   types were observed when comparing responders and non-responders pre- and post-treatment; this is

168   highlighted for T cells (CD4$^+$ T, CD8$^+$ T, Tregs) and macrophages (M1 and M2) (**Fig. 2d**). This finding is

169   consistent with the initial publication on this CTCL cohort and our baseline IHC data (**Fig. 1c-d**), which

170   showed no correlation between pembrolizumab response and the expression of T cell, macrophage or

7

171   PD-1 signaling markers[13]. However, it contrasts with some solid tumor studies, which have correlated

172   the density of tumor infiltrating lymphocytes with clinical outcome[34,35] and immunotherapy

173   response[36,37].

174   We next focused on differences in immune signaling between responders and non-responders.

175   Immunogenomic analyses were preformed to characterize the functional immune state of the TME,

176   which has been shown to be a key determinant of immunotherapeutic activity[38]. Gene expression

177   signatures that have predicted PD-1/PD-L1 blockade response (e.g., IFN-γ scores[39], **Sup. Table 3**) and

178   non-response (e.g., TGF-β scores[40], **Sup. Table 3**) in solid tumors were applied to our CTCL data. No

179   differences were observed pre-treatment in responders versus non-responders for the IFN-γ (**Fig. 2e**,

180   median R, pre (0.77) versus NR, pre (0.76)) or TGF-β (**Fig. 2f**, median R, pre (0.28) versus NR, pre (-0.32))

181   gene scores; hence, neither signature was predictive of pembrolizumab response in CTCL. Since these

182   predictive gene signatures were derived from single-disease studies, their utilization may be limited to

183   similar solid tumor types[41].

184   Rare cancers like CTCL do not have specifically defined immune gene signatures, making it a

185   challenge to catalogue their tumor immunogenicity. Gene lists of immune activation (e.g., *CD27*, *EOMES*,

186   and *ICOS*) and immunosuppression (e.g., *ENTPD1*, *TGFB1*, and *TIGIT*) molecules were therefore compiled

187   (**Sup. Table 3**) and used to assess how the functional immune state of the CTCL TME was altered in

188   response to pembrolizumab. Notably, genes like *PDCD1* and *TNFRSF18*, which can be both immune

189   activating and suppressive depending on cellular state and microenvironmental context, were excluded

190   from this analysis. The immune activation gene score was significantly increased in responders post-

191   treatment compared with pre-treatment (**Fig. 2g**, median R, pre (-2.54) versus R, post (1.21)), with no

192   significant change in non-responders post- versus pre-treatment. This indicates that only responders

193   develop an immune activated TME phenotype following pembrolizumab therapy. In contrast, the

194   immunosuppression gene scores were significantly increased in non-responders compared to

195   responders both pre- and post-treatment (**Fig. 2h**, median NR, pre (0.59) versus R, pre (-0.83) and NR,

8

196   post (0.64) versus R, post (-1.12)), implying that non-responders have an immunosuppressed TME

197   phenotype relative to responders. Collectively, these results demonstrate that the functional immune

198   state of the CTCL TME depends on factors beyond raw immune cell counts. Exploring the spatial

199   patterns of immune infiltration is an essential step towards understanding the indicators predictive of

200   immunotherapy outcome.

201

202   **PD-1 blockade induces spatial re-organization of the CTCL TME**

203   It is expected that the functional immune state of the TME will be mediated by its spatial cellular

204   organization. Cellular neighborhood (CN) analysis, applied previously in a study on colorectal cancer[19],

205   was performed to obtain a high level view of CTCL tissue architecture. CNs are analogous to urban

206   neighborhoods—essentially geographically localized areas within a larger city that facilitate social

207   interaction[42] (**Sup. Fig. 2d**). Likewise, CNs are defined by a localized enrichment of specific cell-types

208   within the tissue that mediate cellular interactions and vital tissue functions (**Sup. Fig. 2e**).

209   Computationally, the CN algorithm extracts quantitative data on the composition and spatial

210   distribution of individual cells to reveal how local cellular niches are organized within tissues (**Fig. 3a**)[19].

211   Specifically, computational parameters like the window size and number of CNs to be computed are

212   manually set (**Fig. 3a.1**). Each cell in the tissue is assigned to a given CN based on the composition of cell-

213   types within the specified window (**Fig. 3a.2**). The windows are then clustered and the correlation of

214   CNs and cell-types are represented as a heatmap (**Fig. 3a.3**). CNs are visualized as Voronoi diagrams and

215   analyzed to better understand cellular spatial behavior (**Fig. 3a.4**).

216   Using a window size of 10 nearest neighbors, we identified 10 distinct CNs that were conserved

217   across this CTCL cohort (**Fig. 3b, Sup. Fig. 3c**). Some CNs recapitulated structural components that are

218   clearly discernable in the corresponding H&E and fluorescent images, such as epithelium (CN-1, green

219   region) and vasculature (CN-3, brown region) (**Fig. 3c**). The other CNs were composed of previously

220   unappreciated sub-structures within the dermal infiltrate that were not apparent in the corresponding

9

221　H&E or fluorescent images, including immune-infiltrated stroma (CN-2, red region), vascularized stroma

222　(CN-4, gray region), tumor and dendritic cells (CN-5, purple region), lymphatic enriched stroma (CN-6,

223　orange region), tumor and mixed immune cells (CN-7, cyan region), tumor and CD4$^+$ T cells (CN-8, yellow

224　region), innate immune cell enriched (CN-9, blue region), and Treg enriched (CN-10, pink region) (**Fig.**

225　**3c**).

226　　　　　Representative Voronoi diagrams from a responder (**Fig. 3d,** see CN-5 and CN-8, purple and

227　yellow regions, respectively) and non-responder (**Fig. 3e,** see CN-10, pink region) post-treatment show

228　significant differences in the frequency of CNs between patient groups. CNs enriched in tumor and

229　dendritic cells (CN-5, purple region) (**Fig. 3f**, mean frequency in R, post (21.4%) versus R, pre (3.2%)) and

230　tumor and CD4$^+$ T cells (CN-8, yellow region) (**Fig. 3g**, mean frequency in R, post (19.0%) versus R, pre

231　(8.5%)) were present at significantly higher levels in responders post-treatment than in non-responders

232　or either group pre-treatment. In contrast, the Treg enriched CN (CN-10, pink region) was present at a

233　significantly higher frequency in non-responders than responders pre- and post-treatment (**Fig. 3h**,

234　mean frequency in NR, pre (15.5%) versus R, pre (3.3%) and NR, post (22.7%) versus R, post (4.9%)).

235　Notably, these differences in the spatial organization of certain cell-types were observed even though

236　there were no differences in the abundance of CD4$^+$ T cells, dendritic cells, Tregs, or tumor cells between

237　patient groups, as previously described (**Fig. 2c-d**).

238　　　　　The increased co-localization of dendritic cells, CD4$^+$ T cells and tumor cells in responders post-

239　treatment, relative to other patient groups, suggests that the more immune activated TME observed in

240　responders following pembrolizumab therapy (i.e., increased immune activation gene score in **Fig. 2g**)

241　may in part be mediated by CD4$^+$ T cell activation by antigen-presenting cells. Indeed, after PD-1

242　blockade, responders had increased frequencies of activated ICOS$^+$ CD4$^+$ T cells (**Fig. 3i**, mean frequency

243　in R, post (1.9%) versus R, pre (0.7%) and NR, post (0.2%)) and proliferating Ki-67$^+$ CD4$^+$ T cells (**Fig. 3j**,

244　mean frequency in R, post (0.8%) versus R, pre (0.1%) and NR, post (0.1%)) compared to responders pre-

245   treatment and non-responders post-treatment, suggesting that pembrolizumab therapy activates CD4^{+} T

246   cells through upregulation of immune activating molecules.

247   The increased frequency of the Treg enriched CN in non-responders pre- and post-treatment is

248   consistent with our finding that non-responders have a persistently immunosuppressed TME (i.e.,

249   increased immunosuppression gene score in **Fig. 2h**), which is further supported by the higher frequency

250   of a potently suppressive subset of Tregs expressing ICOS in non-responders (**Fig. 3k**, mean frequency in

251   NR, pre (4.4%) versus R, pre (1.2%) and NR, post (6.2%) versus R, post (1.2%))[43,44]. Interestingly, despite

252   treatment with PD-1 blockade, no differences were observed in PD-1^{+} subsets of CD4^{+}, CD8^{+}, Tregs, or

253   tumor cells between groups (**Sup. Fig. 2-i**). Collectively, these data link the spatial re-organization of

254   CD4^{+} T cells, tumor cells, and Tregs with immune activity of the TME, highlighting patterns of immune

255   control and pembrolizumab responsiveness.

256

257   **Spatial signature of PD-1^{+} CD4^{+} T cells, tumor cells, and Tregs predicts pembrolizumab response in**

258   **CTCL**

259   It is reasonable to suspect that specific cellular interactions drive pembrolizumab

260   responsiveness in CTCL. While complex spatial analyses have been used to prognosticate cancer

261   outcomes in select clinical cohorts[19], we hypothesized that a simplified approach based on the distances

262   between specific immune and tumor cells could be employed. Guided by our CN findings, which

263   highlighted the spatial arrangement of CD4^{+} T cells, tumor cells and Tregs, we formalized a

264   computational scoring approach to standardizing a spatial signature. This score, termed *SpatialScore*,

265   calculates the physical distance ratio of each CD4^{+} T cell and its nearest tumor cell ("right" distance)

266   relative to its nearest Treg ("left" distance) (**Fig. 4a**). A lower *SpatialScore* (i.e., CD4^{+} T cells are closer to

267   tumor cells than Tregs) suggests increased T cell effector activity (**Fig. 4a.1**), whereas a higher

268   *SpatialScore* (i.e., CD4^{+} T cells are closer to Tregs than tumor cells) suggests increased T cell suppression

11

269   (**Fig. 4a.2**). As such, the *SpatialScore* can be viewed as a proxy of the balance between T cell effector

270   activity and suppression in the TME.

271   The *SpatialScore* is calculated on a per cell basis and the mean value is reported for each patient

272   group. When calculated with all CD4$^+$ T cells, the pre-treatment *SpatialScore* was significantly lower in

273   responders than non-responders, with enhancement post-treatment for both groups (**Fig. 4b**, compare

274   mean *SpatialScore* for R, pre (0.57) versus NR, pre (0.63)). The same trend was observed on a per patient

275   basis (**Sup. Fig. 4a**). Since the current study trialed PD-1 blockade in CTCL, we next asked how the

276   *SpatialScore* was influenced by the PD-1$^+$CD4$^+$ T cell subset. As observed when calculated with all CD4$^+$ T

277   cells, when computed with PD-1$^+$CD4$^+$ T cells, tumor cells, and Tregs, the *SpatialScore* was lower in

278   responders than non-responders (**Fig. 4c**, compare mean *SpatialScore* for R, pre (0.41) versus NR, pre

279   (0.62)). The same trend was seen on a per patient basis (**Sup. Fig. 4b**). Notably, the *SpatialScore* was

280   lower in responders pre-treatment when calculated with PD-1$^+$CD4$^+$ T cells versus all CD4$^+$ T cells,

281   implying increased effector activity in this T cell subset. These results suggest that PD-1$^+$ CD4$^+$ T cells in

282   responders are primed for increased anti-tumor activity, which is enhanced in the immune activated

283   TME that results following pembrolizumab therapy.

284   Since the *SpatialScore* approach appears to predict the outcome of PD-1 blockade in CTCL, it

285   stands to reason that there is a deep phenotype of cell-type specific architecture that is driving the

286   *SpatialScore*. Pre-treatment differences were driven by the closer proximity of PD-1$^+$CD4$^+$ T cells and

287   Tregs in non-responders (**Sup. Fig. 4c**, see red arrow), consistent with the increased immunosuppression

288   gene scores in non-responders relative to responders (**Fig. 2h**). In contrast, post-treatment differences

289   were driven by the closer proximity of PD-1$^+$CD4$^+$ T cells and tumor cells in responders (**Sup. Fig. 4d**, see

290   red arrow), consistent with the increased immune activation gene score in responders relative to non-

291   responders (**Fig. 2i**). Importantly, no correlation was identified between the abundance of PD-1$^+$CD4$^+$ T

292   cells, tumor cells, or Tregs and the *SpatialScore* on a per tissue microarray spot basis (**Sup. Fig. 4g-i**),

293   implying that the *SpatialScore* is not merely driven by cell-type frequency. Additionally, the mean

12

294   *SpatialScore* was significantly different from that of a random sample in responders pre- and post-

295   treatment (**Sup. Fig. 4j and l**), but not in non-responders pre- and post-treatment (**Sup. Fig. 4k and m**).

296   This suggests that an active process coordinates the spatial interactions of PD-1^{+} CD4^{+} T cells, tumor cells

297   and Tregs in responders, whereas no such mechanism exists in non-responders. Finally, when the

298   *SpatialScore* was calculated for CD8^{+} T cells (**Sup. Fig. 4e**) or PD-1^{+}CD8^{+} T cells (**Sup. Fig. 4f**), it was not

299   predictive of pembrolizumab response. The increased proximity of CD4^{+} T cells and tumor cells observed

300   in pembrolizumab responders—and lack thereof for CD8^{+} T cells—suggests that CD4^{+}T cells may have a

301   more important effector function in CTCL than previously appreciated.

302

303   **PD-1^{+} CD4^{+} T cells upregulate cytotoxic effector molecules in pembrolizumab responders**

304   We reasoned that the spatial proximity of PD-1^{+} CD4^{+} T cells and tumor cells reflected the

305   enhanced CD4^{+} T cell tumor reactivity seen in responders following pembrolizumab therapy. CODEX and

306   RNA-seq datasets were therefore used to assess the cytotoxic potential of effector PD-1^{+}CD4^{+} T cells. In

307   CTCL, cytotoxic CD4^{+} T cells act through a granzyme-perforin-dependent pathway to achieve tumor cell

308   killing[45,46], similar to cytotoxic CD8^{+} T cells[46-48]. The expression of granzyme B (GZMB) on PD-1^{+} CD4^{+} T

309   cells was increased in responders post- versus pre-treatment (**Fig. 4d**, mean GZMB expression, R, post

310   (26.9) versus NR, post (12.2) and R, pre (12.1)). This increased GZMB expression is confirmed visually in a

311   responder post-treatment with DRAQ5 (nuclear stain), CD4, PD-1, and GZMB fluorescent staining (**Fig.**

312   **4e**, see white arrow) and is consistent with the increased cytotoxicity gene score[49,50] seen in responders

313   post-treatment compared to pre-treatment (**Fig. 4f**, median R, post (1.21) versus R, pre (-1.77), **Sup.**

314   **Table 3**). No differences were observed between non-responders pre- and post-treatment with regards

315   to GZMB expression on PD-1^{+} CD4^{+} T cells (**Fig. 4d**, mean expression, NR, pre (11.7) versus NR, post

316   (12.2)) or the cytotoxicity gene score (**Fig. 4e**, median NR, pre (0.21) versus NR, post (0.43)).

317   Increased cytotoxicity should coincide with decreased tumor cell aggressiveness and, using

318   genes associated with poor response to therapy[51] and progressive[52] CTCL (**Sup. Table 3**), it was observed

319   that tumor aggressiveness decreased in 100% of responders following pembrolizumab therapy (**Fig. 4g**)

320   but increased in 71% of non-responders (**Fig. 4h**). This increased tumor aggressiveness in non-

321   responders was further supported by an increased frequency of proliferating (Ki-67^{+}) tumor cells in non-

322   responders post- versus pre-treatment and compared to responders post-treatment (**Fig. 4i**, mean

323   frequency, NR, post (17.0%) versus NR, pre (8.9%) and R, post (7.8%))[26,53]. Collectively, these data show

324   the cytotoxic potential of effector PD-1^{+} CD4^{+} T cells and their association with a favorable response to

325   pembrolizumab therapy in CTCL.

326

327   **Validation of the *SpatialScore* biomarker with a clinically accessible multiplexed IHC platform**

328   While mIHC approaches, such as CODEX, provide the raw data for deep cellular profiling,

329   translating these findings to a clinical arena requires simplifying the predictive signature to a diagnostic

330   platform that can be readily implemented in clinical practice. Vectra, in conjugation with the Phenoptics

331   workflow, is a commercially available, widely adopted clinical mIHC imaging platform, which has been

332   used to identify biomarkers for renal cell carcinoma[54] and B cell lymphoma[55]. We devised a simplified

333   staining panel (DAPI, CD3, CD4, CD7, CD8, CD25, FoxP3, and PD-1) that captured the PD-1^{+} CD4^{+} T cells,

334   tumor cells, and Tregs used to calculate the *SpatialScore*. Notably, the tumor cell phenotype identified

335   by CODEX (i.e., decreased expression of CD7 and increased expression of CD25 and Ki-67; **Fig. 1h**), was

336   critical for establishing this streamlined staining panel and could be readily transferred to the Vectra

337   platform.

338   Serial sections from the same CTCL TMA used for CODEX and RNA-seq were stained with this

339   simplified panel and imaged with Vectra (**Sup. Fig. 5a**). Across all TMA spots, 126,653 cells were

340   identified, including 2,957 PD-1^{+} CD4^{+} T cells, 6,161 Tregs, and 19,847 tumor cells. The *SpatialScore* was

341   then computed on a per cell basis and the mean was reported for each patient group. Consistent with

342   the CODEX results (**Fig. 4c**), the Vectra-calculated *SpatialScore* was significantly lower in responders than

343   non-responders pre-treatment (**Fig. 4j**, mean *SpatialScore* R, pre (0.35) versus NR, pre (0.76)), with

344   enhancement post-treatment compared to pre-treatment. The Vectra mIHC images (**Fig. 4k**, left) and

345   corresponding spatial maps (**Fig. 4k**, right) provide visual validation at the single-cell level that PD-1$^+$

346   CD4$^+$ T cells were closer to tumor cells in responders but closer to Tregs in non-responders.

347   Furthermore, on a per patient basis, the pre-treatment *SpatialScore* was nearly 5-times lower in

348   responders than non-responders (**Fig. 4l**, mean *SpatialScore* R, pre (0.31) versus NR, pre (1.52)), with

349   excellent biomarker performance measures at a *SpatialScore* cutoff point of 0.7908 (**Sup. Fig. 5b-e**).

350   Notably, when calculated per patient, the *SpatialScore* extended over a wider range than when

351   calculated for all cells per group; this is due to sample size differences (i.e., n=7 per patient versus

352   n=1000s of cells per group). It is noteworthy that the skin-derived *SpatialScore* is so robust and

353   predictive of pembrolizumab response, since clinical outcome in advanced CTCL is often driven by the

354   burden of disease in the non-skin compartments (i.e., blood or viscera). Collectively, these results show

355   that findings identified by highly multiplexed imaging platforms like CODEX can be translated to more

356   simplified platforms like Vectra, further demonstrating the clinical utility of the *SpatialScore* as a

357   biomarker predictive of PD-1 blockade outcome in CTCL.

358

359   **Tumor cell-specific CXCL13 expression coincides with a favorable response to PD-1 blockade in CTCL**

360   Potential recruitment mechanisms driving the *SpatialScore* were investigated by identifying

361   genes predictive of the spatial interactions between PD-1$^+$ CD4$^+$ T cells, tumor cells, and Tregs. An L1-

362   regularized linear model was fit to bulk RNA-seq data on a per spot basis, which revealed seven genes

363   predictive of the *SpatialScore* including three chemokines: *CXCL9*, *CCL22* and *CXCL13* (**Fig. 5a**). *CXCL9* and

364   *CCL22* are known to mediate Treg recruitment[56,57]; they had positive coefficients and were predictive of

365   the higher *SpatialScore* seen in non-responders. *CXCL13* is a chemoattractant expressed on benign

366   lymphocytes and CTCL tumor cells[28,58]; it had a negative coefficient and was predictive of the lower

367   *SpatialScore* seen in responders. Bulk *CXCL13* gene expression was significantly increased in responders

368   post- versus pre-treatment and compared to non-responders post-treatment (**Fig. 5b**, median

369   normalized *CXCL13* expression, R, post (615.5) versus NR, post (94.7) and R, pre (16.0)). This

370   upregulation of *CXCL13* in responders post-treatment relative to other patient groups was confirmed by

371   CXCL13 IHC shown quantitatively (**Fig. 5c**, mean CXCL13 IHC expression, R, post (34.5) versus NR, post

372   (7.8) and R, pre (7.6)) and visually (**Fig. 5d**, see R, post for highest expression of CXCL13).

373   We next analyzed a publicly available scRNA-seq dataset of four CTCL skin tumors (Gaydosik et

374   al.)[59] to identify the main cell-type overexpressing *CXCL13*. Using this dataset, we annotated 10 clusters

375   including tumor cells, CD4$^+$ T cells (CD4), Tregs, CD8$^+$ T cells (CD8), B & plasma cells (B&PC), macrophages

376   (mac), dendritic cells (DC), stroma, vasculature (vasc), and keratinocytes (KC) (**Sup. Fig. 6a-b**). Examining

377   all cells with a *CXCL13* log1p normalized read count > 0.5 showed that tumor cells had the highest mean

378   expression compared to other cell-types (**Fig. 5e**, median *CXCL13* expression, tumor (3.3) versus less

379   than 2.0 for the other 9 cell-types). Moreover, the frequency of *CXCL13* expressing cells was highest

380   among tumor cells compared to other cell-types (**Fig. 5f**, mean frequency of *CXCL13* positive cells, tumor

381   (0.27) versus less than 0.1 for the other 9 cell-types).

382   CIBERSORTx (CSx) is a computational framework that uses gene expression signatures to enable

383   cell type-specific gene expression to be inferred from bulk RNA-seq data without physical cell isolation[22].

384   We used CSx to computationally resolve tumor, stromal, and immune cell subsets in bulk RNA-seq data

385   (**Fig. 5g** and **Sup. Table 4**). Using the 10 annotated clusters shown in **Fig. e-f**, a signature matrix,

386   consisting of cell-type specific marker genes, was generated (**Sup. Fig 6c** and see **Methods**, marker genes

387   are shown as rows). This signature matrix was used to enumerate CSx-resolved cell-type fractions and

388   resolve gene expression profiles from CTCL bulk transcriptomes. Strong correlations were observed

389   between most of the CSx-resolved cell-type frequencies and CODEX-identified cell-type frequencies (**Fig.**

390   **5h**, see correlation coefficients along the diagonal of the heatmap).

391   The CSx-resolved gene expression profiles of tumor cells were then thoroughly characterized

392   and compared across patient groups. Interestingly, *RAB11B,* a RAS superfamily member of small GTP-

393   binding proteins, was the only tumor cell gene that was significantly differentially expressed between

394   responders and non-responders pre-treatment (**Sup. Fig. 6d**). This suggests an absence of tumor cell-

395   intrinsic differences between responders and non-responders at baseline. In contrast, numerous genes,

396   including *CXCL13*, were upregulated in tumor cells of responders post-treatment compared to pre-

397   treatment (**Fig. 5i**, see *CXCL13* in bold). This finding is consistent with an increased susceptibility of

398   responder tumor cells to PD-1 blockade therapy, which is supported by the decreased tumor

399   aggressiveness score observed in responders post-treatment relative to pre-treatment (**Fig. 4g**).

400   Interestingly, only three genes (*BRD3*, *TWF2* and *ZNF365*) were differentially expressed in non-

401   responder tumor cells post-treatment compared to pre-treatment (**Fig. 5j**). This suggests that non-

402   responder tumor cells are resistant to PD-1 blockade, which is in line with the increased tumor

403   aggressiveness score observed in non-responders post-treatment compared to pre-treatment (**Fig. 4h**).

404   Finally, co-staining the tissue section used for the Vectra mIHC experiment with a standard IHC anti-

405   CXCL13 antibody, followed by co-localization of tumor cells with CXCL13-positive cells, provided visual

406   confirmation that tumor cells are the primary expressors of CXCL13 (**Fig. 5k, Sup. Fig. 6e**).

407   Next, we assessed *CXCL13* expression in tumor cells and its role in recruiting reactive

408   lymphocytes. CSx-resolved tumor cell-specific *CXCL13* expression was significantly increased in

409   responders post-treatment compared with non-responders post-treatment and responders pre-

410   treatment on a per tissue microarray spot basis (**Fig. 5l**, median normalized tumor cell-specific *CXCL13*

411   expression, R, post (12.64) versus NR, post (11.14) and R, pre (10.54)). On a per patient basis, following

412   PD-1 blockade, tumor cell-resolved *CXCL13* expression increased in 100% of responders (**Fig. 5m**) versus

413   29% of non-responders (**Fig. 5n**). CXCL13 exclusively binds to the chemokine receptor CXCR5, which is

414   expressed on B cells, CD4$^+$ T cells, CD8$^+$ T cells, and skin-derived migratory dendritic cells[60]. Although not

415   significant, *CXCR5* expression was increased in bulk mRNA of responders post-treatment relative to pre-

416   treatment (**Sup. Fig. 6f**). The data lacked significant power to unmix *CXCR5* on CD4$^+$ T cells by CSx;

417   however, tumor cell-specific *CXCL13* expression was positively correlated (Spearman correlation

418   coefficient = 0.68) with bulk mRNA *CXCR5* expression (**Fig. 5o**), suggesting a chemoattractant

419   recruitment mechanism.

420   Collectively, these results indicate that PD-1 blockade distinctly alters the CTCL TME of

421   therapeutic responders and non-responders. In responders, pembrolizumab therapy promotes immune

422   activation and upregulates CXCL13 in tumor cells (**Fig. 6**, top panel). CXCL13 overexpression then attracts

423   effector/cytotoxic PD-1$^+$CD4$^+$T cells to tumor cells, promoting CD4$^+$ T cell-mediated tumor cell inhibition

424   and killing. As such, the overexpression of CXCL13 in tumor cells provides a mechanism for the sustained

425   clinical activity seen in responders. In contrast, non-responders have a persistently immunosuppressed

426   TME, which mediates the increased interaction between inhibitory Tregs and PD-1$^+$ CD4$^+$ T cells and

427   maintains this CD4$^+$ T cell subset in an exhausted state (**Fig. 6**, bottom panel). In the setting of

428   pembrolizumab resistance, non-responder tumor cells remain active and proliferative following

429   treatment. Thus, underlying differences in the functional immune state of the TME—coupled with

430   alterations in CD4$^+$ T cell effector activity versus suppression, and tumor cell-specific CXCL13

431   expression—are associated with distinct spatial cellular patterns that predict the efficacy of PD-1

432   blockade in CTCL.

433

434   **DISCUSSION**

435   For anti-PD-1 immunotherapies to provide maximal benefit to cancer patients, the drivers and

436   resistors of clinical response must be identified. Traditional biomarker studies with IHC, gene expression

437   profiling, and tumor mutational burden assays do not fully account for spatial cellular context and have

438   imperfect correlation with immunotherapy outcomes[16]. This was true for our CTCL cohort: No pre-

439   treatment differences were observed in immune composition, expression of PD-1/PD-L1 proteins, or

440   IFN-γ/TGF-β gene signatures between responders and non-responders. We therefore explored

441   alternative approaches, including spatially resolved multiplexed tissue imaging, which has been shown

442   to significantly improve the accuracy of predicting response to PD-1 blockade in several tumor types[61].

443   Multiparameter histologic analysis revealed global prognostic spatial patterns that were

444   predictive of clinical response, including a localized enrichment of tumor and CD4^{+} T cells (CN-8) in

445   responders and of Tregs (CN-10) in non-responders. Profiling the spatial relationships between effector

446   PD-1^{+} CD4^{+} T cells, tumor cells, and immunosuppressive Tregs allowed us to derive the *SpatialScore*—a

447   clinically useful biomarker that correlated strongly with pembrolizumab response in CTCL. Previously

448   identified spatial biomarkers rely on pairwise distances (e.g., PD-1^{+} T cells and PD-L1^{+} tumor cells)[17,62,63],

449   whereas the *SpatialScore* accounts for the interactions between three functionally distinct cell-types. As

450   such, the *SpatialScore* represents a novel predictive approach and provides insight into three key

451   therapeutic determinants underlying PD-1 blockade in CTCL: 1) functional immune state of the TME, 2) T

452   cell function, and 3) chemoattraction.

453   First, the *SpatialScore* captures differences in the functional immune phenotypes between

454   responders and non-responders. Following pembrolizumab therapy, the TME of responders becomes

455   activated, as evidenced by the increased immune activation gene score, increased frequency of ICOS^{+}

456   and Ki-67^{+} CD4^{+} T cells, and a local enrichment of tumor cells with dendritic cells (CN-5) and CD4^{+} T cells

457   (CN-8). These findings suggest that in responders PD-1 blockade specifically activates CD4^{+} T cells

458   through the expression of immunostimulatory molecules and co-stimulation by antigen-presenting cells,

459   resulting in CD4^{+} T cell proliferation[64,65]. In contrast, non-responders have a persistently

460   immunosuppressed TME. This is supported by the increased frequency of a Treg enriched neighborhood

461   (CN-10) and the expansion of a highly suppressive ICOS[+] Treg subset, which has been associated with

462   poor clinical outcomes in melanoma[43] and liver cancer[44]. These results suggest that the increased

463   suppressive function and spatial organization of Tregs in non-responders account for the strong

464   immunosuppression and lack of pembrolizumab response. We speculate that the absence of this pre-

465   treatment immunosuppression in responders enables priming and activation of CD4^{+} T cells following

466   immunotherapy.

467   Second, the *SpatialScore* reflects differences in T cell function between responders and non-

468   responders: After PD-1 blockade, T cell effector activity is restored in responders, whereas non-

469   responders have a continually exhausted T cell phenotype. Consistent with studies of Hodgkin

470   lymphoma[63], bladder cancer[50], and glioblastoma[66], our data suggest that CD4+ T cells, and particularly

471   the PD-1+CD4+ T cell subset, are crucial effectors that influence pembrolizumab efficacy in CTCL. In

472   responders post-treatment, PD-1+CD4+ T cells increase GZMB expression and move closer to tumor cells,

473   similar to the granzyme-perforin-dependent tumor killing mechanism used by cytotoxic CD8+ T cells[45-48].

474   Previous studies have shown that antitumor activity is enhanced by a closer proximity of cytotoxic T cells

475   to tumor cells[67,68] and by removing inhibitory Tregs from the TME milleu[50]. The *SpatialScore* combines

476   these principles by measuring the physical distances between PD-1+ CD4+ T cells and tumor cells (i.e.,

477   effector function) as well as PD-1+ CD4+ T cells and Tregs (i.e., suppressive function). The *SpatialScore*

478   therefore reflects the balance of T cell effector activity versus suppression in the TME and the efficacy of

479   PD-1 blockade in CTCL.

480   Third, pembrolizumab therapy leads to increased RNA and protein expression of CXCL13 in

481   responder tumor cells (or kills cells with lower levels of expression), which may be advantageous in

482   localizing effector PD-1+CD4+ T cells within the TME. Overexpression of *CXCL13* is associated with

483   improved clinical outcomes in breast[69], colon[70], ovarian[71], lung[72], and urothelial cancers[73] as well as

484   responsiveness to anti-PD-1 immunotherapy[72,74]. Additionally, upregulation of *CXCL13* can be

485   accompanied by constitutive protein secretion[69,72], which strongly attracts CXCR5+CD4+ T cells[72] and PD-

486   1+CD4+ T cells[75] to the tumor site. A recent study also showed that the tumor-specific gene expression

487   program of cytotoxic GZMB+CD4+ T cells in bladder cancer treated with anti-PD-L1 therapy was marked

488   by tumor overexpression of *CXCL13*[50]. Furthermore, CXCL13 null mice with bladder tumors did not

489   respond to anti-PD-1 treatment and had a lower frequency of T cell infiltration compared their wild-type

490   counterparts[73]. Collectively, these findings support a chemoattractant mechanism for the sustained

491   clinical response to pembrolizumab therapy observed in responders: Upregulation of CXCL13 in tumor

492   cells attracts effector PD-1$^+$CD4$^+$ T cells to them, promoting successful antitumor activity. This aspect of

493   pembrolizumab responsiveness is captured by the lower *SpatialScore* seen in responders and

494   underscores the importance of T cell topography as a spatial biomarker.

495   There are important limitations to this study. Discovery of the *SpatialScore* was based on 14

496   patients. Larger studies are needed to determine if this spatial biomarker translates broadly for

497   prediction of pembrolizumab response in CTCL and to establish a threshold value for the *SpatialScore*

498   that can be used to stratify patients into probabilistic responders and non-responders. Additionally,

499   larger studies might delineate more subtle features of the spatial architecture not detected in this study.

500   Another limitation of this study is that the post-treatment tumor biopsies were collected at various time

501   points, impairing our ability to directly assess modulation of T cell subsets at the precise time of

502   therapeutic success or failure. Finally, our cohort is limited to advanced, heavily pre-treated CTCL

503   patients. Further efforts should examine the therapeutic activity of PD-1 blockade in early stage and

504   treatment naïve patients, since early tumors are generally more responsive to immunotherapy [76-81] and

505   prior systemic treatment may alter the immune response to therapy. Despite these limitations, the

506   robustness of our findings highlights that spatial organization and immune functionality are conserved in

507   responders and non-responders, which reinforces the importance of these factors for determining

508   pembrolizumab response in CTCL.

509   Future studies with scRNA-seq and paired T cell receptor sequencing are needed to better

510   characterize the heterogeneity of PD-1$^+$CD4$^+$ T cells across patient groups and to fully understand the

511   cytotoxic potential of this crucial effector subset. Similarly, investigating the increased suppressive

512   function of Tregs and the ICOS$^+$ Treg subset in non-responders may reveal vulnerabilities that could be

513   targeted in combination with PD-1 blockade. Given our findings that non-responders have an increased

514   localization of Tregs and upregulation of *BRD3*, an epigenetic regulator, in their tumor cells pre-

515   treatment, future studies should investigate the therapeutic potential of combining mogamulizumab

516   (which depletes Tregs[82]) and/or bromodomain inhibitors (which inhibit BRD3 and decrease tumor cell

517   proliferation[83]) with pembrolizumab therapy for CTCL. Further studies are also required to determine if

518   CXCL13 expression levels—in both skin and blood—can serve as a surrogate of pembrolizumab activity

519   and therefore guide ongoing treatment decisions. Such studies are especially important for advanced

520   CTCL patients, where the burden of disease in the non-skin compartments often dictate clinical

521   outcome.

522   This work provides an important conceptual foundation for improving the efficacy of anti-PD-1

523   immunotherapy in CTCL. We identify effector PD-1$^+$CD4$^+$ T cells in responders and inhibitory ICOS$^+$Tregs

524   in non-responders. The *SpatialScore* captures the interactions of these cell-types with tumor cells and

525   reveals how PD-1 blockade manipulates the balance of effector and suppressive T cell function to

526   achieve disease control. We anticipate that the cell-types comprising the *SpatialScore* will depend on the

527   specific cancer and immunotherapy. The *SpatialScore* biomarker approach and the ability to measure it

528   using a clinically accessible mIHC platform should enable its widespread use in cancer immunotherapy

529   studies.

530
531
532

533   **METHODS**

534   **Human subjects and clinical trial study design.** The CITN-10 trial was a multicenter, phase II, single-arm

535   clinical trial that investigated the efficacy of pembrolizumab in 24 patients with two common forms of

536   relapsed/refractory CTCL, mycosis fungoides and Sézary syndrome[13]. Written informed consent was

537   obtained from all enrolled patients. The use of their tissues for research was fully de-personalized and

538   approved by the Stanford University IRB Administrative Panels on Human Subjects in Medical Research

539   (HSR 46894). All patients had a clinicopathologically confirmed diagnosis of mycosis fungoides or Sézary

540   syndrome (clinical stage IB to IV) that had relapsed, was refractory to, or had progressed after at least

541   one standard systemic therapy. Exclusion criteria included central nervous system disease, active

542   autoimmune disease, previous exposure to any anti-PD-1, anti-PD-L1, or anti-PD-L2 therapy, or

543   treatment with radiotherapy or other anti-cancer agents within 15 weeks of the pre-treatment biopsy.

544   Topical medications were not applied to the biopsied areas during treatment or within 8 weeks of the

545   pre-treatment biopsy. Patients were treated with 2 mg/kg pembrolizumab by intravenous infusion every

546   3 weeks for up to 24 months[13]. Response and primary end point (overall response rate) were assessed

547   by consensus global response criteria[23].

548

549   **Sample collection and tissue microarray construction.** Skin biopsy specimens were collected from the

550   primary tumor site and FFPE histology blocks were generated according to standard pathology

551   procedures. Pre-treatment biopsies were obtained prior to the first pembrolizumab infusion and post-

552   treatment biopsies were collected during and at the conclusion of therapy (**Sup. Fig. 1, Sup. Table 1**).

553   H&E-stained sections from all biopsies were reviewed by two board-certified pathologists (C.M.S. and

554   R.H.P.). Fourteen of the 24 biopsy samples had adequate FFPE material to be assembled into a tissue

555   microarray, and two to three cores of 0.6 mm diameter from the most infiltrated regions of each biopsy

556   were digitally annotated and compiled into a tissue microarray. The tissue microarray was sectioned at

557   4-μm thickness and mounted onto Vectabond[TM]-treated (Vector Labs, #SP-1800) square glass coverslips

558   (22x22 mm, #1 1/2, Electron Microscopy Sciences, #72204-01).

559

560   **Immunohistochemistry.** IHC for CD3 (clone CD3-12; Abd Serotec), CD4 (clone 4B12; Leica), CD8 (clone

561   CD8/144B; Dako), FoxP3 (clone 236A/E7; Abcam), CD163 (clone 10D6; Thermo Fisher Scientific), PD-1

562   (clone NAT105; Cell Marque), PD-L1 (clone 22C3; Merck Research Laboratories), and PD-L2 (clone 3G2;

563   Merck Research Laboratories) was performed as previously described[84]. Images were scored by CITN

564   pathologists, and the positive percentage of the total mononuclear cell infiltrate was reported[13].

565

566   **Multiplex immunohistochemistry and analysis**. mIHC was performed as previously described[85]. Briefly,

567   4-μm FFPE tissue sections were baked for 1 h at 60 °C, dewaxed, and stained on a BOND Rx autostainer

568   (Leica) according to Opal Multiplex IHC assay (Akoya Biosciences)s protocol with the following changes:

569   additional high stringency washes were performed after the secondary antibody and Opal fluor

570   applications using high-salt TBST (0.05M Tris, 0.3M NaCl and 0.1% Tween-20, pH 7.2-7.6), and TCT was

571   used as the blocking buffer (0.05M Tris, 0.15M NaCl, 0.25% Casein, 0.1% Tween 20, pH 7.6 +/- 0.1). The

572   antibody panel was stained in the following order, with antibody stripping between positions. Each

573   primary antibody was incubated for 60 min, followed by 10-min incubation with secondary antibody

574   (OPAL polymer HRP mouse plus rabbit, Akoya Biosciences), followed by application of the tertiary TSA-

575   amplification reagent (OPAL Fluor, Akoya Biosciences) for 10 min. Positions were as follows: position 1:

576   CD8 (clone CD8/144B, DAKO #M7103; concentration 0.8 µg/ml; OPAL Fluor 520); position 2: CD25 (clone

577   4C9, Cell Marque #125M-14; concentration 0.17 µg/ml; OPAL Fluor 540); position 3: CD3 (clone SP7,

578   Thermo Fisher Scientific #RM-9107; concentration 0.06 µg/ml; OPAL Fluor 570); position 4: PD-1 (clone

579   EPR4877(2), Abcam #ab137132, concentration 1.0 µg/ml; OPAL Fluor 650); position 5: CD7 (clone MRQ-

580   56; Cell Marque #107M-24; concentration 1.18 µg/ml; OPAL Fluor 690); position 6: CD4 (clone EP204,

581   Epitomics; #AC0173A; concentration 0.08 µg/ml; OPAL Fluor 480); and position 7: FoxP3 (clone 236A/E7;

582   eBioscience #14-4777-82; 5.0 µg/ml; OPAL Fluor 620). Subsequently, slides were stained with Spectral

583   DAPI (Akoya Biosciences) for 5 min, rinsed, and mounted with Prolong Gold Antifade reagent (Thermo

584   Fisher Scientific #P36930). After curing for 24 h at room temperature in the dark, images were acquired

585   on a Vectra Polaris automated quantitative pathology imaging system (Akoya Biosciences). The raw

586   images were spectrally unmixed using the Phenoptics inForm software (Akoya Biosciences) and

587   exported as multi-image TIFF files.

588   After fluorescent imaging, the slides were de-coverslipped, loaded onto the BOND Rx

589   autostainer, stripped of bound antibody, and a post-mIHC staining for CXCL13 (goat polyclonal, R&D

590   Systems #AF801; concentration 0.5 µg/ml; incubation 60 min) was performed. Bound antibody was

591   revealed by anti-goat HRP secondary ImmPress HRP (Vector Labs #MP-7405; incubation 12 min),

592   followed by DAB chromogen using the BOND Polymer Refine Detection kit (Leica) according to the

593   manufacturer's instructions. After counterstaining with hematoxylin, slides were dry-mounted and

594   scanned on an Aperio AT turbo digital slide scanning system (Leica).

595   HALO software (Indica Labs) was used to perform single-cell analysis of mIHC images. Cells were

596   visualized based on nuclear and cytoplasmic stains, and mean pixel fluorescence intensity in the

597   applicable compartments of each cell were measured (i.e., CD4 in the cytoplasmic compartment and

598   FoxP3 in the nuclear compartment). A mean intensity threshold above background was used to

599   determine positivity for each fluorochrome, thereby defining cells as either positive or negative for each

600   marker. The data was then used to define co-localized populations, including PD-1$^+$ CD4$^+$ T cells, tumor

601   cells, and Tregs. Spatial positions were extracted for each cell, and the spatial distances and ratios

602   between these three cells types were calculated as detailed below. Performance of the *SpatialScore*

603   biomarker was evaluated with the easyROC interface available with the R package shiny[86]. CXCL13 IHC

604   images were scored using a classifier method for the DAB stain based on optical density to obtain the

605   positive percentage of the total mononuclear cell infiltrate per spot.

606

607   **CODEX antibodies.** For CODEX, purified, carrier-free monoclonal and polyclonal anti-human antibodies

608   were purchased from commercial vendors (**Sup. Table 1**). Conjugations to maleimide-modified short

609   DNA oligonucleotides (TriLink) were performed at a 2:1 weight/weight ratio of oligonucleotide to

610   antibody, with at least 100 µg of antibody per reaction, as previously described[19]. Conjugated antibodies

611   were validated and titrated under the supervision of a board-certified pathologist (C.M.S.).

612

613   **CODEX multiplex tissue staining and imaging.** The CODEX experiment was performed as previously

614   described[19]. Briefly, the coverslip was deparaffinized and rehydrated, and heat-induced epitope retrieval

615   was performed using Dako target retrieval solution, pH 9 (Agilent, #S236784-2) at 97 °C for 10 min. The

616   coverslip was stained with an antibody cocktail (**Sup. Table 2**) to a volume of 100 µl overnight at 4 °C in a

617   sealed humidity chamber on a shaker. After multiple fixation steps using 1.6% paraformaldehyde, 100%

618   methanol, and BS3 (Thermo Fisher Scientific, #21580), the coverslip was mounted onto a custom-made

619   acrylic plate (Bayview Plastic Solutions). Imaging was performed with a Keyence BZ-X710 inverted

620   fluorescence microscope equipped with a CFI Plan Apo λ 20x/0.75 objective (Nikon), an Akoya CODEX

621   microfluidics instrument, and CODEX driver software (Akoya Biosciences). Light exposure times and the

622   arrangement of cycles are outlined in **Sup. Table 2**. At the conclusion of the CODEX multicycle reaction,

623   H&E staining was performed, and images were acquired in brightfield mode.

624

625   **Data processing of CODEX images.** Raw TIFF image files were processed using the CODEX Toolkit as

626   previously described. After processing, the staining quality for each antibody was visually assessed in

627   each tissue microarray spot, and cell segmentation was performed using the DRAQ5 nuclear stain.

628   Marker expression was quantified, and single-cell data were saved as FCS files, which were then

629   imported into CellEngine (https://cellengine.com) for cleanup gating. This resulted in a total of 117,170

630   cells across all tissue microarray spots.

631   After cleanup gating, FCS files were exported from CellEngine, imported into VorteX clustering

632   software[87], and subjected to unsupervised X-shift clustering using an angular distance algorithm.

633   Clustering was based on all antibody markers except CD11b, CD16, CD164, CCR4, CCR6, EGFR, and p53.

634   The optimal cluster number was guided by the elbow point validation tool in VorteX, resulting in 78

635   clusters. Clusters were manually verified and assigned to cell-types based on morphology in H&E and

636   fluorescent CODEX images and on their marker expression profiles. Clusters with similar features were

637   merged, resulting in 21 cell-type clusters. The expression frequencies of ICOS, IDO, Ki-67, and PD-1 were

638   determined for the T cell and tumor cell clusters by manual gating in CellEngine for each tissue

639   microarray spot, with visual comparison to the raw fluorescent image.

640

641   **Cellular neighborhood identification.** CN identification was performed using a custom *k*-nearest

642   neighbors' algorithm in Python[19]. For each of the 117,220 cells in this experiment, the window size was

643   set at 10, capturing the center cell and its nine nearest neighboring cells, as measured by the Euclidean

644   distance between X/Y coordinates. To identify 10 CNs, these windows were then clustered by the

645   composition of their microenvironment with respect to the 21 cell-types that were previously identified.

646   This resulted in a vector for each window containing the frequency of each of the 21 cell-types amongst

647   the 10 neighborhoods. These windows were then clustered using Python's *scikit-learn* implementation

648   of MiniBatchKMeans with k=10. Each cell was then allocated to the same CN as the window in which it

649   was centered. All CN assignments were validated by overlaying them on the original fluorescent and

650   H&E-stained images.

651

652   **Calculation of spatial distances and ratios between cell-types**. The X/Y coordinates for each cell type

653   were determined during cellular segmentation, as described above. The minimal distance between each

654   cell-type and its nearest other cell-types, and the averages of these minimal distances per tissue spot,

655   were calculated in R. Given our interest in the relationship of cell distances between three cell-types

656   (i.e., effector T cells (CT1), tumor cells (CT2) and Tregs (CT3)), we calculated the ratio of the minimal

657   distances between CT1—CT2 (right distance) versus CT1—CT3 (left distance). This distance ratio

658   represented the *SpatialScore*. To assess whether these ratios were significantly different from those of a

659   random sample, we performed the following analysis per spot: For the number of CT1 cells in each spot,

660   we randomly selected the same number of non-CT1 (nCT1) cells. For each of these nCT1 cells, we

661   calculated the ratio of the minimal distances (nCT1—CT2 / nCT1—CT3) and determined the mean of this

662   sample. We repeated this random sampling 100 times, and the average of all the means was reported.

663   Distribution of the random values was assessed by the quant output variable, which indicates how many

664   of the random means are smaller than the measured means. For instance, a quant of 97 indicates that

665   97% of the random means are smaller than the measured means. Thus, quant values closer to 100 or 0

666   indicate that the measured means are not random (**Sup. Fig. 4j-m**).

667

668 **Laser-capture microdissection (LCM).** Two serial sections of the tissue microarray were taken at 7 μm

669 thickness and mounted onto frame slides with polyethylene naphthalate membranes (Thermo Fisher

670 Scientific, #LCM0521). Slides were immersed for 20 s each in xylene (three times), 100% ethanol (three

671 times), 95% ethanol (two times), 70% ethanol (two times), water, hematoxylin (Dako, #S3309), water,

672 bluing reagent (Thermo Fisher Scientific, #7301), water, 70% ethanol (two times), 95% ethanol (two

673 times), 100% ethanol (three times), and xylene (three times). Immediately after staining, cells were

674 dissected from every tissue microarray spot on an ArcturusXT LCM System (Thermo Fisher Scientific)

675 using the ultraviolet laser to cut out the desired region and the infrared laser to adhere the membrane

676 to a CapSure HS LCM Cap (Thermo Fisher Scientific, #LCM0215). A tissue area containing roughly 1000

677 mononuclear cells was captured from each spot, with cell numbers determined based on density

678 estimates by cell counting in an adjacent H&E-stained section. If a core had more than 1000

679 mononuclear cells, a tissue fragment containing around 1000 mononuclear cells was dissected from that

680 core. If a core had less than 1000 cells, tissue fragments from corresponding cores on the serial section

681 membrane were combined in the same LCM cap to obtain approximately 1000 cells. After

682 microdissection, the caps were sealed using 0.5-ml tubes (Thermo Fisher Scientific, #N8010611) and

683 stored at -80 °C until cDNA library preparation.

684

685 **Preparation of cDNA libraries and RNA sequencing.** Sequencing libraries were prepared according to

686 the Smart-3Seq protocol for LCM HS caps, as previously described with slight modifications[21]. Briefly, 10

687 μl of lysis mix consisting of 40% (v/v) 5 M trimethylglycine solution (Sigma, #B0300), 20% (v/v) 10 mM

688 nuclease-free dNTP mix (Thermo Fisher Scientific, #R0192), 10% (v/v) 20 μM first-strand primer in TE

689 buffer (1S, /5Biosg/GT GAC TGG AGT TCA GAC GTG TGC TCT TCC GAT CTT TTT TTT TTT TTT TTT TTT TTT

690 TTT TTT TV; Integrated DNA Technologies), 10% (v/v) Triton-X 100 (Sigma #T8787; diluted to 0.5% v/v in

691 molecular biology-grade water), and 20% (v/v) Proteinase K (New England Biolabs, #P8107S; diluted to

692 0.125 mg/ml in in molecular biology-grade water) was added to the center of each LCM cap. Caps were

693   sealed with 0.2 ml low-retention PCR tubes (Corning, #PCR-02-L-C) and incubated on a pre-warmed

694   metal CapSure incubation block (Thermo Fisher Scientific, #LCM0505) at 60 °C in an incubator. Then,

695   tubes were briefly centrifuged, and 10 µl of template-switching reverse-transcription (TS-RT) FFPE LCM

696   mix consisting of 40% (v/v) 5x SMARTScribe first-strand reaction buffer (Clontech, #639537), 20% (v/v)

697   20 mM DTT (Clontech, #639537), 10% (v/v) 20x RNase inhibitor (Thermo Fisher Scientific, #AM2694), 4%

698   (v/v) 50 µM second-strand primer in TE buffer (2S, /5Biosg/CT ACA CGA CGC TCT TCC GAT CTN NNN

699   NrGrG rG; Integrated DNA Technologies), 4% (v/v) 200 mM MgCl$_2$ (Sigma, #63069), 2% 5 mM proteinase

700   K inhibitor (EMD Millipore, #539470), and 20% (v/v) 100 U/µl SMARTScribe reverse transcriptase

701   (Clontech, #639537) was added. Samples were incubated in a programmable thermal cycler (42 °C for 30

702   min, 70 °C for 10 min, 4 °C hold), and 1.25 µl of a unique P5 primer and 1.25 µl of a universal P7 primer

703   (2 µM in TE buffer each; Integrated DNA Technologies; sequences available upon request) and HiFi

704   HotStart ReadyMix (Kapa, #KK2601) were then added, followed by 22 cycles of PCR amplification (98 °C

705   for 45 s; 22 cycles at 98 °C for 15 s, 60 °C for 30 s, 72 °C for 10 s; then 72 °C for 60 s, and 4 °C hold).

706   Amplified cDNA was next purified with SPRI bead mix (Beckman Coulter, #B23317) and a magnetic

707   separation block (V&P Scientific, #VP772F4). Finally, the samples were washed with 80% ethanol and

708   resuspended in TE buffer to yield the sequencing-ready library.

709   Libraries were profiled for size distribution on an Agilent 2200 TapeStation with High Sensitivity

710   D1000 reagent kits and quantified by qPCR with a dual-labeled probe as previously described[88]. Libraries

711   were excluded if <40% of their transcripts were within a 165-500 bp range. A total of 64 libraries were

712   mixed to equimolarity, according to the qPCR measurements. The RNA libraries were sequenced on an

713   Illumina NextSeq 500 instrument with a High Output v2.5 reagent kit (Illumina, #20024906) to a

714   minimum sequencing depth of1.5 M reads per sample (mean: 3.7 M) and minimum uniquely aligned

715   reads of 364,468 per sample (mean: 916,607) using read lengths of 76 nucleotides (nt) for read 1 and 8

716   nt for read 2. On average, we obtained reads from 11,166 genes per sample (median: 11,267) and

717 379,615 unique transcripts per sample (median: 336,005), which is comparable to previously published

718 FFPE-based RNA-seq studies of human cancers[21].

719

720 **Processing of RNA-seq data**. Base calls from the NextSeq were de-multiplexed and converted to FASTQ

721 format with bcl2fastq (Illumina). The five-base unique molecular identifier (UMI) sequence and the G-

722 overhang were extracted from FASTQ data, and A-tails were removed with umi_homopolymer.py

723 (github.com/jwfoley/3SEQtools). Reads were aligned and further processed to remove duplicates using

724 STAR (github.com/alexdobin/STAR). Bulk gene expression profiles were transcript per million (TPM)

725 normalized and log2 transformed. Differences in *CXCL13* and *CXCR5* expression between groups were

726 modeled with Linear Mixed Effects Models on a per spot basis using the lmer function from package

727 lme4 (v1.1.21)[89] and taking the patient intercept as a random effect. The pairwise p-values were derived

728 from t-ratio statistics in the contrast analysis using the lmerTest (v3.1.2)[90] and corrected for multiple

729 hypothesis testing using the Holm Bonferroni method implemented in the modelbased (v0.1.2) package

730 (github.com/easystats/modelbased).

731

732 **Principal component analysis (PCA) immune scores.** PCA scores and principal component 1 (PC1)

733 coefficients were computed for the normalized bulk RNA-seq data on a per spot basis using the prcomp

734 function in base R. The IFN-γ score was calculated using the six gene signature published by Ayers et

735 al.[39]. The TGF-β score was calculated using the 15 gene signature published by Mariathasan et al.[40]. The

736 immune activation and immunosuppression scores were computed using the genes listed in **Fig. 2g**.

737 Differences in PC1 scores between patient groups were modeled using Linear Mixed Effects Models on a

738 per spot basis using the lmer function from package lme4 (v1.1.21)[89] and taking the patient intercept as

739 a random effect. Differences between responders and non-responders as well as pre-treatment and

740 post-treatment samples were modeled as fixed effects and tested using Satterthwaite's degrees of

741 freedom method. The pairwise *p* values were derived from t-ratio statistics in the contrast analysis using

742   the lmerTest (v3.1.2)[90] and corrected for multiple hypothesis testing using the Holm Bonferroni method

743   implemented in the modelbased (v0.1.2) package (github.com/easystats/modelbased).

744

745   **Identifying bulk RNAseq gene signatures associated with tumor cells and the *SpatialScore*.** LASSO

746   regression models were used to find genes predictive of tumor cells and the *SpatialScore*. These models

747   were estimated using the LassoCV object in the scikit-learn python package. Six-fold cross validation was

748   used to select the optimal regularization parameter. Specifically, an L1-regularized linear model was fit

749   to predict the frequency of tumor cells from the gene expression data per tissue microarray spot. For

750   this model, the response variable was the log transformed per spot percentage of tumor cells. A pseudo-

751   count of 1% was added to genes. The features utilized as predictors were the per spot log transformed

752   TPM counts and the log frequency of $CD4^+$ T cells. Genes with positive nonzero coefficients were

753   interpreted as positively associated with tumor cells. Similarly, an L1-regularized linear model was fit to

754   predict the *SpatialScore* from the gene expression data on a per spot basis. For this model, the response

755   variable was the log transformed *SpatialScore* distance ratio. The features used as predictors were the

756   per spot log transformed TPM counts. Genes with nonzero coefficients were selected in figures as

757   predictive.

758

759   **CIBERSORTx signature matrix.** To generate a CSx signature matrix, we used a publicly available scRNA-

760   seq dataset from Gaydosik et al.[59] that was obtained from skin biopsies of five CTCL patients. Datasets

761   were downloaded from the Gene Expression Omnibus (GEO) database (accession code GSE128531), and

762   single-cell profiles were combined and analyzed using the Seurat R package (3.1.4)[91]. Cells with between

763   500 and 7500 genes detected and less than 10% mitochondrial transcripts were included in the analysis.

764   Data were log10normalized and clustered with the Louvain method[92] based on the first 13 PCs

765   and resolution of 1.8. Cell clusters were visualized using Uniform Manifold Approximation and

766   Projection (UMAP)[93], with the same PCs. Major cell-types were assigned according to expression of

767   corresponding marker genes (**Sup. Fig. 6a, Sup. Table 4**). Fibroblasts and pericytes were merged into a

768   stromal cluster. The T cell cluster was divided into CD4$^+$ T cells, CD8$^+$ T cells, Tregs, and tumor cells based

769   on the expression of certain T cell and tumor marker genes (**Sup. Fig 6b, Sup. Table 4**). Tumor cells from

770   patient CTCL-5 were excluded due to extreme heterogeneity. T cell clustering was based on the first 15

771   PCs and resolution of 1.9. The same PCs were used to generate UMAP projections for the T cell clusters.

772   A matrix of single cells and their assigned cell-type identities was used to create a signature matrix using

773   the CSx (v.1.0) website[22] (code available from https://cibersortx.stanford.edu/). There was good

774   correlation between the CSx and CODEX cell-type clusters (**Sup. Fig 5c**).

775

776   **CIBERSORTx deconvolution.** The signature matrix was used to deconvolve tumor cell gene expression in

777   CSx (v.1.0) with the CSx website (arguments used: rmbatchSmode = T, QN = F)[22]. Log2 fold changes were

778   computed for every deconvolved gene across patient groups. Differences in gene expression between

779   patient groups were modeled with Linear Mixed Effects Models on a per spot basis using the lmer

780   function from package lme4 (v1.1.21)[89] and taking the patient intercept as a random effect. The *p*

781   values were derived using Satterthwaite's degrees of freedom method, implemented in the lmerTest

782   (v3.1.2)[90] package. The *p* values were adjusted with the Benjamini-Hochberg correction using the

783   p.adjust function in R. Volcano plots were generated using the ggplot2 (3.3.0)[94] and ggrepel (0.8.1)[95]

784   packages in R. Genes with Benjamini-Hochberg-adjusted *p* < 0.1 were considered significant (**Fig. 5i-j,**

785   **Sup. Fig. 5d**).

786   CSx-deconvolved *CXCL13* expression in tumor cells was log2 transformed on a per spot basis.

787   Differences in *CXCL13* expression between patient groups were modeled using Linear Mixed Effects

788   Models on a per spot basis using the lmer function from package lme4 (v1.1.21) and taking the patient

789   intercept as a random effect. The pairwise *p* values were derived from t-ratio statistics in the contrast

790   analysis using the lmerTest (v3.1.2) and corrected for multiple hypothesis testing using the Holm

791   Bonferroni method implemented in the modelbased (v0.1.2) package

792 (github.com/easystats/modelbased). To examine *CXCL13* expression in tumor cells on a per patient

793 basis, the mean from biological replicates was computed before plotting the log2 normalized CSx-

794 deconvolved *CXCL13* expression. The Wilcoxon signed-rank test was used to evaluate whether patient-

795 matched CSx-deconvolved CXCL13 expression in the tumor cells was different between groups.

796

797 **Statistical analysis.** Statistical analyses were performed with R and Prism v8 (GraphPad Software, Inc).

798 Results with $p < 0.05$ were considered significant, unless otherwise stated. For pre-treatment differences

799 between responders and non-responders, the significance was tested using a two-sided Wilcoxon's

800 rank-sum test. For differences across patient groups (i.e., responders and non-responders pre-

801 treatment, responders pre- and post-treatment, non-responders pre- and post-treatment, and

802 responders and non-responders post-treatment), the significance was tested using a linear mixed-effect

803 model with Bonferroni's corrections for multiple comparisons. Pre- to post-treatment pairwise statistical

804 significance for individual patients was tested using a two-sided Wilcoxon's signed-rank test.

805 Correlations were evaluated with the non-parametric Spearman test. The investigators were not blinded

806 to allocation during experiments and outcome assessment. No sample-size estimates were performed to

807 ensure adequate power to detect a pre-specific effect size. $*p < 0.05$, $**p < 0.01$, $***p < 0.001$,

808 $****p < 0.0001$.

809

810 **DATA AVAILABILITY.** Upon acceptance, raw CODEX data will be deposited in a public repository at The

811 Cancer Imaging Archive (TCIA). RNA-seq data generated in this study have been deposited in the GEO

812 database, with accession code GSE162137 (secure reviewer token: snmnyuqqppefpor).

813

814 **CODE AVAILABILITY.** Cellular neighborhood code:

815 https://github.com/nolanlab/NeighborhoodCoordination. Code used to calculate the physical distances

816   between cell-types will be uploaded to the Nolan Lab github page upon acceptance. CIBERSORTx:

817   https://cibersortx.stanford.edu/.

818

844

845 AUTHOR CONTRIBUTIONS

846   D.P. and C.M.S. conceived of the study. D.P., M.M., B.R.G., S.S.B., G.L.B., S.J., J.D., K.S.S., Y.G., and C.M.S.

847   performed experiments and analyzed data. R.H.P, S.P.F., N.R., and M.A.C. provided clinical samples and

848   created the tissue microarray. M.S.K. and Y.H.K coordinated trial protocols and provided clinical data.

849   G.P.N. guided experiments and data analysis, with assistance from R.B.W. D.P. and G.P.N. wrote the

850   manuscript, with input from all authors. All authors vouch for the accuracy of the data reported and

851   approve the manuscript.

852

853

854 COMPETING INTERESTS

855   G.P.N. and Y.G. are co-founders and stockholders of Akoya Biosciences, Inc. and inventors on patent

856   US9909167. D.P., C.M.S., and G.P.N. are inventors on pending patent US62971722, filed by Stanford

857   University. C.M.S. is a scientific advisor to Enable Medicine, LLC. Y.H.K. received research funding from

858   Merck & Co. The other authors declare no competing interests.

859

860 REFERENCES

861   1   Willemze, R. *et al.* The 2018 update of the WHO-EORTC classification for primary cutaneous
862   lymphomas. *Blood* **133**, 1703-1714, doi:10.1182/blood-2018-11-881268 (2019).

863   2   Scarisbrick, J. J. *et al.* Cutaneous Lymphoma International Consortium Study of Outcome in
864   Advanced Stages of Mycosis Fungoides and Sezary Syndrome: Effect of Specific Prognostic
865   Markers on Survival and Development of a Prognostic Model. *J Clin Oncol* **33**, 3766-3773,
866   doi:10.1200/JCO.2015.61.7142 (2015).

867 3   Wilcox, R. A. Mogamulizumab: 2 birds, 1 stone. *Blood* **125**, 1847-1848, doi:10.1182/blood-2015-
868   02-625251 (2015).

869 4   Postow, M. A., Callahan, M. K. & Wolchok, J. D. Immune Checkpoint Blockade in Cancer Therapy.
870   *J Clin Oncol* **33**, 1974-1982, doi:10.1200/JCO.2014.59.4358 (2015).

871 5   Ribas, A. & Wolchok, J. D. Cancer immunotherapy using checkpoint blockade. *Science* **359**, 1350-
872   1355, doi:10.1126/science.aar4060 (2018).

873 6   Gong, J., Chehrazi-Raffle, A., Reddi, S. & Salgia, R. Development of PD-1 and PD-L1 inhibitors as a
874   form of cancer immunotherapy: a comprehensive review of registration trials and future
875   considerations. *J Immunother Cancer* **6**, 8, doi:10.1186/s40425-018-0316-z (2018).

876 7   Sharpe, A. H. & Pauken, K. E. The diverse functions of the PD1 inhibitory pathway. *Nat Rev
877   Immunol* **18**, 153-167, doi:10.1038/nri.2017.108 (2018).

878 8   Ribas, A. Tumor immunotherapy directed at PD-1. *N Engl J Med* **366**, 2517-2519,
879   doi:10.1056/NEJMe1205943 (2012).

880 9   Ungewickell, A. *et al.* Genomic analysis of mycosis fungoides and Sezary syndrome identifies
881   recurrent alterations in TNFR2. *Nat Genet* **47**, 1056-1060, doi:10.1038/ng.3370 (2015).

882 10   Lesokhin, A. M. *et al.* Nivolumab in Patients With Relapsed or Refractory Hematologic Malignancy:
883   Preliminary Results of a Phase Ib Study. *J Clin Oncol* **34**, 2698-2704, doi:10.1200/JCO.2015.65.9789
884   (2016).

885 11   Kantekure, K. *et al.* Expression patterns of the immunosuppressive proteins PD-1/CD279 and PD-
886   L1/CD274 at different stages of cutaneous T-cell lymphoma/mycosis fungoides. *Am J
887   Dermatopathol* **34**, 126-128, doi:10.1097/DAD.0b013e31821c35cb (2012).

888 12   Querfeld, C. *et al.* Primary T Cells from Cutaneous T-cell Lymphoma Skin Explants Display an
889   Exhausted Immune Checkpoint Profile. *Cancer Immunol Res* **6**, 900-909, doi:10.1158/2326-
890   6066.CIR-17-0270 (2018).

891 13   Khodadoust, M. S. *et al.* Pembrolizumab in Relapsed and Refractory Mycosis Fungoides and Sezary
892   Syndrome: A Multicenter Phase II Study. *J Clin Oncol* **38**, 20-28, doi:10.1200/JCO.19.01056 (2020).

893 14   Wartewig, T. *et al.* PD-1 is a haploinsufficient suppressor of T cell lymphomagenesis. *Nature* **552**,
894   121-125, doi:10.1038/nature24649 (2017).

895 15   Wartewig, T. & Ruland, J. PD-1 Tumor Suppressor Signaling in T Cell Lymphomas. *Trends Immunol*
896   **40**, 403-414, doi:10.1016/j.it.2019.03.005 (2019).

897 16   Gandini, S., Massi, D. & Mandala, M. PD-L1 expression in cancer patients receiving anti PD-1/PD-
898   L1 antibodies: A systematic review and meta-analysis. *Crit Rev Oncol Hematol* **100**, 88-98,
899   doi:10.1016/j.critrevonc.2016.02.001 (2016).

900 17   Johnson, D. B. *et al.* Quantitative Spatial Profiling of PD-1/PD-L1 Interaction and HLA-DR/IDO-1
901   Predicts Improved Outcomes of Anti-PD-1 Therapies in Metastatic Melanoma. *Clin Cancer Res* **24**,
902   5250-5260, doi:10.1158/1078-0432.CCR-18-0309 (2018).

903 18   Jackson, H. W. *et al.* The single-cell pathology landscape of breast cancer. *Nature* **578**, 615-620,
904   doi:10.1038/s41586-019-1876-x (2020).

905 19   Schurch, C. M. *et al.* Coordinated Cellular Neighborhoods Orchestrate Antitumoral Immunity at
906   the Colorectal Cancer Invasive Front. *Cell*, doi:10.1016/j.cell.2020.07.005 (2020).

907 20   Goltsev, Y. *et al.* Deep Profiling of Mouse Splenic Architecture with CODEX Multiplexed Imaging.
908   *Cell* **174**, 968-981 e915, doi:10.1016/j.cell.2018.07.010 (2018).

909 21   Foley, J. W. *et al.* Gene expression profiling of single cells from archival tissue with laser-capture
910   microdissection and Smart-3SEQ. *Genome Res* **29**, 1816-1825, doi:10.1101/gr.234807.118 (2019).

911 22   Newman, A. M. *et al.* Determining cell type abundance and expression from bulk tissues with
912   digital cytometry. *Nat Biotechnol* **37**, 773-782, doi:10.1038/s41587-019-0114-2 (2019).

913 23   Olsen, E. A. *et al.* Clinical end points and response criteria in mycosis fungoides and Sezary
914   syndrome: a consensus statement of the International Society for Cutaneous Lymphomas, the
915   United States Cutaneous Lymphoma Consortium, and the Cutaneous Lymphoma Task Force of
916   the European Organisation for Research and Treatment of Cancer. *J Clin Oncol* **29**, 2598-2607,
917   doi:10.1200/JCO.2010.32.0630 (2011).

918 24   Olsen, E. A. *et al.* Phase IIb multicenter trial of vorinostat in patients with persistent, progressive,
919   or treatment refractory cutaneous T-cell lymphoma. *J Clin Oncol* **25**, 3109-3115,
920   doi:10.1200/JCO.2006.10.2434 (2007).

921 25   de Masson, A. *et al.* High-throughput sequencing of the T cell receptor beta gene identifies
922   aggressive early-stage mycosis fungoides. *Sci Transl Med* **10**, doi:10.1126/scitranslmed.aar5894
923   (2018).

924 26   Pulitzer, M. Cutaneous T-cell Lymphoma. *Clin Lab Med* **37**, 527-546, doi:10.1016/j.cll.2017.06.006
925   (2017).

926 27   Iwahara, K. & Hashimoto, K. T-cell subsets and nuclear contour index of skin-infiltrating T-cells in
927   cutaneous T-cell lymphoma. *Cancer* **54**, 440-446, doi:10.1002/1097-
928   0142(19840801)54:3<440::aid-cncr2820540311>3.0.co;2-m (1984).

929 28   Picchio, M. C. *et al.* CXCL13 is highly produced by Sezary cells and enhances their migratory ability
930   via a synergistic mechanism involving CCL19 and CCL21 chemokines. *Cancer Res* **68**, 7137-7146,
931   doi:10.1158/0008-5472.CAN-08-0602 (2008).

932 29   Campbell, J. J., Clark, R. A., Watanabe, R. & Kupper, T. S. Sezary syndrome and mycosis fungoides
933   arise from distinct T-cell subsets: a biologic rationale for their distinct clinical behaviors. *Blood*
934   **116**, 767-771, doi:10.1182/blood-2009-11-251926 (2010).

935 30   Suga, H. *et al.* The role of IL-32 in cutaneous T-cell lymphoma. *J Invest Dermatol* **134**, 1428-1435,
936   doi:10.1038/jid.2013.488 (2014).

937 31   Qu, K. *et al.* Chromatin Accessibility Landscape of Cutaneous T Cell Lymphoma and Dynamic
938   Response to HDAC Inhibitors. *Cancer Cell* **32**, 27-41.e24, doi:10.1016/j.ccell.2017.05.008 (2017).

939   32   Jariwala, N. *et al.* TIGIT and Helios Are Highly Expressed on CD4(+) T Cells in Sezary Syndrome
940   Patients. *J Invest Dermatol* **137**, 257-260, doi:10.1016/j.jid.2016.08.016 (2017).

941   33   Capriotti, E. *et al.* Expression of T-plastin, FoxP3 and other tumor-associated markers by leukemic
942   T-cells of cutaneous T-cell lymphoma. *Leuk Lymphoma* **49**, 1190-1201,
943   doi:10.1080/10428190802064917 (2008).

944   34   Ascierto, M. L. *et al.* An immunologic portrait of cancer. *J Transl Med* **9**, 146, doi:10.1186/1479-
945   5876-9-146 (2011).

946   35   Galon, J. *et al.* Type, density, and location of immune cells within human colorectal tumors predict
947   clinical outcome. *Science* **313**, 1960-1964, doi:10.1126/science.1129139 (2006).

948   36   Havel, J. J., Chowell, D. & Chan, T. A. The evolving landscape of biomarkers for checkpoint inhibitor
949   immunotherapy. *Nat Rev Cancer* **19**, 133-150, doi:10.1038/s41568-019-0116-x (2019).

950   37   Tumeh, P. C. *et al.* PD-1 blockade induces responses by inhibiting adaptive immune resistance.
951   *Nature* **515**, 568-571, doi:10.1038/nature13954 (2014).

952   38   Binnewies, M. *et al.* Understanding the tumor immune microenvironment (TIME) for effective
953   therapy. *Nat Med* **24**, 541-550, doi:10.1038/s41591-018-0014-x (2018).

954   39   Ayers, M. *et al.* IFN-gamma-related mRNA profile predicts clinical response to PD-1 blockade. *J*
955   *Clin Invest* **127**, 2930-2940, doi:10.1172/JCI91190 (2017).

956   40   Mariathasan, S. *et al.* TGFbeta attenuates tumour response to PD-L1 blockade by contributing to
957   exclusion of T cells. *Nature* **554**, 544-548, doi:10.1038/nature25501 (2018).

958   41   Iglesia, M. D. *et al.* Prognostic B-cell signatures using mRNA-seq in patients with subtype-specific
959   breast and ovarian cancer. *Clin Cancer Res* **20**, 3818-3829, doi:10.1158/1078-0432.CCR-13-3368
960   (2014).

961   42   Schuck, A. M. a. R., Dennis P. in *Community Change: Theories, Practice, and Evidence Promoting*
962   *change through community level interventions* Ch. 2, 61-140 (The Aspen Institute, 2006).

963   43   Sim, G. C. *et al.* IL-2 therapy promotes suppressive ICOS+ Treg expansion in melanoma patients. *J*
964   *Clin Invest* **124**, 99-110, doi:10.1172/JCI46266 (2014).

965   44   Tu, J. F. *et al.* Regulatory T cells, especially ICOS(+) FOXP3(+) regulatory T cells, are increased in
966   the hepatocellular carcinoma microenvironment and predict reduced survival. *Sci Rep* **6**, 35056,
967   doi:10.1038/srep35056 (2016).

968   45   Bagot, M. *et al.* Isolation of tumor-specific cytotoxic CD4+ and CD4+CD8dim+ T-cell clones
969   infiltrating a cutaneous T-cell lymphoma. *Blood* **91**, 4331-4341 (1998).

970   46   Echchakir, H. *et al.* Cutaneous T cell lymphoma reactive CD4+ cytotoxic T lymphocyte clones
971   display a Th1 cytokine profile and use a fas-independent pathway for specific tumor cell lysis. *J*
972   *Invest Dermatol* **115**, 74-80, doi:10.1046/j.1523-1747.2000.00995.x (2000).

973   47   Haabeth, O. A. *et al.* How Do CD4(+) T Cells Detect and Eliminate Tumor Cells That Either Lack or
974   Express MHC Class II Molecules? *Front Immunol* **5**, 174, doi:10.3389/fimmu.2014.00174 (2014).

975   48   Kitano, S. *et al.* Enhancement of tumor-reactive cytotoxic CD4+ T cell responses after ipilimumab
976   treatment in four advanced melanoma patients. *Cancer Immunol Res* **1**, 235-244,
977   doi:10.1158/2326-6066.CIR-13-0068 (2013).

978   49   Marshall, N. B. *et al.* NKG2C/E Marks the Unique Cytotoxic CD4 T Cell Subset, ThCTL, Generated
979   by Influenza Infection. *J Immunol* **198**, 1142-1155, doi:10.4049/jimmunol.1601297 (2017).

980   50   Oh, D. Y. *et al.* Intratumoral CD4(+) T Cells Mediate Anti-tumor Cytotoxicity in Human Bladder
981   Cancer. *Cell*, doi:10.1016/j.cell.2020.05.017 (2020).

982   51   Shin, J. *et al.* Lesional gene expression profiling in cutaneous T-cell lymphoma reveals natural
983   clusters associated with disease outcome. *Blood* **110**, 3015-3027, doi:10.1182/blood-2006-12-
984   061507 (2007).

985   52   Kari, L. *et al.* Classification and prediction of survival in patients with the leukemic phase of
986   cutaneous T cell lymphoma. *J Exp Med* **197**, 1477-1488, doi:10.1084/jem.20021726 (2003).

987   53   Brown, D. C. & Gatter, K. C. Ki67 protein: the immaculate deception? *Histopathology* **40**, 2-11,
988   doi:10.1046/j.1365-2559.2002.01343.x (2002).

989   54   Abel, E. J. *et al.* Analysis and validation of tissue biomarkers for renal cell carcinoma using
990   automated high-throughput evaluation of protein expression. *Hum Pathol* **45**, 1092-1099,
991   doi:10.1016/j.humpath.2014.01.008 (2014).

992   55   Griffin, G. K. *et al.* Spatial Signatures Identify Immune Escape via PD-1 as a Defining Feature of T-
993   cell/Histiocyte-rich Large B-cell Lymphoma. *Blood*, doi:10.1182/blood.2020006464 (2020).

994   56   Campbell, D. J. & Koch, M. A. Phenotypical and functional specialization of FOXP3+ regulatory T
995   cells. *Nat Rev Immunol* **11**, 119-130, doi:10.1038/nri2916 (2011).

996   57   Gobert, M. *et al.* Regulatory T cells recruited through CCL22/CCR4 are selectively activated in
997   lymphoid infiltrates surrounding primary breast tumors and lead to an adverse clinical outcome.
998   *Cancer Res* **69**, 2000-2009, doi:10.1158/0008-5472.CAN-08-2360 (2009).

999   58   Kazanietz, M. G., Durando, M. & Cooke, M. CXCL13 and Its Receptor CXCR5 in Cancer:
1000   Inflammation, Immune Response, and Beyond. *Front Endocrinol (Lausanne)* **10**, 471,
1001   doi:10.3389/fendo.2019.00471 (2019).

1002   59   Gaydosik, A. M. *et al.* Single-Cell Lymphocyte Heterogeneity in Advanced Cutaneous T-cell
1003   Lymphoma Skin Tumors. *Clin Cancer Res* **25**, 4443-4454, doi:10.1158/1078-0432.CCR-19-0148
1004   (2019).

1005   60   Burkle, A. *et al.* Overexpression of the CXCR5 chemokine receptor, and its ligand, CXCL13 in B-cell
1006   chronic lymphocytic leukemia. *Blood* **110**, 3316-3325, doi:10.1182/blood-2007-05-089409 (2007).

1007   61   Lu, S. *et al.* Comparison of Biomarker Modalities for Predicting Response to PD-1/PD-L1
1008   Checkpoint Blockade: A Systematic Review and Meta-analysis. *JAMA Oncol*,
1009   doi:10.1001/jamaoncol.2019.1549 (2019).

1010   62   Giraldo, N. A. *et al.* Multidimensional, quantitative assessment of PD-1/PD-L1 expression in
1011   patients with Merkel cell carcinoma and association with response to pembrolizumab. *J*
1012   *Immunother Cancer* **6**, 99, doi:10.1186/s40425-018-0404-0 (2018).

1013   63   Carey, C. D. *et al.* Topological analysis reveals a PD-L1-associated microenvironmental niche for
1014   Reed-Sternberg cells in Hodgkin lymphoma. *Blood* **130**, 2420-2430, doi:10.1182/blood-2017-03-
1015   770719 (2017).

1016   64   Tang, H., Qiao, J. & Fu, Y. X. Immunotherapy and tumor microenvironment. *Cancer Lett* **370**, 85-
1017   90, doi:10.1016/j.canlet.2015.10.009 (2016).

1018   65   Nagarsheth, N., Wicha, M. S. & Zou, W. Chemokines in the cancer microenvironment and their
1019   relevance in cancer immunotherapy. *Nat Rev Immunol* **17**, 559-572, doi:10.1038/nri.2017.49
1020   (2017).

1021   66   Klein, S. *et al.* PD-1 blockade activates conventional CD4 T cells and the innate immune response
1022   during glioblastoma eradication. *The Journal of Immunology* **200**, 57.59-57.59 (2018).

1023   67   Carstens, J. L. *et al.* Spatial computation of intratumoral T cells correlates with survival of patients
1024   with pancreatic cancer. *Nat Commun* **8**, 15095, doi:10.1038/ncomms15095 (2017).

1025   68   Ribas, A. & Tumeh, P. C. The future of cancer therapy: selecting patients likely to respond to
1026   PD1/L1 blockade. *Clin Cancer Res* **20**, 4982-4984, doi:10.1158/1078-0432.CCR-14-0933 (2014).

1027   69   Gu-Trantien, C. *et al.* CXCL13-producing TFH cells link immune suppression and adaptive memory
1028   in human breast cancer. *JCI Insight* **2**, doi:10.1172/jci.insight.91487 (2017).

1029   70   Bindea, G. *et al.* Spatiotemporal dynamics of intratumoral immune cells reveal the immune
1030   landscape in human cancer. *Immunity* **39**, 782-795, doi:10.1016/j.immuni.2013.10.003 (2013).

1031   71   Ignacio, R. M. C. *et al.* Chemokine Network and Overall Survival in TP53 Wild-Type and Mutant
1032   Ovarian Cancer. *Immune Netw* **18**, e29, doi:10.4110/in.2018.18.e29 (2018).

1033   72   Thommen, D. S. *et al.* A transcriptionally and functionally distinct PD-1(+) CD8(+) T cell pool with
1034   predictive potential in non-small-cell lung cancer treated with PD-1 blockade. *Nat Med* **24**, 994-
1035   1004, doi:10.1038/s41591-018-0057-z (2018).

1036   73   Goswami, S. *et al.* ARID1A mutation plus CXCL13 expression act as combinatorial biomarkers to
1037   predict responses to immune checkpoint therapy in mUCC. *Sci Transl Med* **12**,
1038   doi:10.1126/scitranslmed.abc4220 (2020).

1039   74   Jenkins, R. W. *et al.* Ex Vivo Profiling of PD-1 Blockade Using Organotypic Tumor Spheroids. *Cancer*
1040   *Discov* **8**, 196-215, doi:10.1158/2159-8290.CD-17-0833 (2018).

1041   75   Kamekura, R. *et al.* Circulating PD-1+CXCR5−CD4+ T cells underlying the immunological
1042   mechanisms of IgG4-related disease. *Rheumatology Advances in Practice* **2**,
1043   doi:10.1093/rap/rky043 (2018).

1044   76   Amaria, R. N. *et al.* Neoadjuvant immune checkpoint blockade in high-risk resectable melanoma.
1045   *Nat Med* **24**, 1649-1654, doi:10.1038/s41591-018-0197-1 (2018).

1046 77 Blank, C. U. *et al.* Neoadjuvant versus adjuvant ipilimumab plus nivolumab in macroscopic stage
1047   III melanoma. *Nat Med* **24**, 1655-1661, doi:10.1038/s41591-018-0198-0 (2018).

1048 78 Chalabi, M. *et al.* Neoadjuvant immunotherapy leads to pathological responses in MMR-proficient
1049   and MMR-deficient early-stage colon cancers. *Nat Med* **26**, 566-576, doi:10.1038/s41591-020-
1050   0805-8 (2020).

1051 79 Cloughesy, T. F. *et al.* Neoadjuvant anti-PD-1 immunotherapy promotes a survival benefit with
1052   intratumoral and systemic immune responses in recurrent glioblastoma. *Nat Med* **25**, 477-486,
1053   doi:10.1038/s41591-018-0337-7 (2019).

1054 80 Forde, P. M. *et al.* Neoadjuvant PD-1 Blockade in Resectable Lung Cancer. *N Engl J Med* **378**, 1976-
1055   1986, doi:10.1056/NEJMoa1716078 (2018).

1056 81 Powles, T. *et al.* Clinical efficacy and biomarker analysis of neoadjuvant atezolizumab in operable
1057   urothelial carcinoma in the ABACUS trial. *Nat Med* **25**, 1706-1714, doi:10.1038/s41591-019-0628-
1058   7 (2019).

1059 82 Kim, Y. H. *et al.* Mogamulizumab versus vorinostat in previously treated cutaneous T-cell
1060   lymphoma (MAVORIC): an international, open-label, randomised, controlled phase 3 trial. *Lancet
1061   Oncol* **19**, 1192-1204, doi:10.1016/S1470-2045(18)30379-6 (2018).

1062 83 Kamijo, H. *et al.* BET bromodomain inhibitor JQ1 decreases CD30 and CCR4 expression and
1063   proliferation of cutaneous T-cell lymphoma cell lines. *Arch Dermatol Res* **309**, 491-497,
1064   doi:10.1007/s00403-017-1749-9 (2017).

1065 84 Basu, A., Yearley, J. H., Annamalai, L., Pryzbycin, C. & Rini, B. Association of PD-L1, PD-L2, and
1066   Immune Response Markers in Matched Renal Clear Cell Carcinoma Primary and Metastatic Tissue
1067   Specimens. *Am J Clin Pathol* **151**, 217-225, doi:10.1093/ajcp/aqy141 (2019).

1068 85 Seo, Y. D. *et al.* Mobilization of CD8(+) T Cells via CXCR4 Blockade Facilitates PD-1 Checkpoint
1069   Therapy in Human Pancreatic Cancer. *Clin Cancer Res* **25**, 3934-3945, doi:10.1158/1078-
1070   0432.CCR-19-0081 (2019).

1071 86 Goksuluk, D., Korkmaz, S., Zararsiz, G. & Karaagaoglu, A. E. easyROC: an interactive web-tool for
1072   ROC curve analysis using R language environment. *The R Journal* **8**, 213-226 (2016).

1073 87 Samusik, N., Good, Z., Spitzer, M. H., Davis, K. L. & Nolan, G. P. Automated mapping of phenotype
1074   space with single-cell data. *Nat Methods* **13**, 493-496, doi:10.1038/nmeth.3863 (2016).

1075 88 Quail, M. A. *et al.* A large genome center's improvements to the Illumina sequencing system. *Nat
1076   Methods* **5**, 1005-1010, doi:10.1038/nmeth.1270 (2008).

1077 89 Bates, D., Mächler, M., Bolker, B. & Walker, S. Fitting Linear Mixed-Effects Models Using lme4.
1078   *2015* **67**, 48, doi:10.18637/jss.v067.i01 (2015).

1079 90 Kuznetsova, A., Brockhoff, P. B. & Christensen, R. H. B. lmerTest Package: Tests in Linear Mixed
1080   Effects Models. *2017* **82**, 26, doi:10.18637/jss.v082.i13 (2017).

1081 91 Stuart, T. *et al.* Comprehensive Integration of Single-Cell Data. *Cell* **177**, 1888-1902 e1821,
1082   doi:10.1016/j.cell.2019.05.031 (2019).

1083   92   Blondel, V. D., Guillaume, J.-L., Lambiotte, R. & Lefebvre, E. Fast unfolding of communities in large
1084   networks. *Journal of Statistical Mechanics: Theory and Experiment* **2008**, P10008,
1085   doi:10.1088/1742-5468/2008/10/p10008 (2008).

1086   93   McInnes, L., Healy, J. & Melville, J. Umap: Uniform manifold approximation and projection for
1087   dimension reduction. *arXiv preprint arXiv:1802.03426* (2018).

1088   94   Wickham, H. *ggplot2: elegant graphics for data analysis*. (Springer, 2016).

1089   95   Slowikowski, K. ggrepel: Repulsive text and label geoms for 'ggplot2'. *R package version 0.6* **5**
1090   (2016).

1091

1092

1093
1094
1095
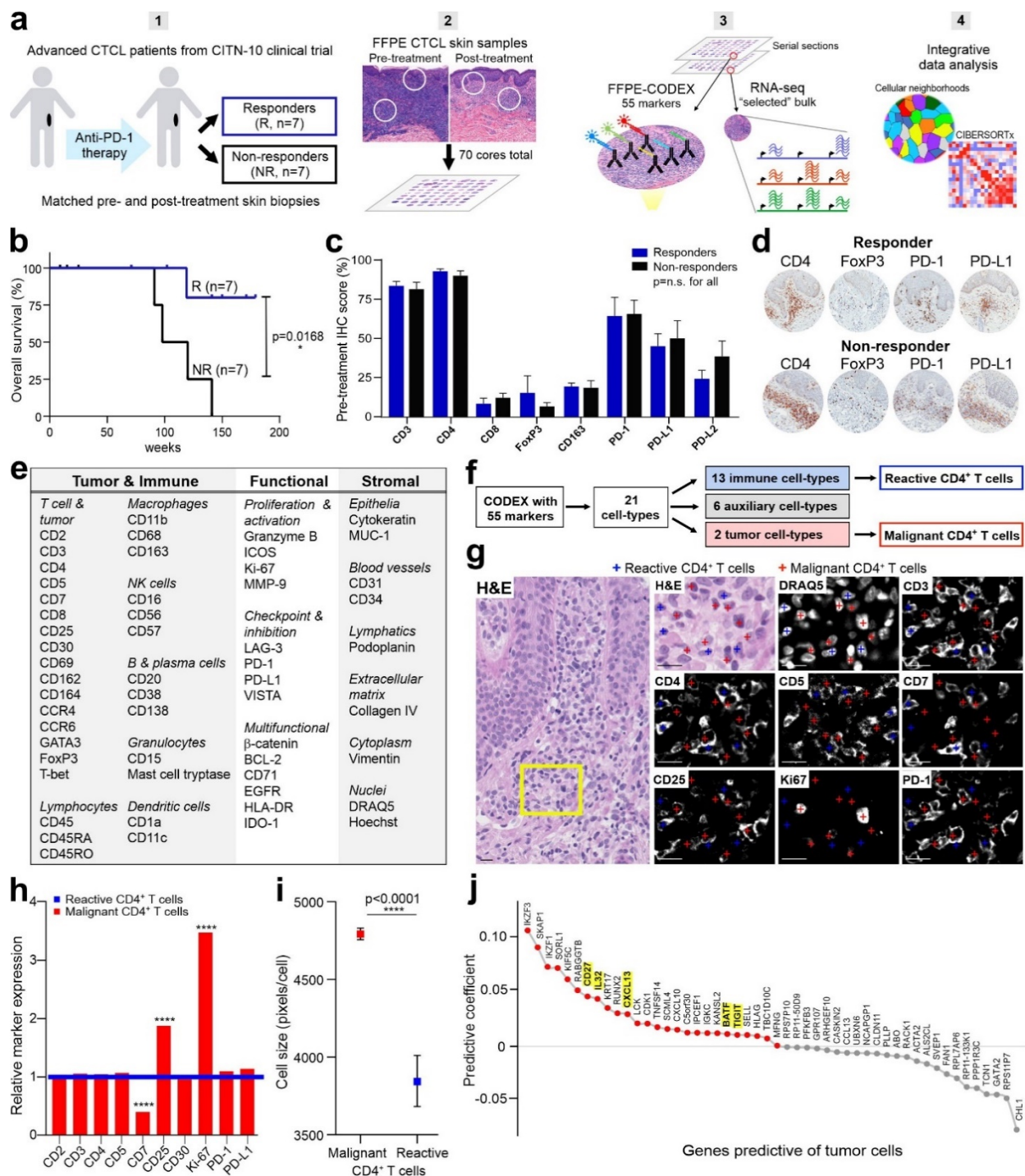
1096

Fig 1. Discrimination of malignant and reactive CD4$^+$ T cells in the CTCL TME. a, Workflow for sample

preparation, CODEX, RNAseq, and computational analyses. **b**, Kaplan-Meier overall survival curve,

comparing responders (R, *n*=7, blue line) and non-responders (NR, *n*=7, black line) (hazard ratio 0.0969

responder/non-responder; *p* value calculated by log-rank test). **c**, IHC protein marker expression in

responders and non-responders pre-treatment (mean ± s.e.m.). *P* values were calculated by two-sided

1102   Wilcoxon's rank-sum tests (p = not significant (n.s.) for all comparisons). **d**, Representative pre-

1103   treatment IHC images for select markers from a responder (top) and non-responder (bottom). **e**, CODEX

1104   antibody panel (see also **Sup. Fig. 1d**). **f**, Identification of 21 cell-types by clustering (see also **Sup. Fig.**

1105   **2a-b**). **g**, Visual verification of reactive (blue crosses) versus malignant (red crosses) CD4$^+$ T cells in CTCL

1106   tissue. Scale bars, 20 μm. **h**, Average expression of select markers on malignant (red bars) relative to

1107   reactive (blue line) CD4$^+$ T cells. P values were calculated by two-sided Wilcoxon's rank-sum tests (****,

1108 $p<0.0001$). **i**, Cell size, measured in pixels/cell, of all malignant (red square) versus reactive (blue square)

1109   CD4$^+$ T cells (mean ± s.e.m.). P value was calculated by a two-sided Wilcoxon's rank-sum test. **j**, Ranking

1110   genes most predictive of tumor cells per tissue microarray spot using an L1-regularized linear model.

1111   Red colored genes have positive predictive coefficients (i.e., most likely to represent tumor cells); gray

1112   colored genes have negative predictive coefficients (i.e., less likely to represent tumor cells). Known

1113   CTCL marker genes are highlighted in yellow.

1114

1115
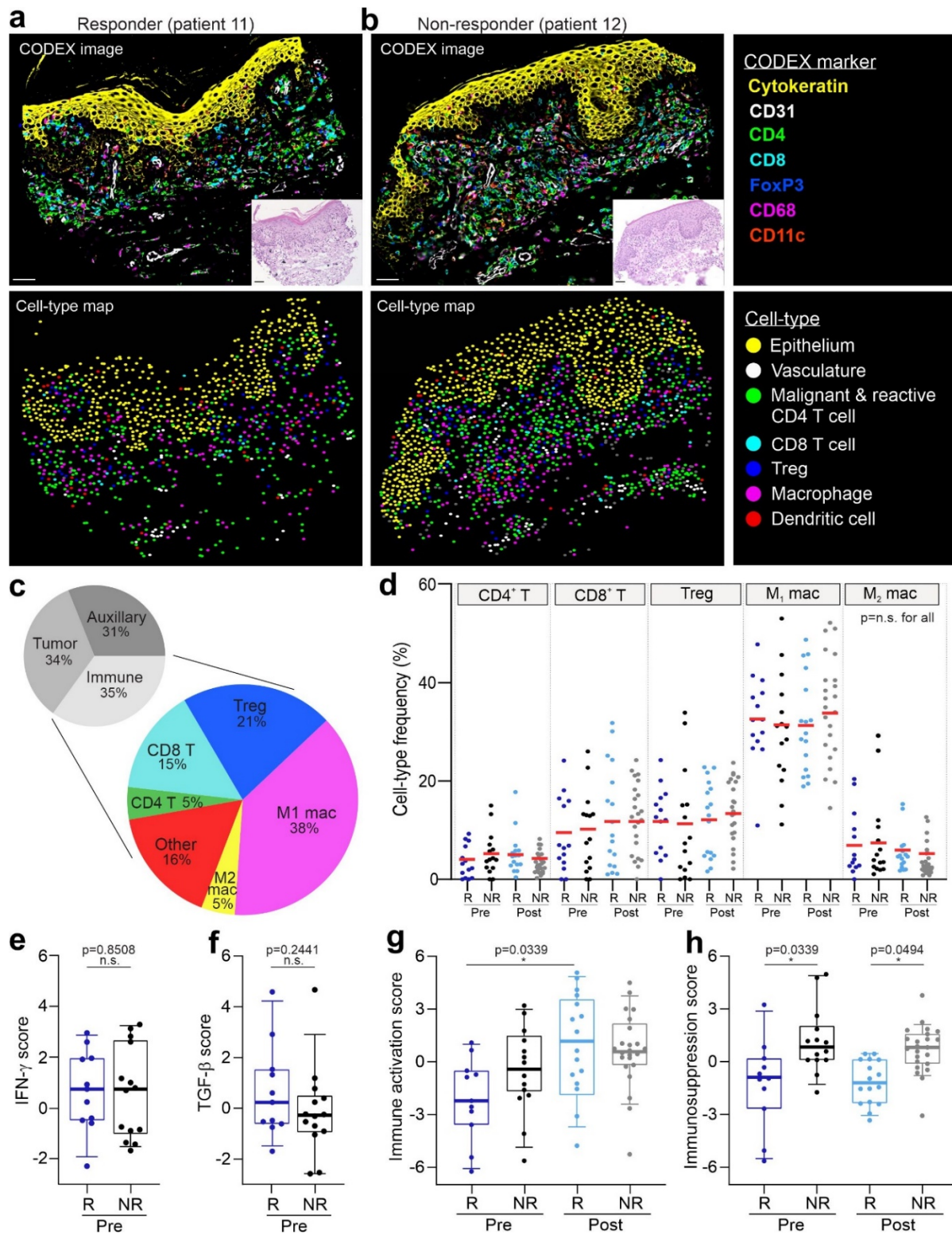
Fig 2. Characterization of the CTCL TME pre- and post-pembrolizumab treatment. a-b, Top panels:

Representative CODEX seven-color overlay images from a responder (left) and non-responder (right)

pre-treatment. Scale bar, 50 μm. Insets, corresponding H&E images; scale bars, 50 μm. Bottom panels:

1120   corresponding cell-type maps. **c**, Upper pie chart: overall frequencies of tumor, immune and auxiliary

1121   cell-types. Lower pie chart: overall frequencies of all immune cell-types, including CD4^{+} T cells, CD8^{+} T

1122   cells, Tregs, M1 macrophages, M2 macrophages, and other (B cells, dendritic cells, Langerhans cells,

1123   mast cells, neutrophils, and plasma cells). **d**, Cell-type frequencies of CD4^{+} T cell, CD8^{+} T cell, Treg, M1

1124   macrophage, and M2 macrophage as a percentage of all immune cells per tissue microarray spot in

1125   responders and non-responders pre- and post-treatment (mean, red bar). *P* values were calculated with

1126   a linear mixed-effect model with Bonferroni's corrections for multiple comparisons (p = not significant

1127   (n.s.) for all comparisons). **e-f**, IFN-γ (**e**) and TGF-β (**f**) gene scores between responders and non-

1128   responders pre-treatment per spot. Boxes, median ± interquartile range (IQR); whiskers, 1.5x IQR. *P*

1129   values were calculated with a linear mixed-effect model with Bonferroni's corrections for multiple

1130   comparisons. **g-h**, Immune activation (**g**) and immunosuppression (**h**) gene scores, computed on bulk

1131   RNA-seq data, between responders and non-responders pre- and post-treatment per spot. Boxes,

1132   median ± IQR; whiskers, 1.5x IQR. *P* values were calculated with a linear mixed-effect model with

1133   Bonferroni's corrections for multiple comparisons.

1134
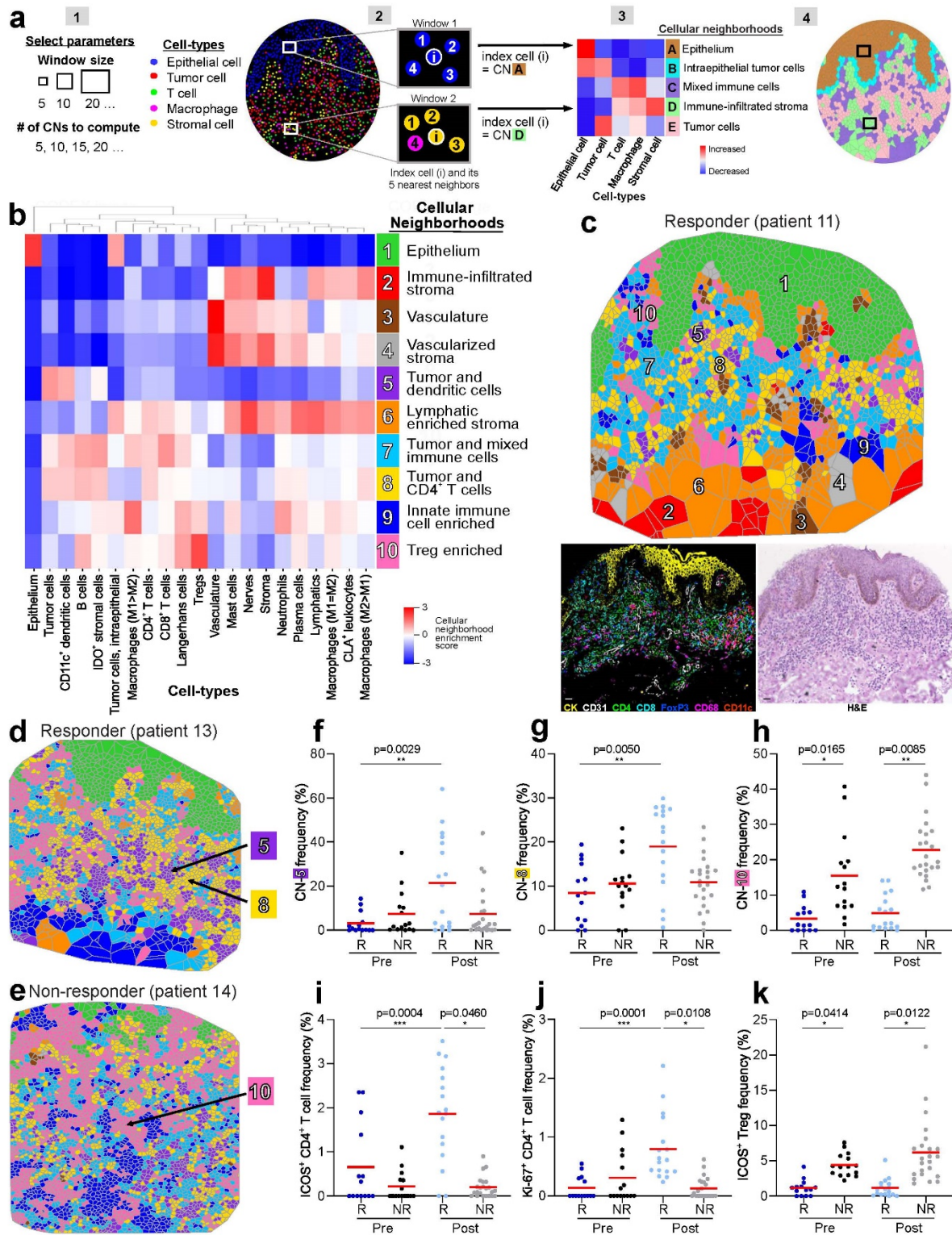
Fig 3. Cellular neighborhoods reveal differences in the spatial TME organization in responders and non-responders. a, Cellular neighborhood (CN) analysis schematic. [1] Selection of computational parameters, including the window size (five in this schematic) and the number of CNs to be computed

1139   (five in this schematic). [2] Assignment of an index cell (i, center of window) to a given CN based on the

1140   composition of cell-types within its corresponding window the clustering of windows. [3] Heatmap of

1141   cell-type distribution for each CN and assignment of CN names. [4] Visualization of CNs as a Voronoi

1142   diagram. **b**, Identification of 10 conserved CNs in the CTCL TME using a window size of 10. **c**,

1143   Representative Voronoi diagram of the 10 CNs in a responder post-treatment, with the corresponding

1144   H&E and seven color fluorescent CODEX images. Scale bar, 20 μm. **d-e**, Voronoi diagrams of CNs in a

1145   responder (**d**) and non-responder (**e**) post-treatment, highlighting CN-5 (tumor and dendritic cells), CN-8

1146   (tumor and CD4$^+$ T cells) and CN-10 (Treg enriched). **f-h**, Frequencies of CN-5 (**f**), CN-8 (**g**) and CN-10 (**h**)

1147   per tissue microarray spot in responders and non-responders pre- and post-treatment (mean, red bar). *P*

1148   values were calculated with a linear mixed-effect model with Bonferroni's corrections for multiple

1149   comparisons. **i-k**, Frequencies of ICOS$^+$ CD4$^+$ T cell (**i**), Ki-67$^+$ CD4$^+$ T cell (**j**) and ICOS$^+$ Treg (**k**) as a

1150   percentage of all immune cells per spot in responders and non-responders pre- and post-treatment

1151   (mean, red bar). *P* values were calculated with a linear mixed-effect model with Bonferroni's corrections
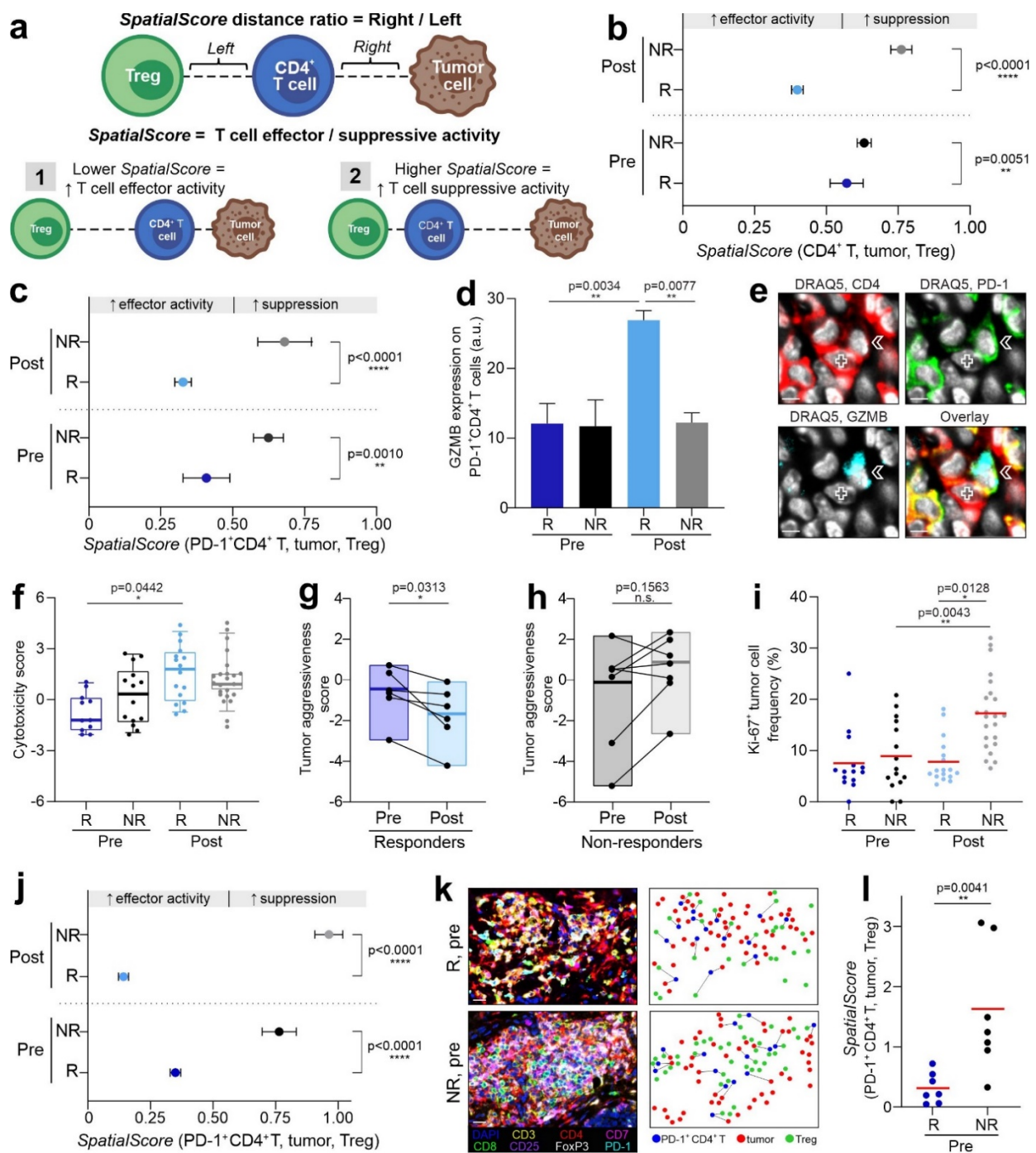
1152   for multiple comparisons.

1153

1154

1155

1156

1157

1158

Fig 4. Spatial relationship between CD4+ T cells, Tregs and tumor cells predicts pembrolizumab response in CTCL. a, *SpatialScore* schematic.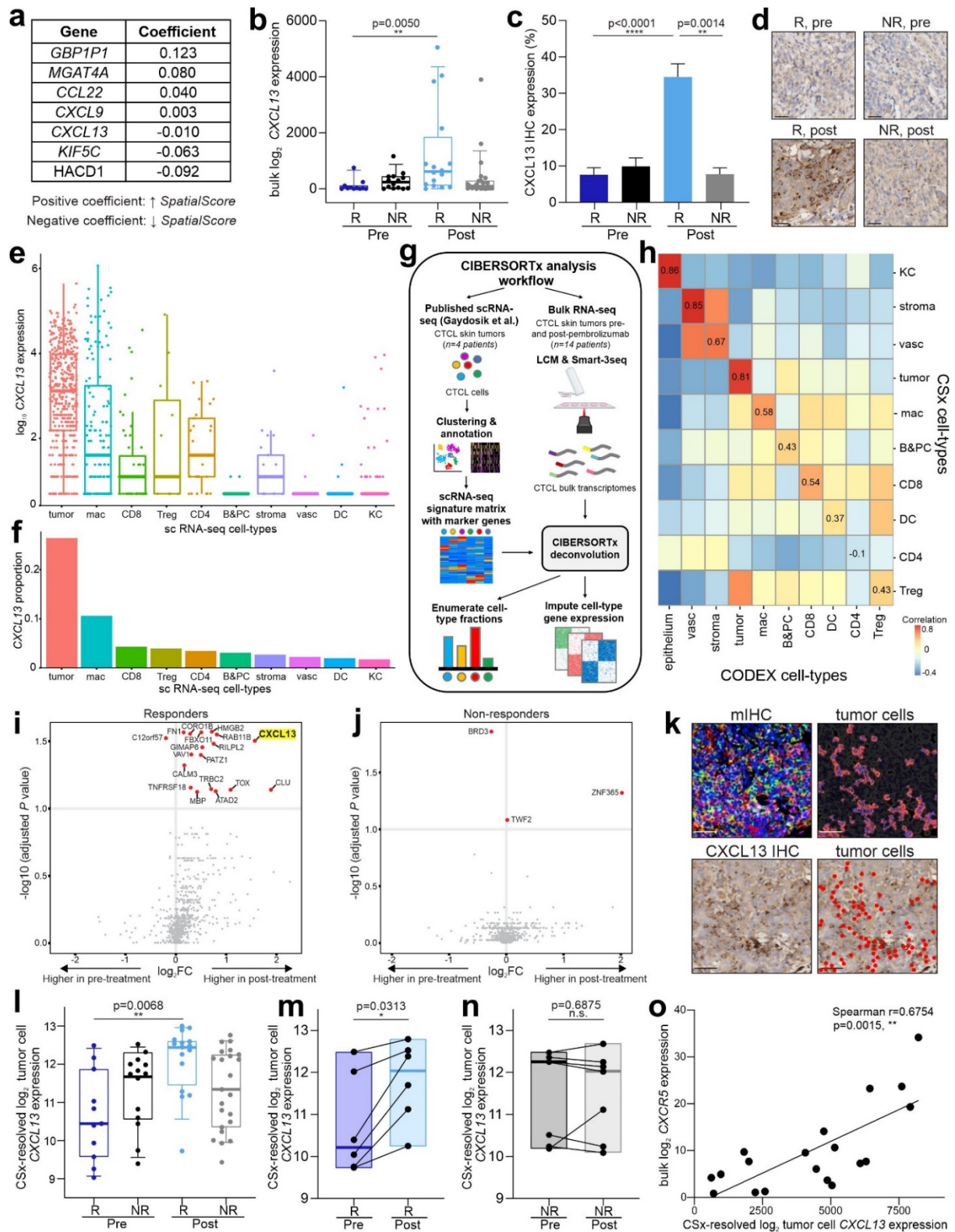 The *SpatialScore* is calculated by taking the ratio of the physical distance between each CD4+ T cell and its nearest tumor cell (distance "right") relative to its nearest Treg (distance "left"). [1] A lower *SpatialScore* (i.e., CD4+ T cells are closer to tumor cells than Tregs) suggests increased T cell effector activity. [2] A higher spatial score (i.e., CD4+ T cells are closer to

1165   Tregs than tumor cells) suggests increased T cell suppression. **b-c**, *SpatialScore* on a per cell basis for

1166   CD4$^+$ T cells (**b**) and PD-1$^+$ CD4$^+$ T cells (**c**) for each patient group (mean ± s.e.m.). *P* values were

1167   calculated by two-sided Wilcoxon's rank-sum tests, with no adjustments for multiple comparisons. **d**,

1168   GZMB protein expression on PD-1$^+$ CD4$^+$ T cells by CODEX in responders and non-responders pre- and

1169   post-treatment per tissue microarray spot (mean fluorescence intensity (arbitrary units, a.u.) ± s.e.m.) *P*

1170   values were calculated with a linear mixed-effect model with Bonferroni's corrections for multiple

1171   comparisons. **e**, CODEX images of DRAQ5 (white), CD4 (red), PD-1 (green), GZMB (cyan), and overlay

1172   showing contact between a tumor cell (marked by cross) and GZMB-expressing PD-1$^+$ CD4$^+$ T cell

1173   (marked by arrow) in responder patient 13 post-treatment. Scale bars, 10 µm. **f**, Cytotoxicity gene

1174   scores, computed on bulk RNA-seq data, between responders and non-responders pre- and post-

1175   treatment per spot. Boxes, median ± IQR; whiskers, 1.5x IQR. *P* values were calculated with a linear

1176   mixed-effect model with Bonferroni's corrections for multiple comparisons. **g-h**, Pre- to post-treatment

1177   changes in tumor aggressiveness gene scores, computed on bulk RNA-seq data, on a per patient basis in

1178   responders (**g**) and non-responders (**h**). Boxes, median ± IQR; whiskers, 1.5x IQR. *P* values were

1179   calculated by two-sided Wilcoxon's signed-rank tests. **i**, Ki-67$^+$ tumor cell frequencies per spot in

1180   responders and non-responders pre- and post-treatment (mean, red bar). *P* values were calculated with

1181   a linear mixed-effect model with Bonferroni's corrections for multiple comparisons. **j**, *SpatialScore* on a

1182   per cell basis calculated from Vectra mIHC data using PD-1$^+$CD4$^+$ T cells for each patient group (mean ±

1183   s.e.m.). *P* values were calculated by two-sided Wilcoxon's rank-sum tests, with no adjustments for

1184   multiple comparisons. **k**, Vectra mIHC images (left panels; representative regions of a tissue microarray

1185   spot) in responder patient 13 (R) and non-responder patient 14 (NR) pre-treatment. Scale bars, 20 µm.

1186   The corresponding spatial plots (right panels) show that PD-1$^+$ CD4$^+$ T cells (blue dots) are closer to

1187   tumor cells (red dots) than Tregs (green dots) in the responder and vice versa in the non-responder. **l**,

1188   Pre-treatment *SpatialScore* calculated from Vectra mIHC data for responders and non-responders on a

1189   per patient basis (mean, red bar). *P* values was calculated by a two-sided Wilcoxon's rank-sum test.

a

Gene	Coefficient
GBP1P1	0.123
MGAT4A	0.080
CCL22	0.040
CXCL9	0.003
CXCL13	-0.010
KIF5C	-0.063
HACD1	-0.092

Positive coefficient: ↑ *SpatialScore*
Negative coefficient: ↓ *SpatialScore*

1190

Fig 5. CXCL13 is a key driver of pembrolizumab response in CTCL. a, Seven genes predictive of the

SpatialScore identified from bulk RNA-seq data. Genes with a positive coefficient are associated with a

51

1193 higher *SpatialScore* (i.e., a suppressive phenotype), whereas those with a negative coefficient are

1194 associated with a lower *SpatialScore* (i.e., an effector phenotype). **b**, Normalized bulk *CXCL13* gene

1195 expression between responders and non-responders pre- and post-treatment per tissue microarray

1196 spot. Boxes, median ± IQR; whiskers, 1.5x IQR. *P* values were calculated with a linear mixed-effect

1197 model with Bonferroni's corrections for multiple comparisons. **c**, CXCL13 protein expression by IHC in

1198 responders and non-responders pre- and post-treatment per spot (mean ± s.e.m.). *P* values were

1199 calculated with a linear mixed-effect model with Bonferroni's corrections for multiple comparisons. **d**,

1200 Representative CXCL13 IHC images from responder patient 9 pre-treatment (top left) and post-

1201 treatment (bottom left) as well as non-responder patient 14 pre-treatment (top right) and post-

1202 treatment (bottom right). Scale bars, 20 μm. **e-f**, Single-cell transcriptomes from a publicly available

1203 scRNA-seq dataset of CTCL skin tumors (Gaydosik et al.)[59] were analyzed for *CXCL13* expression.

1204 Abbreviations: mac (macrophages), B&PC (B and plasma cells), vasc (vasculature), DC (dendritic cells),

1205 and KC (keratinocytes). **e**, Normalized expression of *CXCL13* in single cells (each dot represents a cell

1206 positive for *CXCL13*). Cells with *CXCL13* log1p normalized read counts less than 0.5 were excluded (see

1207 **Methods**). Boxes, median ± IQR; whiskers, 1.5x IQR. **f**, Proportion of CXCL13-expressing cells per cell-

1208 type. **g**, CIBERSORTx analysis workflow schematic. Single cell transcriptomes from Gaydosik et al.[59] were

1209 used to generate a CSx deconvolution signature matrix, consisting of cell-type-specific marker genes (left

1210 portion of schematic). This matrix was then applied to CTCL bulk transcriptomes obtained with laser-

1211 capture microdissection (LCM) and Smart-3Seq (right portion of schematic) to enumerate cell-type

1212 fractions and resolve gene expression profiles (see **Methods**). **h,** Heatmap of the correlation between

1213 CSx-resolved cell-type frequencies and CODEX-identified cell-type frequencies. Spearman correlation

1214 coefficients between corresponding cell-types are shown along the diagonal. For this analysis, some of

1215 the original 21 CODEX cell-types were manually merged to match CSx cell-types (e.g., B cells and plasma

1216 cells). **i-j**, Volcano plots of differential gene expression of CSx-resolved tumor cell genes in responders (**j**)

1217 and non-responders (**k**) pre- and post-treatment. *P* values were calculated with a linear mixed-effect

1218   model with Benjamini-Hochberg correction. Significantly different genes ($p < 0.1$) are colored red;

1219   *CXCL13* is highlighted yellow. **k**, Vectra mIHC image of DAPI (blue), CD3 (yellow), CD4 (red), CD7

1220   (magenta), CD8 (green), CD25 (purple), FoxP3 (white), and PD-1 (cyan) (top left), corresponding tumor

1221   cell depiction (top right), corresponding CXCL13 IHC image (bottom left), and overlaid image showing

1222   that CXCL13 IHC staining most commonly localized to tumor cells (red circles) (bottom right) in

1223   responder patient 9 post-treatment. Scale bars, 20 µm. **l**, Normalized CSx-resolved *CXCL13* expression in

1224   tumor cells between responders and non-responders pre- and post-treatment per spot. Boxes, median ±

1225   IQR; whiskers, 1.5x IQR. *P* values were calculated with a linear mixed-effect model with Bonferroni's

1226   corrections for multiple comparisons. **m-n**, Pre- to post-treatment changes in normalized *CXCL13* gene

1227   expression from CSx-resolved tumor genes on a per patient basis in responders (**m**) and non-responders

1228   (**n**). Boxes, median ± IQR; whiskers, 1.5x IQR. *P* values were calculated by two-sided Wilcoxon's signed-

1229   rank tests. **o**, Correlation of CSx-resolved tumor cell *CXCL13* expression and bulk *CXCR5* expression per

1230   spot. Data was evaluated with the Spearman test and a two-tailed t-distribution with n-2 degrees of
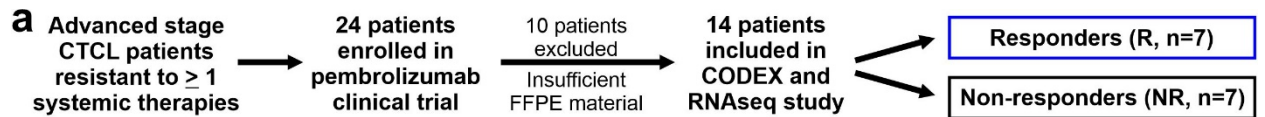
1231   freedom.

1232

1233
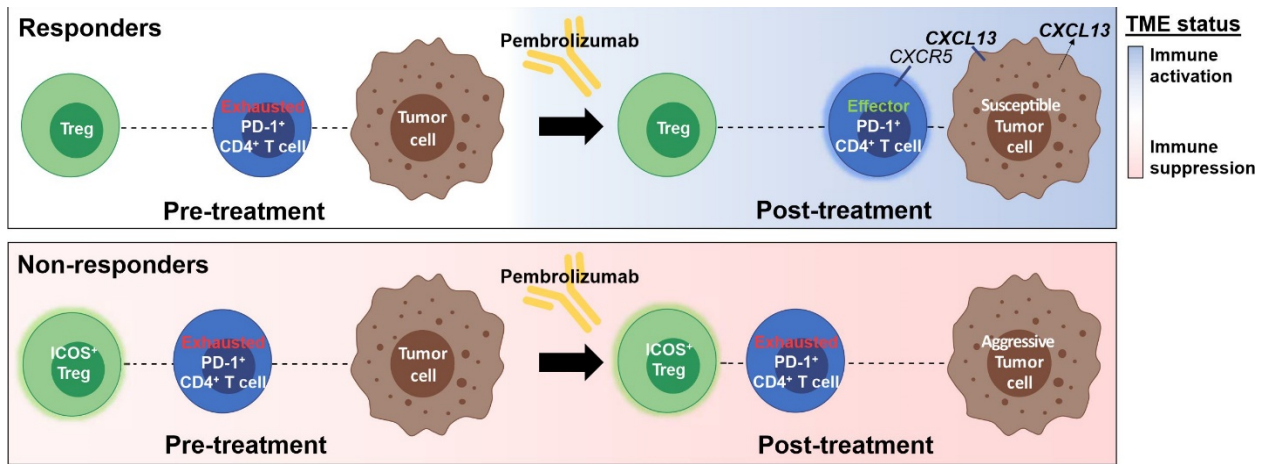
1234

1235

1236 **Fig 6. Proposed mechanisms of pembrolizumab response in CTCL.**

1237 Proposed mechanisms of pembrolizumab response in therapy responders (top panel) and non-

1238 responders (bottom panel) pre- and post-treatment. The functional immune status of the TME is

1239 represented by blue shading when activated and pink shading when suppressed. In non-responders, the

1240 TME is continually immunosuppressed and persistently exhausted PD-1$^+$CD4$^+$ T cells are in closer

1241 proximity to potently suppressive ICOS$^+$ Tregs. Due to pembrolizumab resistance, non-responder tumor

1242 cells become more aggressive following therapy. In contrast, responders have a neutral functional

1243 immune state pre-treatment, which becomes activated following pembrolizumab therapy, enabling the

1244 transition from exhausted to effector PD-1$^+$ CD4$^+$ T cells. Additionally, responder tumor cells are

1245 susceptible to PD-1 blockade and overexpress CXCL13. This attracts effector PD-1$^+$ CD4$^+$ T cells toward

1246 tumor cells, providing a mechanism for the sustained clinical response seen in responders.

1247

1248

a Advanced stage CTCL patients resistant to ≥ 1 systemic therapies → 24 patients enrolled in pembrolizumab clinical trial → 10 patients excluded (Insufficient FFPE material) → 14 patients included in CODEX and RNAseq study → Responders (R, n=7) / Non-responders (NR, n=7)

b

Patient characteristics	Responders	Non-responders
Patients (n)	7	7
Male (n)	5	5
Female (n)	2	2
Age, year (mean ± SD)	67.5 ± 12.0	62.1 ± 14.4
Cancer type (n)		
Mycosis fungoides (MF)	4	3
Sézary syndrome (SS)	3	4
Cancer stage (TNM) (n)		
IB	0	1
IIB	1	0
IIIA	2	0
IIIB	1	2
IVA	3	4
Prior systemic therapies		
Number (mean ± SD)	4 ± 2	4 ± 3
Range	1 - 6	1 - 9
Patient outcomes		
mSWAT change (**)	41.5	-90.5
1 year PFS (*)	85.7%	28.6%
Patient deaths (n) (*)	1	4
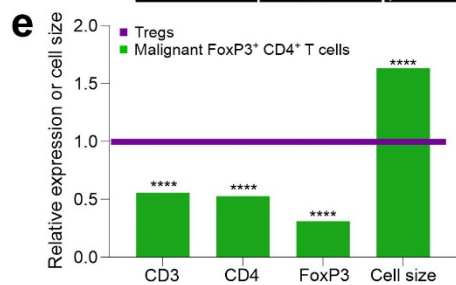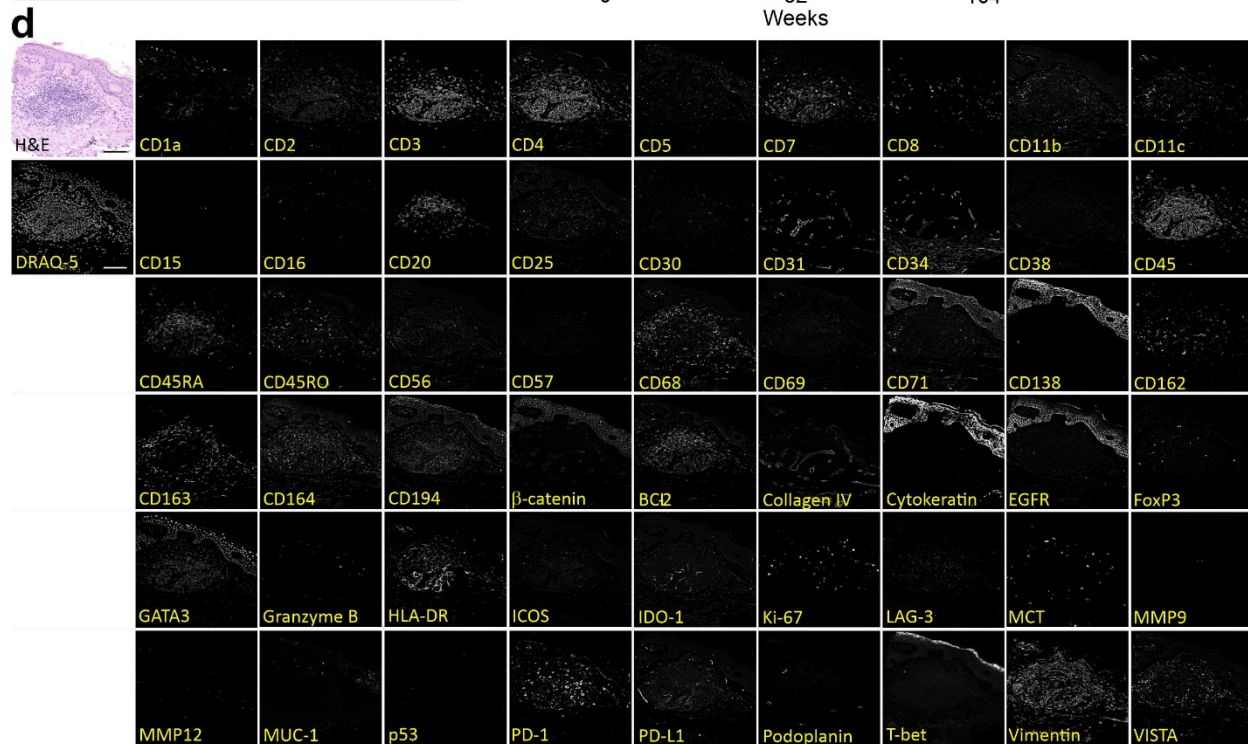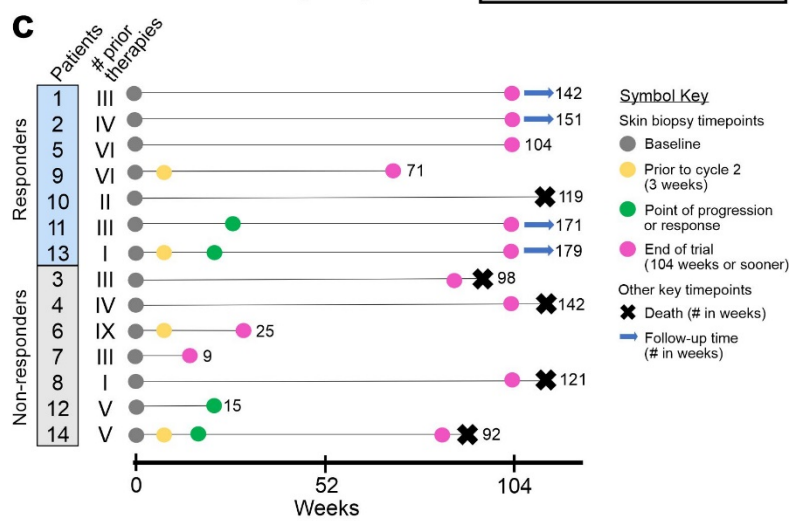
**Sup. Fig. 1. Study design and CODEX experimental validation. a**, Framework for the 14 included CTCL

patient samples used for CODEX tissue imaging, RNA-seq and mIHC imaging. **b**, Patient characteristics

1252   for the 7 responders and 7 non-responders. Significant differences between responders and non-

1253   responders were only noted for patient outcomes: the change from baseline in skin by the modified

1254   Severity Weighted Assessment Tool (mSWAT) (**, p=0.0019 by Wilcoxon's rank sum test), the 1 year

1255   progression free survival (PFS) (*, p=0.0306 by Wilcoxon's rank sum test), and patients deaths (*,

1256 p=0.0168 by log rank test in Kaplan-Meier overall survival curve; see **Fig. 1b**). **c**, Swimmer plot of

1257   individual patients, depicting treatment history and timepoints in weeks for every tumor biopsy used in

1258   this study. Lines represent overall survival in weeks. A rightward arrow indicates that the patient was

1259   still alive following the final tumor collection. A rightward X indicates that the patient died. **d**, Validation

1260   of the 55-marker CODEX antibody panel used to stain the CTCL skin tissue microarray. Images of a single

1261   microarray spot are depicted in false gray color for each marker. H&E staining is also shown. Scale bars,

1262   100 μm. **e**, Average expression of CD3, CD4, FoxP3 and cell size, measured in pixels/cell (green bars),

1263   relative to Tregs (purple line). P values were calculated by two-sided Wilcoxon's rank-sum tests (****,

1264 p<0.0001).

1265

1266
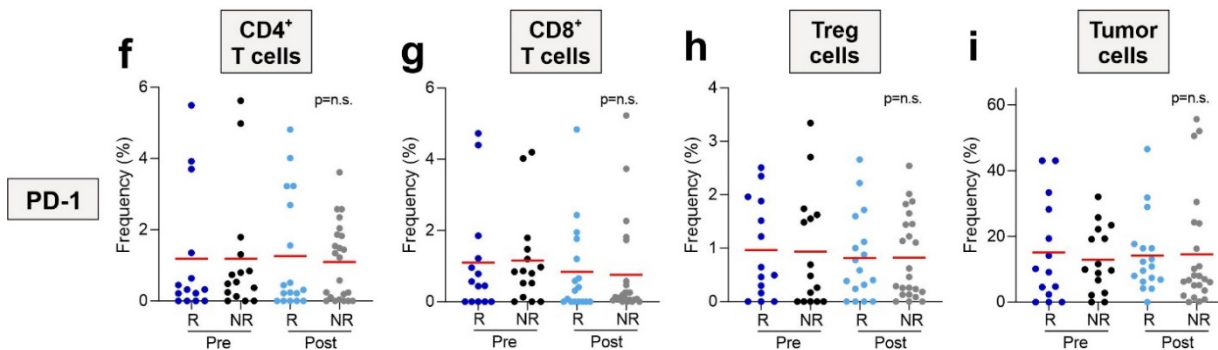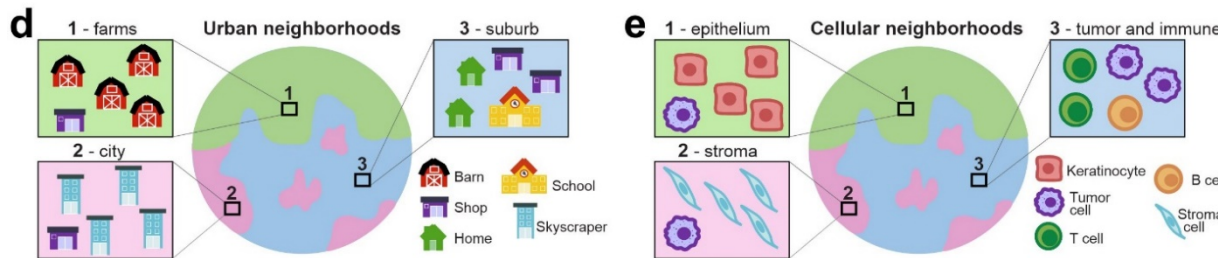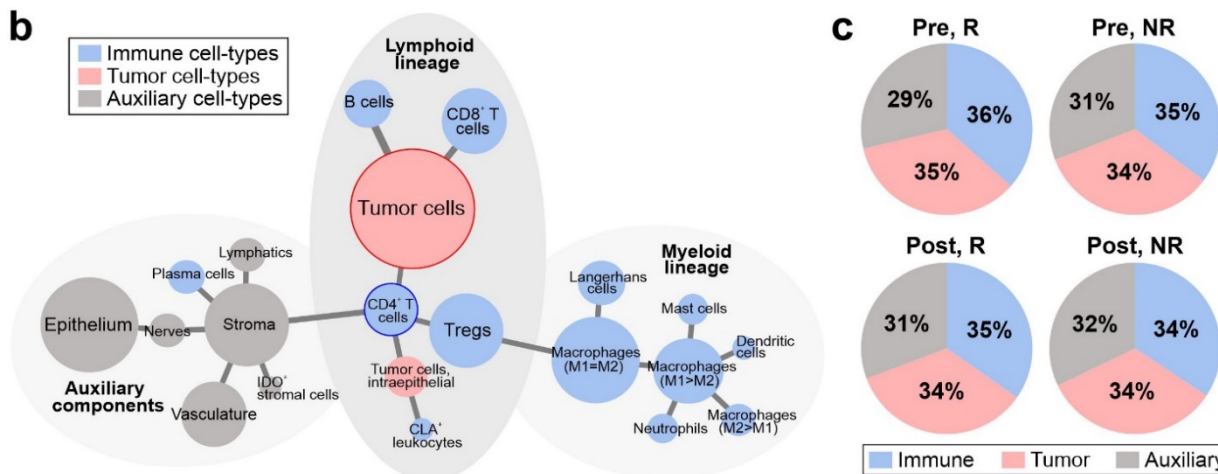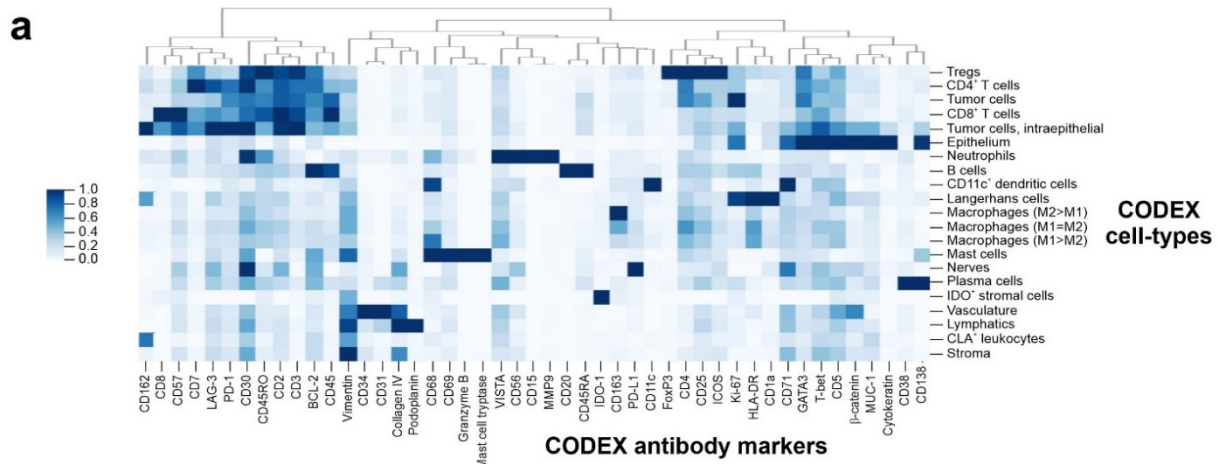
**Sup. Fig. 2. Characterizing CODEX cell-types, the cellular neighborhood concept, and PD-1 positivity. a,**

Heatmap of CODEX antibody marker expression in each of the 21 identified cell-types. **b,** Minimal

1270   spanning tree of the 21 cell-types, which are colored blue (immune cell-types), red (tumor cell-types)

1271   and gray (auxiliary cell-types). **c**, Frequencies of tumor, immune and auxiliary cell-types for each patient

1272   group (p=n.s. for all comparisons). **d-e**, Conceptual neighborhood schematic showing how urban

1273   neighborhoods are determined based on their composition of buildings (**d**) and cellular neighborhoods

1274   based on cell-types (**e**). **f-i**, Frequencies of PD-1$^+$ CD4$^+$ T cells (**f**), PD-1$^+$ CD8$^+$ T cells (**g**), PD-1$^+$ Tregs (**h**),

1275   and , PD-1$^+$ tumor cells (**i**) per tissue microarray spot in responders and non-responders pre- and post-

1276   treatment (mean, red bar). *P* values were calculated with a linear mixed-effect model with Bonferroni's

1277   corrections for multiple comparisons.

1278

1279
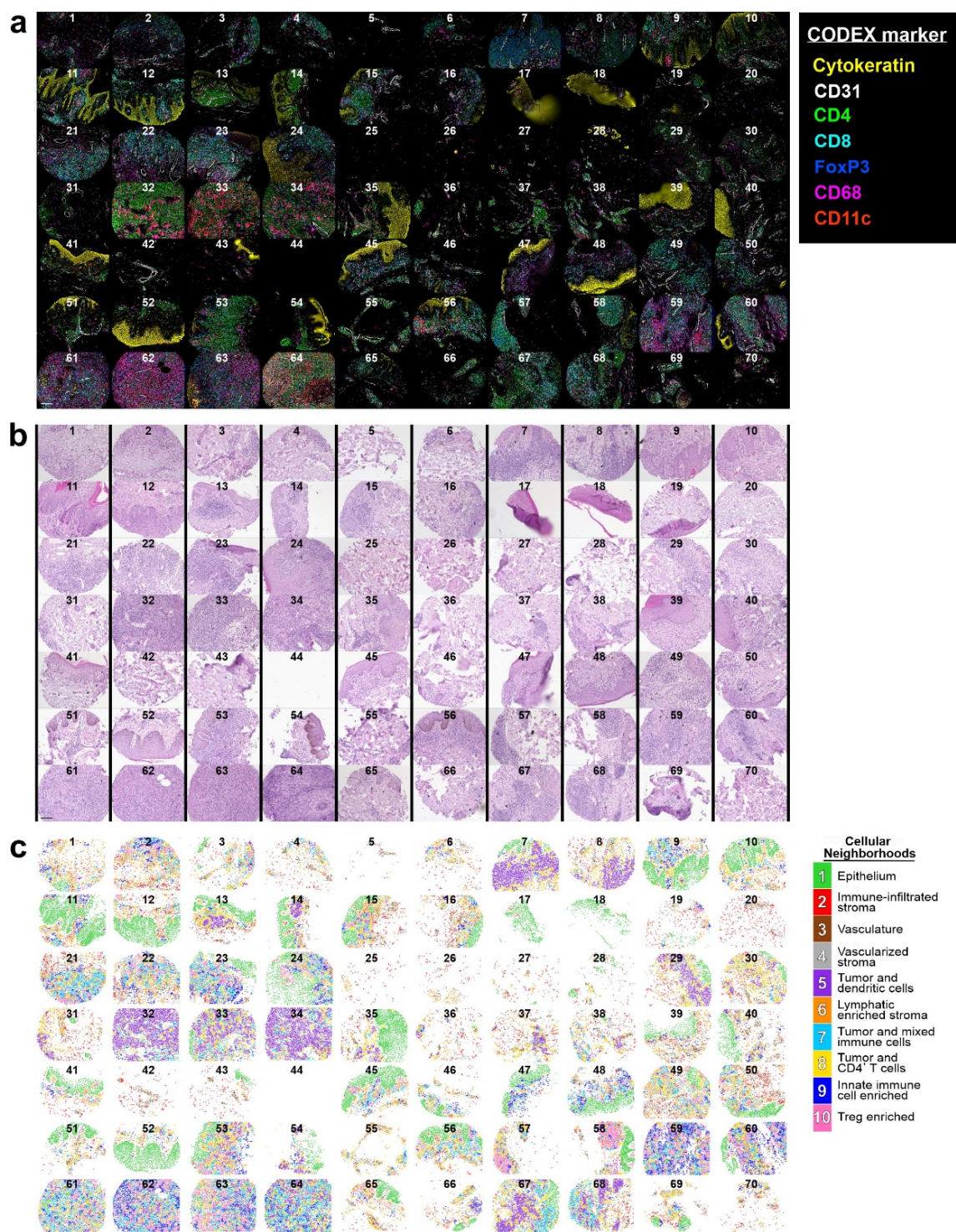
1280

Sup. Fig. 3. CODEX, H&E, and cellular neighborhood images for the CTCL tissue microarray. a, CODEX

seven-color overlay image of the CTCL tissue microarray. Scale bar, 100 μm. **b**, Corresponding H&E

image of the CTCL tissue microarray. Scale bar, 100 μm. **c**, Dot plot Voronoi diagram of the 10 identified

CNs, colored according to the corresponding legend.
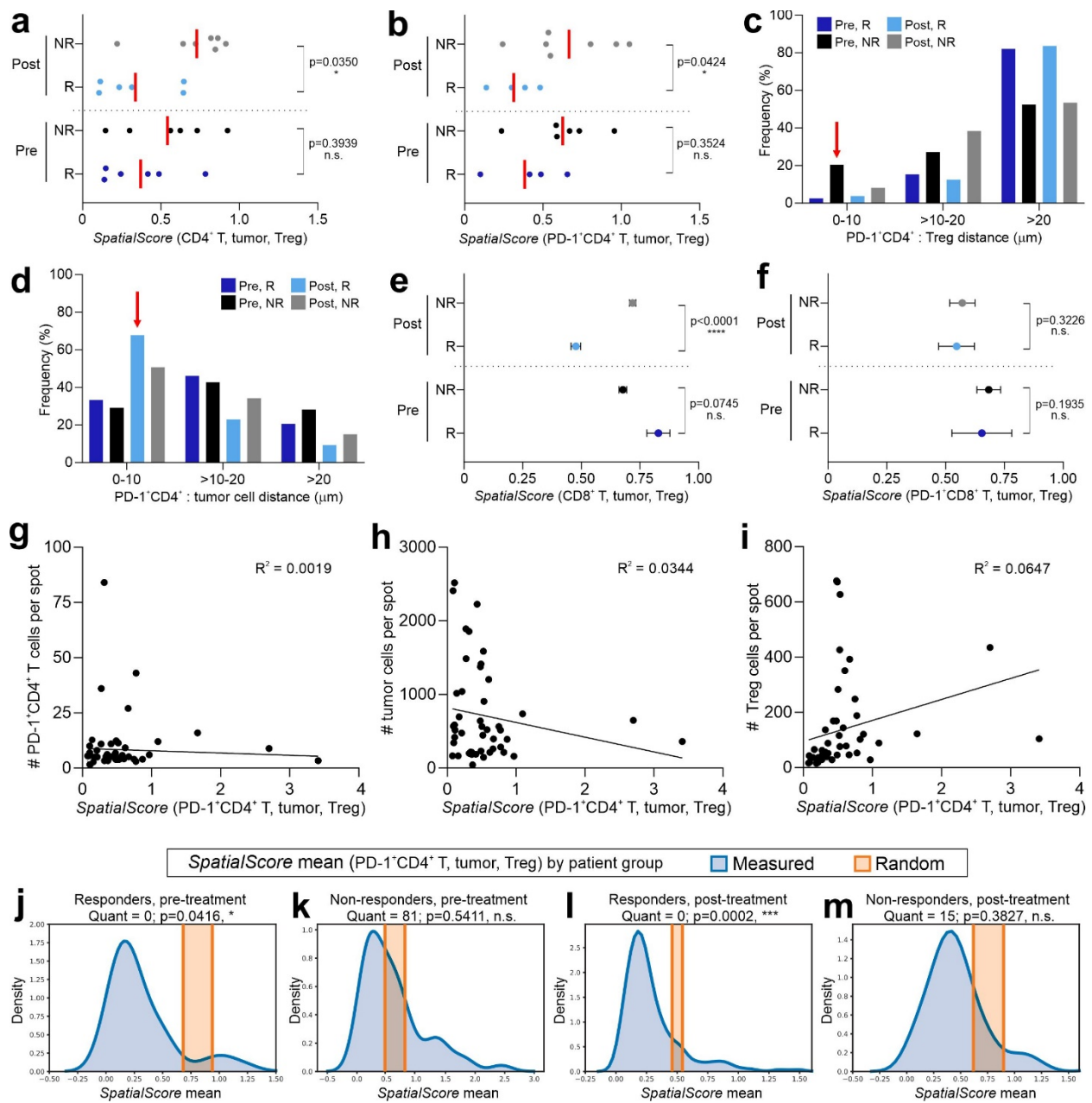
Sup. Fig. 4. Detailing the *SpatialScore* in CTCL. a-b, *SpatialScore* based on all CD4^{+} T cells (**a**) and PD-1^{+}

CD4^{+} T cells (**b**) on a per patient basis across patient groups (mean, red bar). Patients were excluded

from this analysis if they did not have at least 10 CD4^{+} or PD-1^{+} CD4^{+} T cells. *P* values were calculated by

two-sided Wilcoxon's rank-sum tests, with no adjustments for multiple comparisons. **c**, Frequency

distribution of the physical distances in the tissue between PD-1^{+} CD4^{+} and Tregs by patient group, with

the red arrow showing that these two cell-types are closest in non-responders pre-treatment. **d**,

1293   Frequency distribution of the distances between PD-1$^+$ CD4$^+$ and tumor cells by patient group, with the

1294   red arrow showing that these two cell-types are closest in responders post-treatment. **e-f**, *SpatialScore*

1295   on a per cell basis using CD8$^+$ T cells (**e**) and PD-1$^+$ CD8$^+$ T cells (**f**) for each patient group (mean ± s.e.m.).

1296   *P* values were calculated by two-sided Wilcoxon's rank-sum tests, with no adjustments for multiple

1297   comparisons.   **g-i**, Correlations of the number of PD-1$^+$ CD4$^+$ T cells (**g**) tumor cells (**h**), and Tregs (**i**)

1298   relative to the *SpatialScore* per tissue microarray spot. Correlations were evaluated with the Spearman

1299   test. **j-m**, Density plots of the measured mean *SpatialScore* distribution (blue) and corresponding

1300   random mean with its standard deviation (orange) for responders pre-treatment (j) non-responders pre-

1301   treatment (k) responders post-treatment (l), and non-responders post-treatment (m). *P* values were

1302   calculated by two-sided Wilcoxon's rank-sum tests, with no adjustments for multiple comparisons. The

1303   Quant values correspond to the percentage of randomly measured values that are smaller than the

1304   measured value; values closer to 0 or 100 indicate that the measurement is not random.

1305

1306
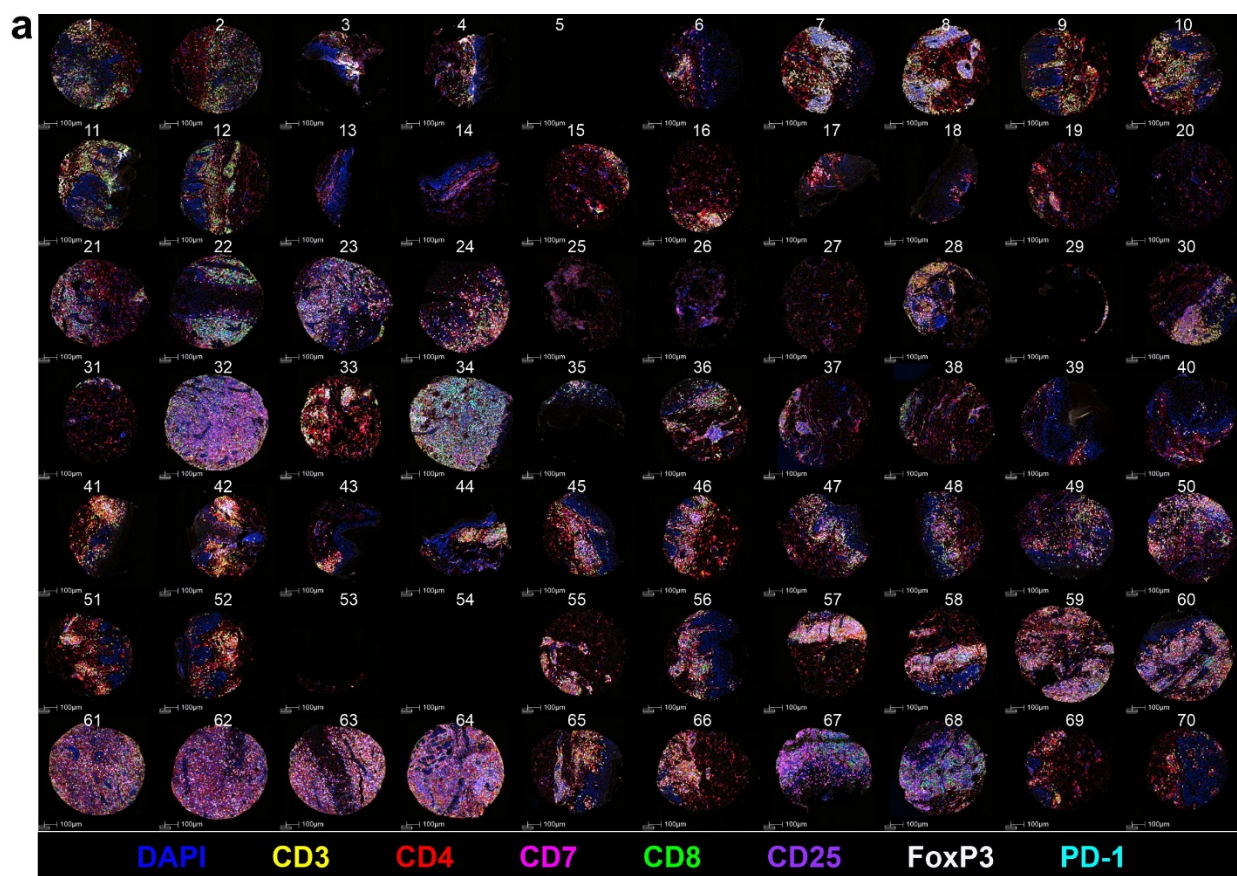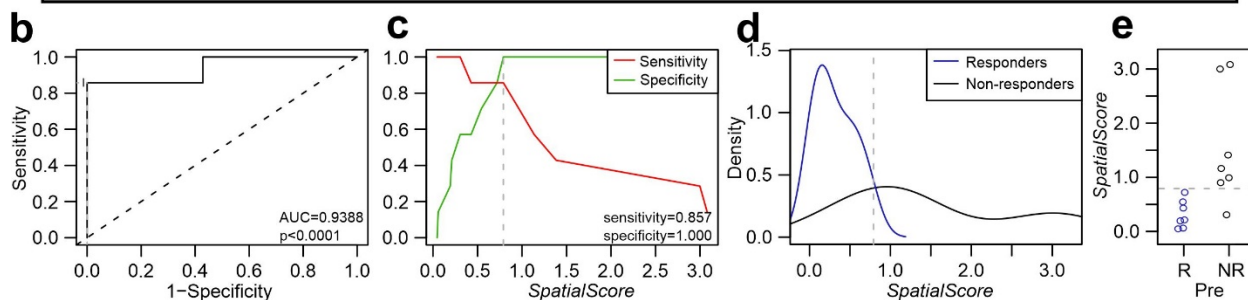
Sup. Fig. 5. Validation of the *SpatialScore* biomarker using a clinically accessible mIHC platform. a, Vectra mIHC staining of the CTCL tissue microarray with an eight-color overlay image, including DAPI (blue), CD3 (yellow), CD4 (red), CD7 (magenta), CD8 (green), CD25 (purple), FoxP3 (white), and PD-1 (cyan). Scale bars, 100 μm. **b-e,** Biomarker performance measures, using an optimal cut-off point of 0.7908, for the pre-treatment *SpatialScore* calculated from data obtained with the Vectra mIHC platform including an ROC curve (**b**),sensitivity and specificity plots (**c**), density plots (**d**), and patient-based scatter

1315   plots (**e**), whereby 100% of responders were below the *SpatialScore* cut-off point and 85.7% of non-

1316   responders were above the cut-off point).

1317
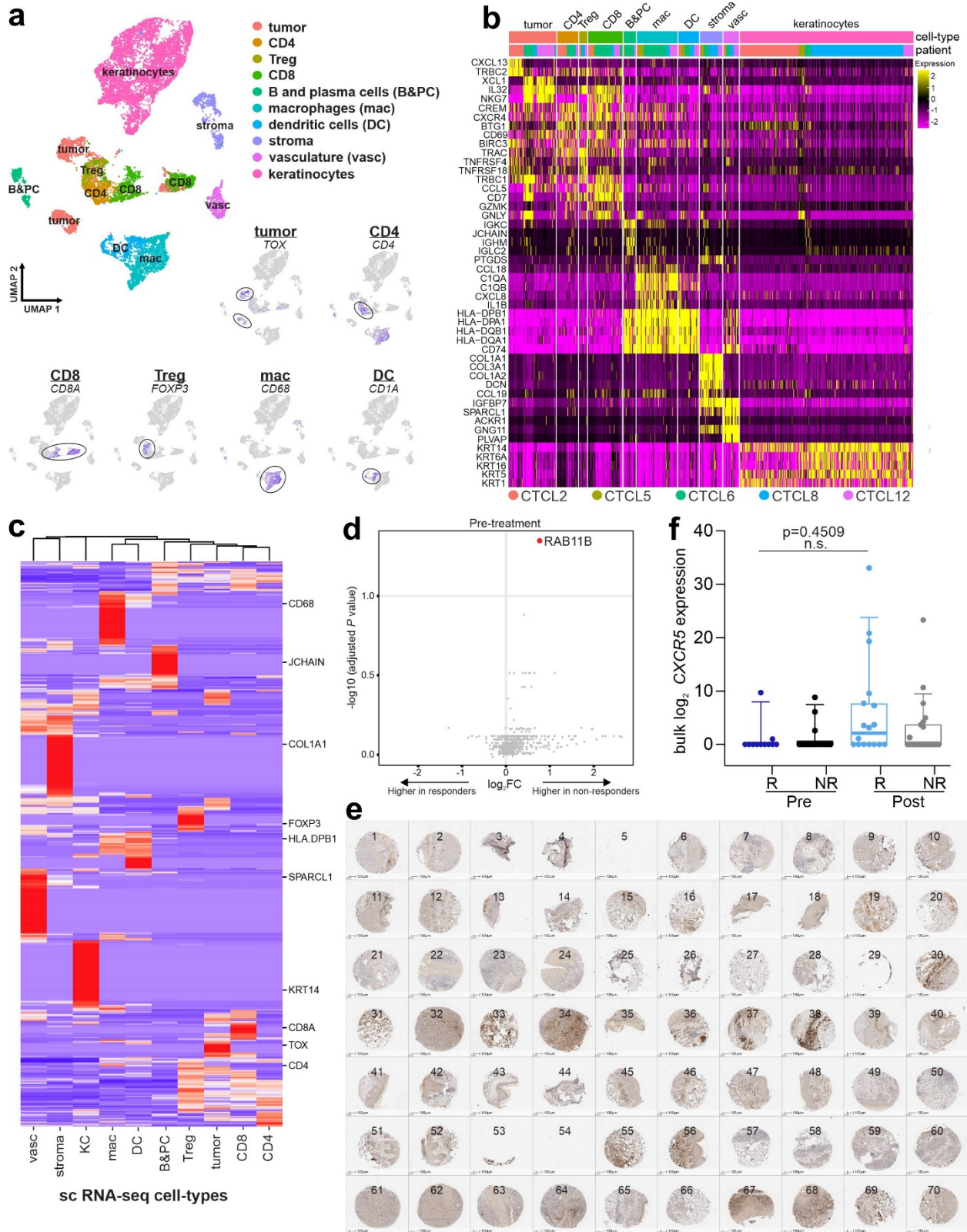
1318

Sup. Fig. 6. Characterizing CIBERSORTx cell-types and CXCL13 expression patterns. a, UMAP of 10

major cell-types identified in the Gaydosik et al.[59] CTCL scRNA-seq dataset (see **Methods**), with feature

1321   plots showing expression for a subset of marker genes including *TOX* (tumor cells), *CD4* (CD4+ T cells),

1322   *CD8A* (CD8+ T cells), *FOXP3* (Tregs), *CD68* (macrophages), and *CD1A* (dendritic cells). **b**, Heatmap of the

1323   top differentially expressed genes (rows) for the 10 cell-types, corresponding to the top color bar. The

1324   other color bar corresponds to patient samples from the Gaydosik et al.[59] CTCL scRNA-seq dataset

1325   (legend is at the bottom of the heatmap). **c**, Signature matrix, highlighting key marker selected genes

1326   (rows), used to enumerate cell-type fractions and resolve gene expression profiles from CTCL bulk RNA-

1327   seq. **d**, Differential expression of CSx-resolved tumor cell genes in responders versus non-responders

1328   pre-treatment. **e**, CXCL13 IHC staining of the CTCL tissue microarray. Scale bars, 100 μm. **f**, Normalized

1329   bulk *CXCR5* gene expression across patient groups. Boxes, median ± IQR; whiskers, 1.5x IQR. *P* values

1330   were calculated with a linear mixed-effect model with Bonferroni's corrections for multiple

1331   comparisons.

1332

1333

1334

1335

Supplementary Table 1. Cohort and tissue microarray layout.

Sup. Table 1a. Cohort.

Patient ID	Age at screening (years)	Gender	Diagnosis	Disease stage	Prior therapies	Response status	Biopsy timepoints	C02 (weeks)	Response / progression time (weeks)	EOT time (weeks)	Death time (weeks)	Follow-up time (weeks)
1	76.14	Male	MF	IIIA	3	Responder	Pre, EOT			104		142
2	60.59	Male	MF	IIIB	4	Responder	Pre, EOT			104		151
3	52.01	Male	SS	IVA	3	Non-responder	Pre, EOT			98	98	98
4	85.14	Female	SS	IVA	4	Non-responder	Pre, EOT			104	142	142
5	75.24	Male	MF	IIB	6	Responder	Pre, EOT			104		103
6	46.74	Male	MF	IVA	9	Non-responder	Pre, C02, EOT	3		25		25
7	46.71	Female	MF	IIIB	3	Non-responder	Pre, EOT			9		9
8	67.44	Male	SS	IIIB	1	Non-responder	Pre, EOT			104	121	121
9	77.65	Female	SS	IVA	6	Responder	Pre, C02, EOT	3		71		71
10	66.40	Male	MF	IIIA	2	Responder	Pre			N/A	119	119
11	72.23	Male	SS	IVA	3	Responder	Pre, Response		22	104		171
12	72.59	Male	SS	IVA	5	Non-responder	Pre, Progression		15	15		15
13	44.10	Female	SS	IVA	1	Responder	Pre, C02, Response, EOT	3	15	104		179
14	63.69	Male	MF	IB	5	Non-responder	Pre, C02, Response, EOT	3	10	92	92	92

MF: mycosis fungoides
SS: Sezary syndrome
Pre: biopsy obtained pre-treatment
C02: biopsy obtained prior to cycle 2
Response / Progression: biopsy obtained at point of response or progression
EOT: end of trial

1347 **Sup. Table 1b. Tissue microarray layout.**

TMA spot	Patient ID	Biopsy timepoint
1	1	Pre_1
2	1	Pre_2
3	1	EOT_1
4	1	EOT_2
5	2	Pre_1
6	2	Pre_2
7	2	EOT_1
8	2	EOT_2
9	3	Pre_1
10	3	Pre_2
11	3	EOT_1
12	3	EOT_2
13	4	Pre_1
14	4	Pre_2
15	4	EOT_1
16	4	EOT_2
17	5	Pre_1
18	5	Pre_2
19	5	EOT_1
20	5	EOT_2
21	6	Pre_1
22	6	Pre_2
23	6	EOT_1
24	6	EOT_2
25	7	Pre_1
26	7	Pre_2
27	7	EOT_1
28	7	EOT_2
29	8	Pre_1
30	8	Pre_2
31	8	Pre_3
32	8	EOT_1
33	8	EOT_2
34	8	EOT_3
35	9	Pre_1
36	9	Pre_2
37	9	EOT_1
38	9	EOT_2
39	10	Pre_1
40	10	Pre_2
41	11	Pre_1
42	11	Pre_2
43	11	Resp_1
44	11	Resp_2
45	12	Pre_1
46	12	Pre_2
47	12	Resp_1
48	12	Resp_2
49	6	C02_1
50	6	C02_2
51	13	Pre_1
52	13	Pre_2
53	13	Resp_1
54	13	Resp_2
55	13	EOT_1
56	13	EOT_2
57	14	Pre_1
58	14	Pre_2
59	14	Resp_1
60	14	Resp_2
61	14	Resp_3
62	14	EOT_1
63	14	EOT_2
64	14	EOT_3
65	14	C02_1
66	14	C02_2
67	9	C02_1
68	9	C02_2
69	13	C02_1
70	13	C02_2

Pre: pre-treatment biopsy
C02: biopsy obtained prior to cycle 2 (3 weeks)
Response / Progression: biopsy obtained
at point of response or progression
EOT: end of trial (104 weeks)

1348

1349

1350 **Supplementary Table 2. Targets.**

Antibody target	Company	Clone	Oligonucleotide	Flourophore	Dilution	Exposure time	Reaction cycle	Reaction channel
CD1a	Novus Biologicals	O10+CA1/71	43	Cy5	1:100	1/2s	20	4
CD2	Biolegend	RPA-2.10	25	Cy5	1:25	1/2s	7	4
CD3	Cell Marque	MRQ-39	77	Cy5	1:100	1/2s	17	4
CD4	Abcam	EPR6855	20	ATTO550	1:100	1/2s	9	3
CD5	Biolegend	UCHT2	75	ATTO550	1:50	1/2s	8	3
CD7	Cell Marque	MRQ-56	63	ATTO550	1:100	1/2s	19	3
CD8	Novus Biologicals	C8/144B	8	Cy5	1:50	1/5s	18	4
CD11b	Abcam	EPR1344	28	Cy5	1:50	1/2s	13	4
CD11c	Abcam	EP1347Y	49	ATTO550	1:50	1/2s	12	3
CD15	BD Biosciences	MMA	14	Alexa488	1:200	1/10s	7	2
CD16	Cell Signaling Technology	D1N9L	26	ATTO550	1:100	1/2s	13	3
CD20	Novus Biologicals	rIGEL/773	48	ATTO550	1:200	1/4s	11	3
CD25	Cell Marque	4C9	24	ATTO550	1:100	1/2s	10	3
CD30	Cell Marque	BerH2	57	ATTO550	1:25	1/2s	7	3
CD31	Novus Biologicals	C31.3+C31.7+C31.10	68	ATTO550	1:200	1/8.5s	25	3
CD34	Novus Biologicals	QBEnd/10	38	ATTO550	1:100	1/4s	23	3
CD38	Abcam	EPR4106	66	ATTO550	1:100	1/2s	24	3
CD45	Novus Biologicals	B11+PD7/26	56	ATTO550	1:400	1/8.5s	20	3
CD45RA	Biolegend	HI100	72	Cy5	1:50	1/2s	19	4
CD45RO	Biolegend	UCH-L1	2	ATTO550	1:100	1/4s	22	3
CD56	Cell Marque	MRQ-42	29	Cy5	1:50	1/2s	10	4
CD57	Biolegend	HCD57	30	ATTO550	1:200	1/4s	21	3
CD68	Biolegend	KP-1	70	Cy5	1:100	1/4s	23	4
CD69	R&D Systems	polyclonal	36	ATTO550	1:200	1/2s	18	3
CD71	Cell Marque	MRQ-48	3	Cy5	1:100	1/5s	22	4
CD138	Novus Biologicals	B-A38	76	ATTO550	1:100	1/8.5s	26	3
CD162	Novus Biologicals	HECA-452	46	Cy5	1:200	1/8.5s	12	4
CD163	Novus Biologicals	EDHu-1	45	Cy5	1:200	1/3s	26	4
CD164	BD Biosciences	N6B6	69	Alexa488	1:200	1/2s	3	2
CD194	Biolegend	L291H4	55	ATTO550	1:100	1/2s	14	3
Beta-catenin	BD Biosciences	14	51	Cy5	1:50	1/2s	21	4
BCL-2	Novus Biologicals	124	41	ATTO550	1:50	1/2s	17	3
Collagen IV	Abcam	polyclonal	33	Cy5	1:200	1/4s	24	4
Cytokeratin	Biolegend	C11	67	Alexa488	1:200	1/5s	6	2
DRAQ5	Cell Signaling Technology	N/A	N/A	Cy5	1:100	1/8.5s	29	4
EGFR	Cell Signaling Technology	D38B1	58	ATTO550	1:25	1/2s	15	3
FoxP3	Abcam	236A/E7	61	ATTO550	1:100	1/4s	3	3
GATA3	Cell Marque	L50-823	60	Cy5	1:100	1/2s	3	4
Granzyme B	Abcam	EPR20129-217	81	Alexa488	1:200	1/8.5s	8	2
HLA-DR	Abcam	EPR2692	65	ATTO550	1:200	1/4s	16	3
ICOS	Cell Signaling Technology	D1K2T	74	Cy5	1:100	1/2s	16	4
IDO-1	Cell Signaling Technology	D5J4E	59	Cy5	1:25	1/2s	14	4
Ki-67	BD Biosciences	B56	6	Cy5	1:100	1/5s	6	4
LAG3	Cell Signaling Technology	D2G4O	42	Cy5	1:25	1/2s	9	4
Mast cell tryptase	Abcam	AA1	44	ATTO550	1:200	1/80s	27	3
MMP9	Biolegend	L51/82	62	Alexa488	1:400	1/3s	9	2
MMP12	Abcam	polyclonal	80	Cy5	1:100	1/2s	27	4
MUC-1	Novus Biologicals	955	15	Alexa488	1:100	1/2s	4	2
p53	Cell Marque	DO7	52	ATTO550	1:50	1/2s	4	3
PD-1	Cell Signaling Technology	D4W2J	23	Cy5	1:50	1/2s	11	4
PD-L1	Cell Signaling Technology	E1L3N	11	ATTO550	1:50	1/2s	6	3
Podoplanin	Biolegend	D2-40	32	Cy5	1:200	1/3s	25	4
T-bet	Cell Signaling Technology	D6N8B	5	ATTO550	1:100	1/2s	5	3
Vimentin	BD Biosciences	RV202	7	Alexa488	1:200	1/4s	5	2
VISTA	Cell Signaling Technology	D1L2G	79	Cy5	1:50	1/2s	15	4

1351

1352

1353

1354 **Supplementary Table 3. Genes lists; related to Figures 2e-h, 4f-h.**

1355 **Sup. Table 3a. Interferon gamma gene score[39].**

1356

Gene	Coefficient
IFNG	-0.30685
HLA-DRA	-0.35484
IDO1	-0.36499
STAT1	-0.45212
CXCL10	-0.46207
CXCL9	-0.47832

1357

1358 **Sup. Table 3b. Transforming growth factor beta gene score[40].**

1359

Gene	Coefficient
IL6ST	0.48031
PDGFRB	0.40325
TGFBR2	0.39434
TNFRSF1A	0.39151
PDGFA	0.25311
KIT	0.25002
FLT4	0.24409
IFNGR1	0.10497
TNFRSF14	0.03628
ACVR1	-0.03375
TGFB1	-0.04924
TNFRSF10B	-0.15319
LIF	-0.17415
IL4R	-0.20508

1360

1361

1362 **Sup. Table 3c. Immune activation gene score.**

Gene	Coefficient
CXCL9	0.28056
CCL5	0.27507
GZMH	0.27229
EOMES	0.26916
GZMK	0.26379
CD27	0.25655
TNFRSF9	0.25375
IL2RG	0.24956
PRF1	0.24024
FASLG	0.23683
IL2RA	0.22805
IFNG	0.21895
ICOS	0.20233
CD40	0.18924
CD40LG	0.18919
IL17RA	0.14444
IL12B	0.13478
TNFSF9	0.12999
CD28	0.12862
CX3CR1	0.11662
TNFRSF4	0.11086
GZMB	0.07612
CCR7	0.06002
IL23A	0.05400

1363

1364

1365   **Sup. Table 3d. Immunosuppression gene score.**

Gene	Coefficient
TGFB1	0.31255
ENTPD1	0.30707
IL24	0.30658
CXCL1	0.30076
IL6	0.29989
TGFBR1	0.27375
IL10	0.24295
HAVCR2	0.20469
PDGFRA	0.20016
HLA-G	0.18822
TGFBRAP1	0.18282
PVT1	0.16990
PDGFRB	0.16723
LINC00473	0.16219
CXCL3	0.16065
TIGIT	0.15326
LIF	0.14962
CXCL12	0.12772
CD274	0.12391
TIAF1	0.11831
LAG3	0.10954
DNM3OS	0.02112
NIFK-AS1	-0.00826
IL4	-0.04139
GNAS-AS1	-0.05070
HOTAIR	-0.06027
PDCD1LG2	-0.08477
GAS5	-0.14413

1366

1367

1368 **Sup. Table 3e. Cytotoxicity gene score[49,50].**

Gene	Coefficient
NKG7	0.39045
PRF1	0.35018
TNF	0.34146
GZMH	0.32965
TBX21	0.31663
GZMK	0.31526
GZMM	0.29080
ID2	0.26046
IFNG	0.25047
GNLY	0.22788
GZMB	0.18149

1369

1370 **Sup. Table 3f. Tumor aggressiveness[51,52].**

Gene	Coefficient
IL2RB	0.30377
BATF	0.29598
IL21R	0.28415
CCND2	0.26500
RGS16	0.25940
MYO7A	0.25910
SLA	0.25436
ANP32E	0.23795
MTHFD2	0.21538
IL10	0.21012
TRIB2	0.20521
RARRES3	0.19264
GNLY	0.19238
DUSP5	0.18767
C1GALT1	0.15656
BCL2	0.15272
EHD1	0.13197
HSPD1	0.13011
DAD1	0.12384
MMP12	0.08265
IL26	0.07073
IL22	0.06240
P4HB	-0.05212
TCN1	-0.07340
SFTPD	-0.12905
TGFBR3	-0.18280

1371

Supplementary Table 4. CIBERSORTx marker genes.

Sup. Table 4a. Markers of CIBERSORTx cell-types.

Cell-types	Marker genes	CIBERSORTx cell-types
B cells & plasma cells	*MS4A1, LTB, CD79A, CD79B*	B and plasma cells
T cells	*CD3E, CD3D, CD274*	CD4 T, CD8 T, Tregs, tumor cells
Macrophages & dendritic cells	*AIF1*	Macrophages, dendritic cells
Keratinocytes	*KRT1, KRT14*	Epithelium
Vasculature	*CD43, PECAM1, CLDN5*	Vasculature
Fibroblasts	*COL1A1, SFRP2*	Stroma
Pericytes	*RGS5, ACTA2*	

1374

Sup. Table 4b. T cell and tumor cell markers for CIBERSORTx.

| T cell markers (reactive CD4+, CD8+, Tregs)				Tumor markers			
CD4	*FOXP3*	*IL2*	*STAT6*	*ACTG1*	*CDK1*	*KIAA0101*	*PRDX1*
CD7	*GATA3*	*IL2RA*	*TBX21*	*ANP32B*	*CDK6*	*MCTS1*	*PSMB2*
CD8A	*GZMA*	*IL4*	*TGFB1*	*ATP5C1*	*CENPE*	*MKI67*	*RAN*
CD8B	*GZMB*	*ITGAE*	*TIGIT*	*BCL2*	*CENPM*	*MYC*	*RANBP1*
CD27	*HAVCR2*	*LAG3*	*TNF*	*BCL2L12*	*DUT*	*NPM1*	*SET*
CD44	*ICOS*	*PDCD1*	*TRAC*	*BIRC3*	*FOS*	*NUSAP1*	*SMC4*
CD69	*IFNG*	*PRF1*	*TRBC1*	*BIRC5*	*HMGN1*	*PCNA*	*STMN1*
CD160	*IKZF2*	*RORC*	*TRBC2*	*CCNA2*	*HMMR*	*PIM2*	*TOP2A*
CTLA4	*IL10*	*RUNX3*	*TRDC*	*CCND1*	*HN1*	*PLK1*	*TOX*
EOMES	*IL17A*	*STAT3*	*TRGC1*	*CDC20*	*IGF2*	*PPA1*	*TSC22*
FASLG	*IL1B*	*STAT4*	*TRGC2*	*CDCA8*	*IL2RA*	*PPIA*	

1376

Figures
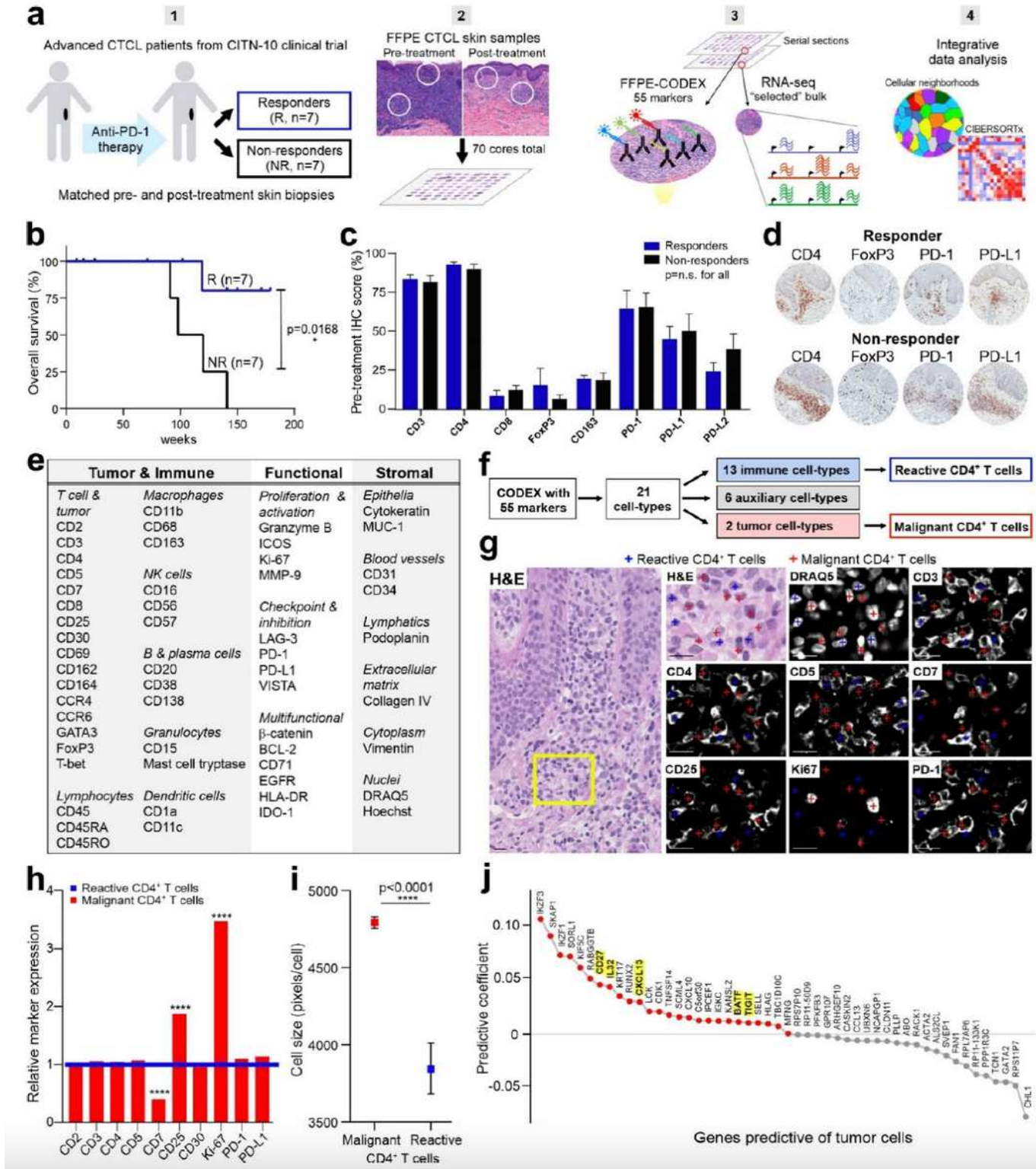
Figure 1

Discrimination of malignant and reactive CD4+ T cells in the CTCL TME. a, Workflow for sample preparation, CODEX, RNAseq, and computational analyses. b, Kaplan-Meier overall survival curve, comparing responders (R, n=7, blue line) and non-responders (NR, n=7, black line) (hazard ratio 0.0969
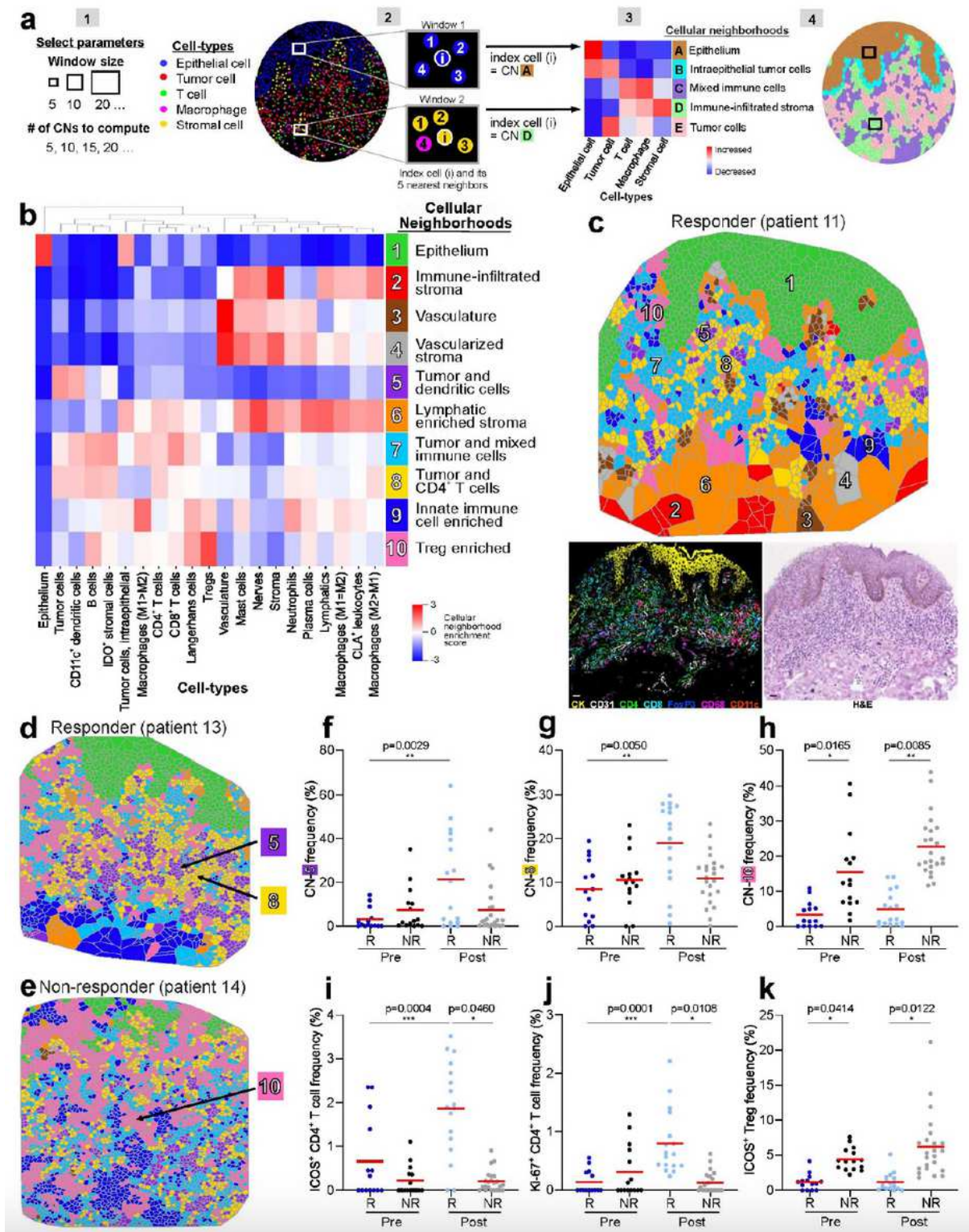
responder/non-responder; p value calculated by log-rank test). c, IHC protein marker expression in responders and non-responders pre-treatment (mean ± s.e.m.). P values were calculated by two-sided Wilcoxon's rank-sum tests (p = not significant (n.s.) for all comparisons). d, Representative pre-treatment IHC images for select markers from a responder (top) and non-responder (bottom). e, CODEX antibody panel (see also Sup. Fig. 1d). f, Identification of 21 cell-types by clustering (see also Sup. Fig. 2a-b). g, Visual verification of reactive (blue crosses) versus malignant (red crosses) CD4+ T cells in CTCL tissue. Scale bars, 20 μm. h, Average expression of select markers on malignant (red bars) relative to reactive (blue line) CD4+ T cells. P values were calculated by two-sided Wilcoxon's rank-sum tests (****, p<0.0001). i, Cell size, measured in pixels/cell, of all malignant (red square) versus reactive (blue square) CD4+ T cells (mean ± s.e.m.). P value was calculated by a two-sided Wilcoxon's rank-sum test. j, Ranking genes most predictive of tumor cells per tissue microarray spot using an L1-regularized linear model. Red colored genes have positive predictive coefficients (i.e., most likely to represent tumor cells); gray colored genes have negative predictive coefficients (i.e., less likely to represent tumor cells). Known CTCL marker genes are highlighted in yellow.
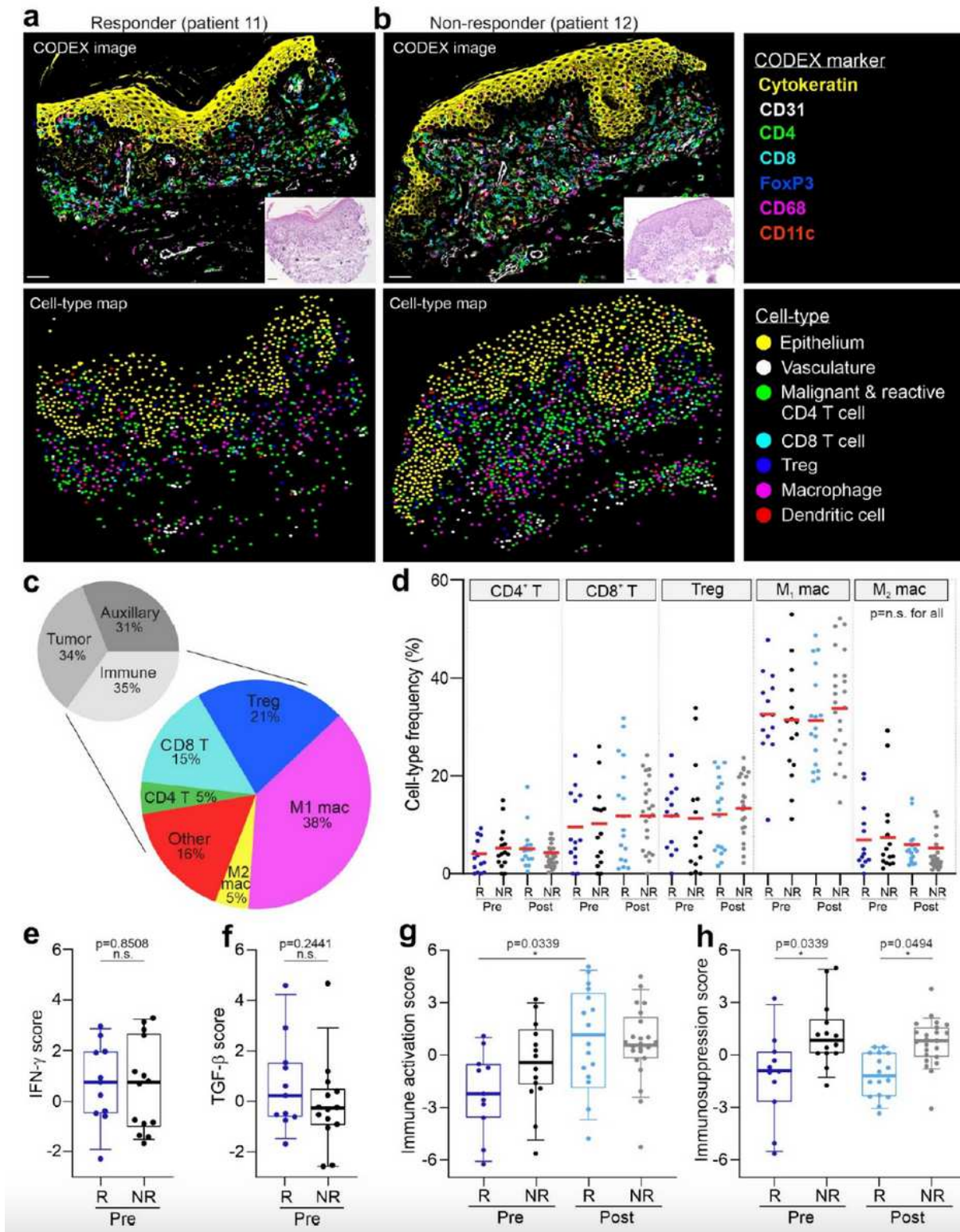
Figure 2

Characterization of the CTCL TME pre- and post-pembrolizumab treatment. a-b, Top panels:Representative CODEX seven-color overlay images from a responder (left) and non-responder (right) pre-treatment. Scale bar, 50 μm. Insets, corresponding H&E images; scale bars, 50 μm. Bottom panels: corresponding cell-type maps. c, Upper pie chart: overall frequencies of tumor, immune and auxiliary cell-types. Lower pie chart: overall frequencies of all immune cell-types, including CD4+ T cells,

CD8+ T cells, Tregs, M1 macrophages, M2 macrophages, and other (B cells, dendritic cells, Langerhans cells, mast cells, neutrophils, and plasma cells). d, Cell-type frequencies of CD4+ T cell, CD8+ T cell, Treg, M1 macrophage, and M2 macrophage as a percentage of all immune cells per tissue microarray spot in responders and non-responders pre- and post-treatment (mean, red bar). P values were calculated with a linear mixed-effect model with Bonferroni's corrections for multiple comparisons (p = not significant (n.s.) for all comparisons). e-f, IFN-γ (e) and TGF-β (f) gene scores between responders and non-responders pre-treatment per spot. Boxes, median ± interquartile range (IQR); whiskers, 1.5x IQR. P values were calculated with a linear mixed-effect model with Bonferroni's corrections for multiple comparisons. g-h, Immune activation (g) and immunosuppression (h) gene scores, computed on bulk RNA-seq data, between responders and non-responders pre- and post-treatment per spot. Boxes, median ± IQR; whiskers, 1.5x IQR. P values were calculated with a linear mixed-effect model with Bonferroni's corrections for multiple comparisons.
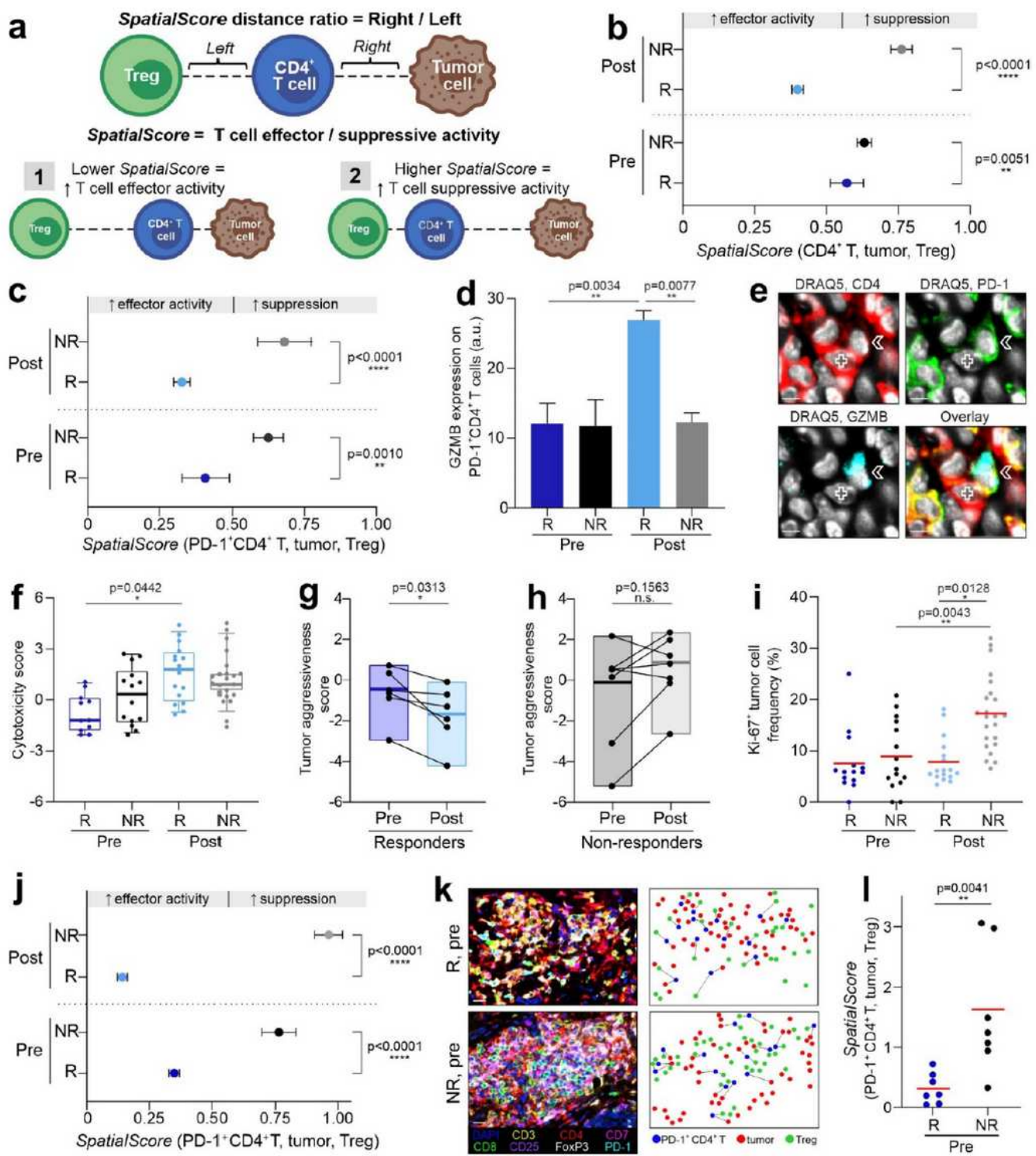
Figure 3

Cellular neighborhoods reveal differences in the spatial TME organization in responders and non-responders. a, Cellular neighborhood (CN) analysis schematic. [1] Selection of computational parameters, including the window size (five in this schematic) and the number of CNs to be computed (five in this schematic). [2] Assignment of an index cell (i, center of window) to a given CN based on the composition of cell-types within its corresponding window the clustering of windows. [3] Heatmap of cell-type

distribution for each CN and assignment of CN names. [4] Visualization of CNs as a Voronoi diagram. b, Identification of 10 conserved CNs in the CTCL TME using a window size of 10. c, Representative Voronoi diagram of the 10 CNs in a responder post-treatment, with the corresponding H&E and seven color fluorescent CODEX images. Scale bar, 20 μm. d-e, Voronoi diagrams of CNs in a responder (d) and non-responder (e) post-treatment, highlighting CN-5 (tumor and dendritic cells), CN-8 (tumor and CD4+ T cells) and CN-10 (Treg enriched). f-h, Frequencies of CN-5 (f), CN-8 (g) and CN-10 (h) per tissue microarray spot in responders and non-responders pre- and post-treatment (mean, red bar). P values were calculated with a linear mixed-effect model with Bonferroni's corrections for multiple comparisons. i-k, Frequencies of ICOS+ CD4+ T cell (i), Ki-67+ CD4+ T cell (j) and ICOS+ Treg (k) as a percentage of all immune cells per spot in responders and non-responders pre- and post-treatment (mean, red bar). P values were calculated with a linear mixed-effect model with Bonferroni's corrections for multiple comparisons.
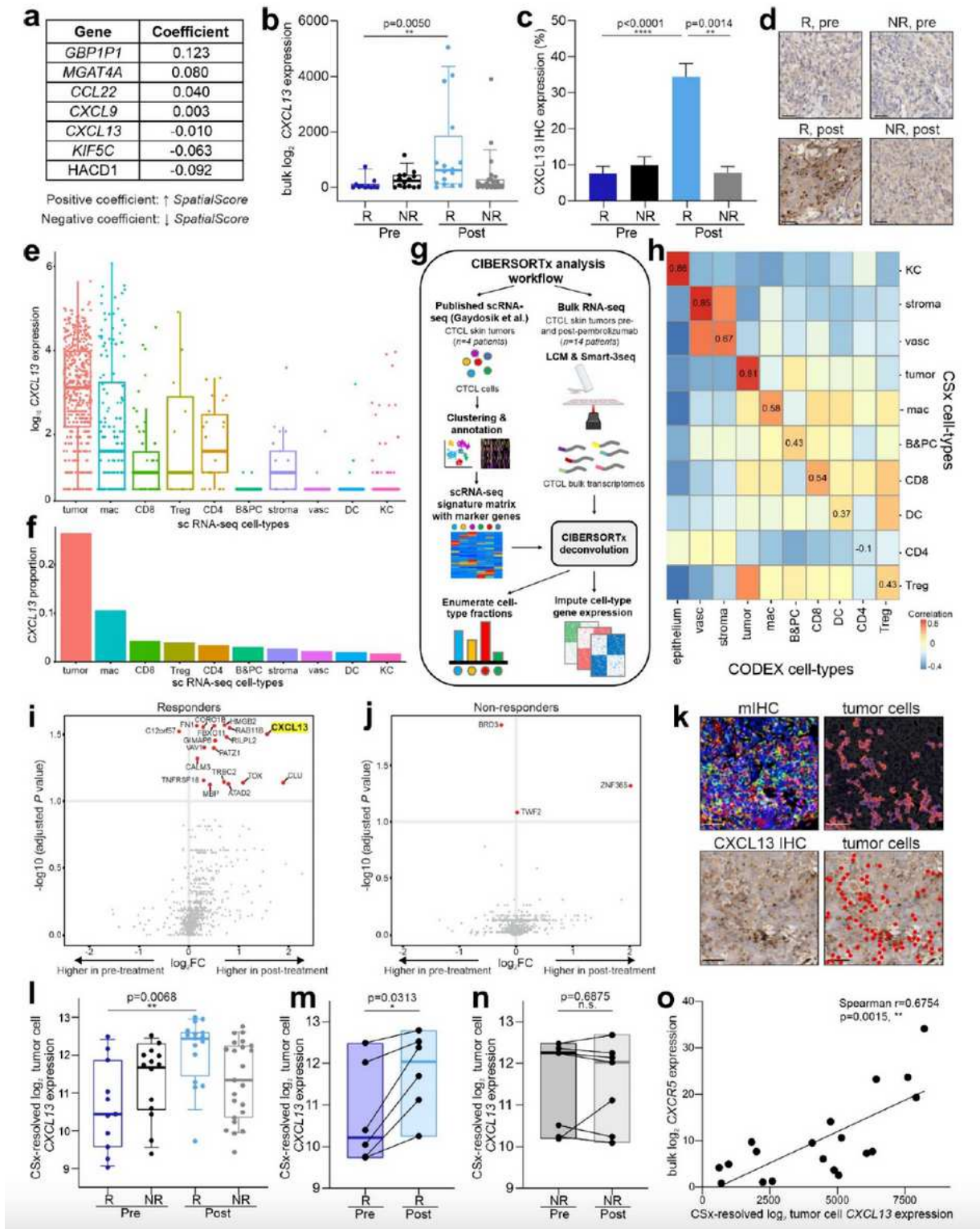
Figure 4

Spatial relationship between CD4+ T cells, Tregs and tumor cells predicts pembrolizumab response in CTCL. a, SpatialScore schematic. The SpatialScore is calculated by taking the ratio of the physical distance between each CD4+ T cell and its nearest tumor cell (distance "right") relative to its nearest Treg (distance "left"). [1] A lower SpatialScore (i.e., CD4+ T cells are closer to tumor cells than Tregs) suggests increased T cell effector activity. [2] A higher spatial score (i.e., CD4+ T cells are closer to Tregs than

tumor cells) suggests increased T cell suppression. b-c, SpatialScore on a per cell basis for CD4+ T cells (b) and PD-1+ CD4+ T cells (c) for each patient group (mean ± s.e.m.). P values were calculated by two-sided Wilcoxon's rank-sum tests, with no adjustments for multiple comparisons. d, GZMB protein expression on PD-1+ CD4+ T cells by CODEX in responders and non-responders pre- and post-treatment per tissue microarray spot (mean fluorescence intensity (arbitrary units, a.u.) ± s.e.m.) P values were calculated with a linear mixed-effect model with Bonferroni's corrections for multiple comparisons. e, CODEX images of DRAQ5 (white), CD4 (red), PD-1 (green), GZMB (cyan), and overlay showing contact between a tumor cell (marked by cross) and GZMB-expressing PD-1+ CD4+ T cell (marked by arrow) in responder patient 13 post-treatment. Scale bars, 10 µm. f, Cytotoxicity gene scores, computed on bulk RNA-seq data, between responders and non-responders pre- and post-treatment per spot. Boxes, median ± IQR; whiskers, 1.5x IQR. P values were calculated with a linear mixed-effect model with Bonferroni's corrections for multiple comparisons. g-h, Pre- to post-treatment changes in tumor aggressiveness gene scores, computed on bulk RNA-seq data, on a per patient basis in responders (g) and non-responders (h). Boxes, median ± IQR; whiskers, 1.5x IQR. P values were calculated by two-sided Wilcoxon's signed-rank tests. i, Ki-67+ tumor cell frequencies per spot in responders and non-responders pre- and post-treatment (mean, red bar). P values were calculated with a linear mixed-effect model with Bonferroni's corrections for multiple comparisons. j, SpatialScore on a per cell basis calculated from Vectra mIHC data using PD-1+CD4+ T cells for each patient group (mean ± s.e.m.). P values were calculated by two-sided Wilcoxon's rank-sum tests, with no adjustments formultiple comparisons. k, Vectra mIHC images (left panels; representative regions of a tissue microarray spot) in responder patient 13 (R) and non-responder patient 14 (NR) pre-treatment. Scale bars, 20 µm. The corresponding spatial plots (right panels) show that PD-1+ CD4+ T cells (blue dots) are closer to tumor cells (red dots) than Tregs (green dots) in the responder and vice versa in the non-responder. l, Pre-treatment SpatialScore calculated from Vectra mIHC data for responders and non-responders on a per patient basis (mean, red bar). P values was calculated by a two-sided Wilcoxon's rank-sum test.
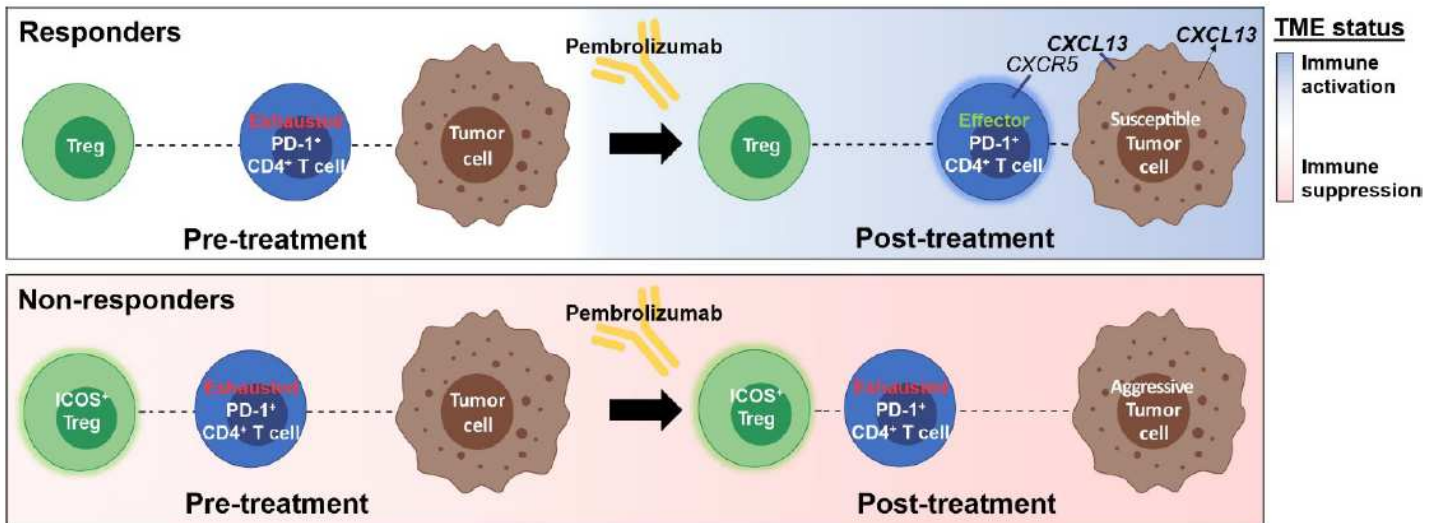
Figure 5

CXCL13 is a key driver of pembrolizumab response in CTCL. a, Seven genes predictive of the SpatialScore identified from bulk RNA-seq data. Genes with a positive coefficient are associated with a higher SpatialScore (i.e., a suppressive phenotype), whereas those with a negative coefficient are associated with a lower SpatialScore (i.e., an effector phenotype). b, Normalized bulk CXCL13 gene expression between responders and non-responders pre- and post-treatment per tissue microarray spot.

Boxes, median ± IQR; whiskers, 1.5x IQR. P values were calculated with a linear mixed-effect model with Bonferroni's corrections for multiple comparisons. c, CXCL13 protein expression by IHC in responders and non-responders pre- and post-treatment per spot (mean ± s.e.m.). P values were calculated with a linear mixed-effect model with Bonferroni's corrections for multiple comparisons. d, Representative CXCL13 IHC images from responder patient 9 pre-treatment (top left) and post-treatment (bottom left) as well as non-responder patient 14 pre-treatment (top right) and post-treatment (bottom right). Scale bars, 20 μm. e-f, Single-cell transcriptomes from a publicly available scRNA-seq dataset of CTCL skin tumors (Gaydosik et al.)[59] were analyzed for CXCL13 expression. Abbreviations: mac (macrophages), B&PC (B and plasma cells), vasc (vasculature), DC (dendritic cells), and KC (keratinocytes). e, Normalized expression of CXCL13 in single cells (each dot represents a cell positive for CXCL13). Cells with CXCL13 log1p normalized read counts less than 0.5 were excluded (see Methods). Boxes, median ± IQR; whiskers, 1.5x IQR. f, Proportion of CXCL13-expressing cells per cell-type. g, CIBERSORTx analysis workflow schematic. Single cell transcriptomes from Gaydosik et al.[59] were used to generate a CSx deconvolution signature matrix, consisting of cell-type-specific marker genes (left portion of schematic). This matrix was then applied to CTCL bulk transcriptomes obtained with laser-capture microdissection (LCM) and Smart-3Seq (right portion of schematic) to enumerate cell-type fractions and resolve gene expression profiles (see Methods). h, Heatmap of the correlation between CSx-resolved cell-type frequencies and CODEX-identified cell-type frequencies. Spearman correlation coefficients between corresponding cell-types are shown along the diagonal. For this analysis, some of the original 21 CODEX cell-types were manually merged to match CSx cell-types (e.g., B cells and plasma cells). i-j, Volcano plots of differential gene expression of CSx-resolved tumor cell genes in responders (j) and non-responders (k) pre- and post-treatment. P values were calculated with a linear mixed-effect model with Benjamini-Hochberg correction. Significantly different genes ($p < 0.1$) are colored red; CXCL13 is highlighted yellow. k, Vectra mIHC image of DAPI (blue), CD3 (yellow), CD4 (red), CD7 (magenta), CD8 (green), CD25 (purple), FoxP3 (white), and PD-1 (cyan) (top left), corresponding tumor cell depiction (top right), corresponding CXCL13 IHC image (bottom left), and overlaid image showing that CXCL13 IHC staining most commonly localized to tumor cells (red circles) (bottom right) in responder patient 9 post-treatment. Scale bars, 20 μm. l, Normalized CSx-resolved CXCL13 expression in tumor cells between responders and non-responders pre- and post-treatment per spot. Boxes, median ± IQR; whiskers, 1.5x IQR. P values were calculated with a linear mixed-effect model with Bonferroni's corrections for multiple comparisons. m-n, Pre- to post-treatment changes in normalized CXCL13 gene expression from CSx-resolved tumor genes on a per patient basis in responders (m) and non-responders (n). Boxes, median ± IQR; whiskers, 1.5x IQR. P values were calculated by two-sided Wilcoxon's signed-rank tests. o, Correlation of CSx-resolved tumor cell CXCL13 expression and bulk CXCR5 expression per spot. Data was evaluated with the Spearman test and a two-tailed t-distribution with n-2 degrees of freedom.

Figure 6

Proposed mechanisms of pembrolizumab response in CTCL. Proposed mechanisms of pembrolizumab response in therapy responders (top panel) and non-responders (bottom panel) pre- and post-treatment. The functional immune status of the TME is represented by blue shading when activated and pink shading when suppressed. In non-responders, the TME is continually immunosuppressed and persistently exhausted PD-1+CD4+ T cells are in closer proximity to potently suppressive ICOS+ Tregs. Due to pembrolizumab resistance, non-responder tumor cells become more aggressive following therapy. In contrast, responders have a neutral functional immune state pre-treatment, which becomes activated following pembrolizumab therapy, enabling the transition from exhausted to effector PD-1+ CD4+ T cells. Additionally, responder tumor cells are susceptible to PD-1 blockade and overexpress CXCL13. This attracts effector PD-1+ CD4+ T cells toward tumor cells, providing a mechanism for the sustained clinical response seen in responders.

Supplementary Files

This is a list of supplementary files associated with this preprint. Click to download.

- SupplementalData.pdf